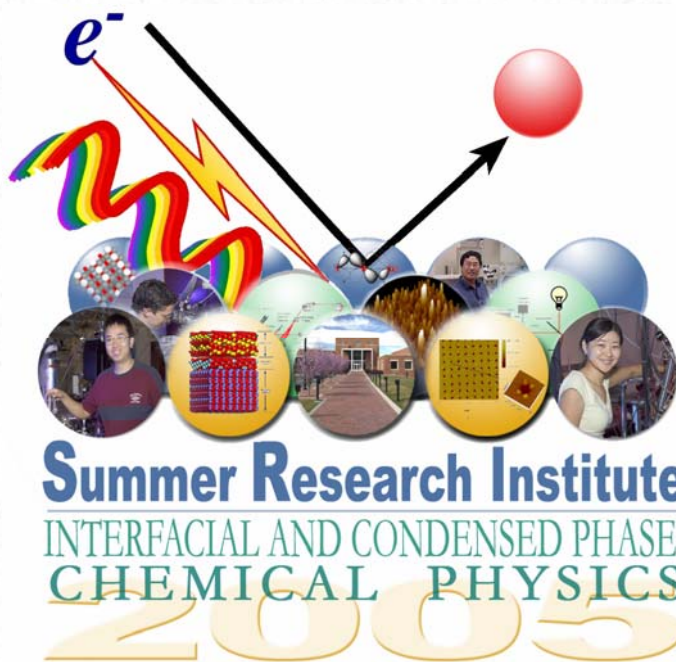**Pacific Northwest National Laboratory**
Operated by Battelle for the
U.S. Department of Energy

2005 Annual Report

Summer Research Institute
Interfacial and Condensed Phase
Chemical Physics

November 2005

Office of Science
U.S. DEPARTMENT OF ENERGY

DISCLAIMER

This report was prepared as an account of work sponsored by an agency of the United States Government. Neither the United States Government nor any agency thereof, nor Battelle Memorial Institute, nor any of their employees, makes **any warranty, express or implied, or assumes any legal liability or responsibility for the accuracy, completeness, or usefulness of any information, apparatus, product, or process disclosed, or represents that its use would not infringe privately owned rights**. Reference herein to any specific commercial product, process, or service by trade name, trademark, manufacturer, or otherwise does not necessarily constitute or imply its endorsement, recommendation, or favoring by the United States Government or any agency thereof, or Battelle Memorial Institute. The views and opinions of authors expressed herein do not necessarily state or reflect those of the United States Government or any agency thereof.

This document was printed on recycled paper.

2005 Annual Report

Summer Research Institute
Interfacial and Condensed Phase
Chemical Physics

October 2005

Pacific Northwest National Laboratory
Richland, Washington 99354

Executive Summary

Pacific Northwest National Laboratory (PNNL) hosted the second annual Summer Research Institute in Interfacial and Condensed Phase Chemical Physics from May through September 2005. During this period, 16 PNNL scientists hosted 14 young scientists from 11 different universities. Of the 14 participants, 12 were graduate students; one was a postdoctoral fellow; and one was a university faculty member.

Table of Contents

Acknowledgements

Even a modest-sized program such as this one would not happen without the involvement of many people. This year's scientific oversight committee consisted of Drs. Donald R. Baer, L. Rene Corrales, and Stephan E. Barlow. Ms. Nikki B. Avery, our administrator in 2005, played the key role in ensuring that the institute ran smoothly. Ms. Cynthia A. Irwin, Operations Administrator for Chemical Structure and Dynamics, administered financial and budgetary support, and Ms. Christine C. Montgomery provided invaluable administrative support.

We also acknowledge Ms. Rebecca J. Janosky of PNNL's Science and Engineering Education Office. She handled a myriad of details associated with fellowship appointments, including fellowship awards, agreements, and disbursement of stipends, while dealing with a major reorganization.

We also wish to acknowledge the following PNNL staff members for their expertise and timeliness in creating and developing the institute's website, application website, and finalizing the institute's brochure: Mr. Matthew Elliott, Publication Design Group; Mr. Mark D. Bayless, Rich Interaction Environments Group; and Ms. Elaine C. Schneider, Graphics and Multimedia Design Group.

We also wish to acknowledge the U.S. Department of Energy's Office of Basic Energy Sciences, which provided guidance needed to initiate the Summer Research Institute in Interfacial and Condensed Phase Chemical Physics and the financial support needed to actually plan and execute the institute's program.

Finally, the real stars of the Interfacial and Condensed Phase Chemical Physics Summer Research Institute were our participants. The remainder of this document is devoted to them.

Summary

PNNL's Management and Operations Contract with the U.S. Department of Energy (DOE)[a] identifies the following Office of Basic Energy Science (BES) Mission Stretch Goal: *"To establish PNNL in a national leadership role in the area of theoretical and experimental condensed phase and interfacial chemical physics research."* Successful achievement of a national leadership role will be evidenced by *"Establishment of a summer school (at least two weeks in duration) to educate graduate students and young scientists in state-of-the-art theory, simulation, and experimental measurement, with a total attendance of at least 60 over the contract period."*

Interfacial and condensed phase chemical physics is not so much a specific field of study as it is a cross-cutting concept. Important issues exist in nearly every scientific discipline from astronomy to zoology that fall with the purview of this general concept area. Likewise, all of the technology and engineering of the modern world as well as our hopes for future development depend to one degree or another on our ability to understand and manipulate condensed phases and interfacial processes.

The guidance provided by the DOE Office of Science gave considerable latitude in implementing the institute's advanced program, which focuses on graduate students, postdoctoral fellows, and university faculty members. The institute caters to more senior people than generally accommodated by PNNL's summer internship programs. We believe that the best education people at this level can receive is to actively engage in research that is relevant to their own career development goals. To accomplish this objective, the institute has a different character and puts different requirements on its participants than do either standard internship programs or other institutes, workshops, etc. Perhaps the best overall description of the Summer Research Institute in Interfacial and Condensed Phase Chemical Physics is a "visiting scientist program for early career researchers." In this spirit, each young scientist's particular program was individually tailored to specific research interests. The descriptions given below are generally true for most of the young scientists but may or may not apply to any particular individual.

Participants and the Institute Structure

Prospective participants applied electronically at the Summer Research Institute's web site at www.pnl.gov/si/. Application submission and screening and correspondence with applicants were all handled online. This greatly approach facilitated the review and screening process as well as record keeping. The Director of the Institute handled preliminary screenings of the applications, acknowledged receipt, and informed applicants of any additional information or actions needed to complete the application process. A number of candidates were found to be unsuited to participate in the institute, and they were informed as soon as that determination was be made. Reasons for rejection at this stage included:

---

[a] Appendix H of Contract DE-AC06-76RL01830, Modification M375.

- The candidate's area of interest was outside of the scope of the program (e.g., high-energy physics or genetics).

- The prospective PNNL hosts were already committed or were unavailable.

- The candidate was finishing an M.S. or a Ph.D. degree and did not have a new position.

- The candidate failed to finish the application process.
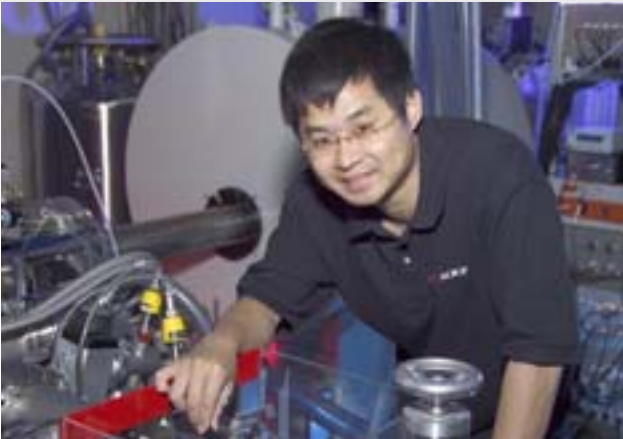
Candidates who passed the initial screening and who had identified a PNNL host were then required to submit a summary of proposed research or activity that they would conduct at during the summer. Normally, the proposal was prepared with the assistance of both the PNNL host and the candidate's academic advisor or supervisor (as appropriate). Once the application deadline had passed, a PNNL science panel composed of Dr. Donald R. Baer and Dr. L. Rene Corrales of PNNL's Fundamental Science Directorate and Dr. Stephan E. Barlow of PNNL's Environmental Molecular Sciences Laboratory (EMSL) reviewed all the completed applications. Each successful candidate received unanimous approval of the panel. Individual acceptance and rejection letters were prepared and distributed by the Institute Director. Interestingly, all of the candidates who were accepted agreed to come. Table 1 provides some statistics on applications and acceptances.

Table 1. 2005 Summer Research Institute in Interfacial and Condensed Phase Chemical Physics Participant Numbers	
Applications and inquiries	22
Acceptances	14
Participants	14
Graduating Seniors	0
Graduate Students	12
Postdoctoral Fellows	1
Faculty	1
U.S. Citizens/Foreign National	5/9
PNNL Hosts	16

The application and acceptance procedure required participation from all concerned parties: the PNNL hosts, the participants, and the participants' academic advisors or supervisors at their home institutions (if applicable). Further, PNNL hosts were expected to provide appropriate mentoring for the visitors as well the resources needed to accomplish the proposed work. The participants' academic advisors or supervisors were expected to continue financial support during the stay at PNNL because the Summer Research Institute normally could only cover travel expenses to and from PNNL and partial living expenses.

Each participant had a specific program tailored around his or her schedule and research goals. To accommodate individual schedules, the 2005 summer appointments began in early May, and the final appointment concluded in September. Prior to arrival, each participant was paired with the PNNL host and a research program was identified. All of this activity was coordinated with the visitor's academic advisor or supervisor. Most often, the participant was playing a role in a collaboration or prospective collaboration between the PNNL host and his or her supervisor. (For the cases of graduating seniors or faculty members slightly different procedures apply.) Table 2 lists our participants, their PNNL hosts, and academic advisors or supervisors.

Table 2.   Interfacial and Condensed Phase Chemical Physics Summer Research Institute Participants, PNNL Hosts, and Academic Advisors or Supervisors

Visitors	
	Professor Ivan Keung Chu Department of Chemistry University of Hong Kong Hong Kong ivankchu@hku.hk **PNNL Hosts:** Julia Laskin and Jean H. Futrell, FSD Julia.Laskin@pnl.gov Jean.Futrell@pnl.gov **Supervisor:** N/A
	Michael R. Dyer Florida State University Tallahassee, Florida **PNNL Host:** Fei Gao, FSD Fei.Gao@pnl.gov **Supervisor** Professor Anter El-Azab Department of Mechanical Engineering Florida State University Tallahassee, Florida anter@eng.fsu.edu

Timothy Fister
University of Washington
Seattle, Washington

PNNL Host:
John L. Fulton, FSD
john.fulton@pnl.gov

Supervisor:
Professor Gerald T. Seidler
Physics Department
University of Washington
Seattle, Washington
seidler@phys.washington.edu

Jason R. Green
Purdue University
West Lafayette, Indiana

PNNL Host:
Julia Laskin, FSD
Julia.Laskin@pnl.gov

Supervisor:
Professor R. Graham Cooks
Chemistry Department
Purdue University
West Lafayette, Indiana
cooks@purdue.edu

Christos Evangelos Kefalidis
Aristotle University of Thessaloniki
Thessaloniki, Greece

PNNL Host:
Sotiris S. Xantheas, FSD
sotiris.xantheas@pnl.gov

Supervisor:
Professor Constantinos Tsipis
Chemistry Department
Aristotle University of Thessaloniki
Thessaloniki, Greece

Satyanarayana Kuchibhatla
Central Florida University
Orlando, Florida

PNNL Host:
Donald R. Baer, FSD
don.baer@pnl.gov

Supervisor:
Professor Sudipta Seal
Advanced Materials Processing and Analysis
Central Florida University
Orlando, Florida
Sseal@pegasus.cc.ucf.edu

Anoop Menon Mayampurath
Utah State University
Logan, Utah
(Now at PNNL)

PNNL Host:
Marianne B. Sowa, FSD
James C. Solinsky, NSD
Marianne.sowa@pnl.gov
James.solinsky@pnl.gov

Supervisor:
Professor Scott Budge
Electrical and Computer Engineering
Utah State University
Logan, Utah
scott.budge@ece.usu.edu

Fung Suong Ou
Rensselaer Polytechnic University
Troy, New York

PNNL Host:
Laxmikant V. Saraf, EMSL
lax.saraf@pnl.gov

Supervisor:
Professor Pulickel Ajayan
Material Science and Engineering
Rensselaer Polytechnic University
Troy, New York
ajayan@rpi.edu

Benjamin Schmid
University of Oregon
Eugene, Oregon

PNNL Host:
S. Thomas Autrey, FSD
tom.autrey@pnl.gov

Supervisor:
Professor David C. Johnson
Chemistry Department
University of Oregon
Eugene, Oregon
davej@uoregon.edu

Andrew D. Shaller
Washington State University
Pullman, Washington

PNNL Host:
H. Peter Lu, FSD
Peter.Lu@pnl.gov

Supervisor:
Professor Alexander Dequan Li
Chemistry Department
Washington State University
Pullman, Washington
dequan@wsu.edu

Yiguang Wang
Central Florida University
Orlando, Florida

PNNL Host:
Theva Thevuthasan, EMSL
theva@pnl.gov

Supervisor:
Professor Lian An
Mechanical, Materials, and Aerospace
Engineering
Central Florida University
Orlando, Florida
lan@pegasus.cc.ucf.edu
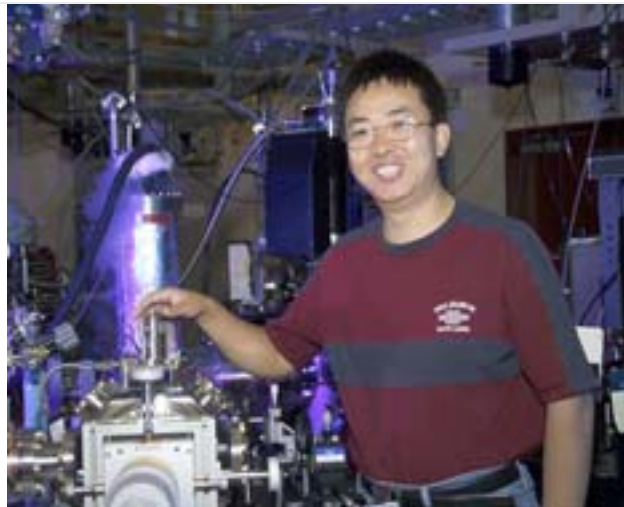
	Wei (David) Wei University of Texas Austin, Texas **PNNL Host:** Kenneth M. Beck, EMSL Wayne Hess, FSD kenneth.beck@pnl.gov **Supervisor:** Professor John White Chemistry Department. University of Texas Austin, Texas jmwhite@mail.utexas.edu
	Weixing Xu Central Florida University Orlando, Florida **PNNL Host:** Sarah D. Burton, EMSL sarah.burton@pnl.gov **Supervisor:** Professor Lian An Mechanical, Materials, and Aerospace Engineering Central Florida University Orlando, Florida lan@pegasus.cc.ucf.edu
	Dr. Zhenrong Zhang University of Texas Austin, Texas **PNNL Host:** Zdenek Dohnalek, FSD Zdenek.Dohnalek@pnl.gov **Supervisor:** Professor John White Chemistry Department. University of Texas Austin, Texas jmwhite@mail.utexas.edu
	FSD: Fundamental Sciences Directorate NSD: National Security Directorate
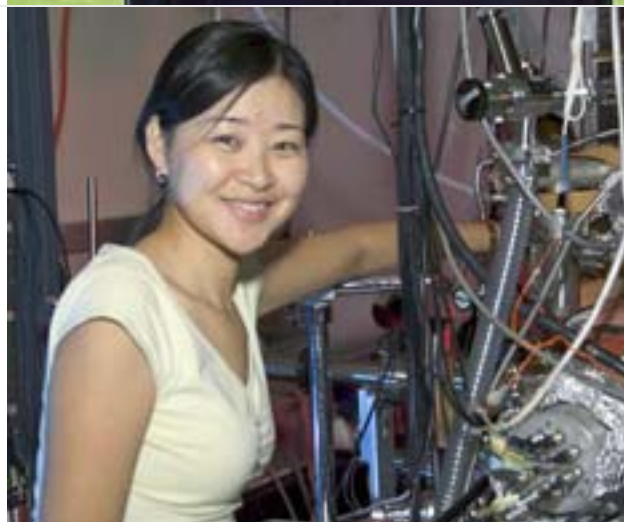
Table 3. 2005 Summer Research Institute Attendance by university

Aristotle University of Thessaloniki	1
Central Florida University	3
Florida State University	1
Purdue University	1
Rensselaer Polytechnic University	1
University of Hong Kong	1
University of Oregon	1
University of Texas	2
University of Washington	1
Utah State University	1
Washington State University	1

Benefits

As described above, participation in the Summer Research Institute required a significant investment in time and resources on the part of all parties involved. The only reason that a young scientist, a PNNL host, or an academic advisor would be involved is if they believed that their investment would be beneficial. We believe that the Summer Institute's structure promoted the likelihood of that success. In addition, the presence of these energetic, intelligent, well-educated, and highly motivated young scientists is a benefit for PNNL that cannot be easily measured. PNNL is in a rather remote location far from major urban centers and large academic institutions, and these young scientists were an absolute delight to have at the Laboratory. Their inquisitiveness, creativity, and willingness to learn helped stimulate PNNL staff to think in new, creative ways.

Measures of Success

The Summer Institute is a research enterprise. As such, its real success will only become apparent in the future. Further, the relatively short time that the young scientists were on campus at PNNL is only a small part of the story. We can already point, however, to a few early successes. First, although the applicant pool was limited, we did receive 16 outstanding applications. Invitations to participate in the institute were extended all 16 of these applicants, and they all accepted and completed the program. Second, all of the participants, PNNL mentors, and academic advisors or supervisors expressed enthusiasm about the institute at the outset and were generally more enthusiastic by the end of their respective summer appointments. In one case, the research carried out during the institute resulted in the participant being hired as a staff member at PNNL. Numerous presentations and manuscripts are being prepared for submission to peer-reviewed journals.

2004 Follow-Up

In last year's report, we stated that at least half-dozen papers were being prepared for publication as a result of the research performed at PNNL by Summer Research Institute participants. Currently (i.e., September 2005), there are still six to eight manuscripts in various stages of preparation as a consequence of work accomplished in 2004, but seven papers, which are listed in Table 4, have already been published in peer-reviewed journals. At least two presentations at national or international meetings were also produced—see Table 5. In addition, numerous internal PNNL reports have been generated.

The author lists from 2004 (see Table 4) also point to an additional and somewhat unexpected benefit of the Summer Research Institute. Those participants who were involved in laboratory work in EMSL were extremely facile in harnessing internal collaborative opportunities and resources. Thus many of the papers included unanticipated participation by PNNL staff members who were not hosts or otherwise involved in the institute.

Table 4. Peer-Reviewed Publications from 2004 Work Through August 2005

Alvarez, Jormarie,[a] R. Graham Cooks,[c] S. E. Barlow, Daniel J. Gaspar, Jean H. Futrell, and Julia Laskin.[b] 2005. "Preparation and *In Situ* Characterization of Surfaces Using Soft Landing in a Fourier Transform Ion Cyclotron Resonance Mass Spectrometer." *Anal. Chem.* 77,3452-3460.

Gologan, Bogdan, Jason R. Green, Jormarie Alvarez,[a] Julia Laskin,[b] and R. Graham Cooks.[c] 2005. "Ion/Surface Reactions and Ion Soft-Landing," *Phys. Chem. Chem. Phys.*,7**:** 1490-1500.

Yingge Du, Y,[a] S. Atha, R. Hull, James F. Groves,[c] Igor V. Lyubinetsky,[b] and Donald R. Baer. 2004. "Focused-Ion-Beam Directed Self-Assembly of Cu₂O Islands on SrTiO3(100)." *Applied Physics Letters* 84:5213-5215.

Lagutschenkov, Anita,[a] George S. Fanourgakis, Gereon Niedner-Schatteburg,[c] and Sotiris S. Xantheasa.[b] 2005. "The Spectroscopic Signature of the All-Surface to Internally Solvated Structural Transition in Water Clusters in the n=17–21 Size Regime." *J. Chem. Phys.* 122:194310.

Fung Suong Ou,[a] Laxmikant V. Saraf, and Donald R. Baer.[b] 2005. "Use of Hydrogen Bubble to Direct Pattern Microstructures of Porous Silicon.*" Appl. Phys. Lett.* submitted.

Lloyd, JA, Jeffrey M Spraggins,[a] Murray V Johnston,[c] and Julia Laskin.[b] 2005. "Peptide Ozonolysis: Product Structures and Proposed Mechanisms for Oxidation of Tyrosine and Histidine." *J. Amer. Soc. Mass Spectrum* submitted.

Tait, Steven L.,[a] Zdenek Dohnálek,[b] Charles T. Campbell,[c] and Bruce D. Kay. 2005. "N-Alkanes on MgO„100.... I. Coverage-Dependent Desorption Kinetics of N-Butane." *J. Chem. Phys*. 122:164707.

Tait, Steven L.[a] Zdenek Dohnálek,[b] Charles T. Campbell,[c] and Bruce D. Kay. "*N-Alkanes on MgO„100.... II. Chain Length Dependence of Kinetic Desorption Parameters for Small N-Alkanes.*" J. Chem. Phys. 122:164708.

Wang, Yiguang,[a] L Zhang, Y Fan, J. Luo, DE McCready, CM Wang,[b] and L An.[c] 2005. "Synthesis, Characterization, and Optical Properties of Pristine and Doped Yttrium Aluminum Garnet Nanopowders." *J. Am. Ceram. Soc.* 88:284-286.

a. 2004 Summer Research Institute Visitor
b. PNNL Host
c. Supervisor

Table 5. Presentations/Conference Papers
Ou, Fung Suong,[a] Laxmikant V. Saraf, and Donald R. Baer.[b] 2004. "Site-Specific Formation of Nanoporous Silicon on Micro-Fabricated Silicon Surfaces." Presented by Fung Suong Ou at MRS 2004 Fall Meeting, Boston, Massachusetts, on December 1, 2004. PNNL-SA-42481, Pacific Northwest National Laboratory, Richland, Washington.
Henager, C. H., Jr.,[b] E. A. Le[a], and R. H. Jones. 2004. "A Model Stress Analysis of Swelling in SiC/SiC Composites as a Function of Fiber Type and Carbon Interphase Structure." In *11th International Conference on Fusion Reactor Materials in Journal of Nuclear Materials*, no. Pt A, ed. Kohyama, A., 329-333 (2005) 502 - 506. Elsevier, Amsterdam, Netherlands.
a. 2004 Summer Research Institute Visitor
b. PNNL Host
c. Supervisor

Participant Survey

The following survey was sent to all of the Summer Institute participants (visitors, hosts, and advisors).

Interfacial and Condensed Phase Chemical Physics Summer Research Institute (ICPCPSRI): Follow-Up Questionnaire

Dear Colleague:

From my perspective, the second year of PNNL's ICPCPSRI went well. However, your perspectives are much more important and will largely determine the fate of this program. Therefore, I encourage each of you to take a few minutes to answer some questions and to append any additional comments, suggestions, etc., to your reply. I would appreciate reply by 16 October, even if it is incomplete. If at a later time, you wish to add anything, please do so.

Directions

Not every question applies to everyone, and it is not necessary to answer everything that does apply. The more complete your answers, the more useful they are. I may wish to use your comments in follow-on documentation, please indicate whether you wish for me to attribute the comments to your or would prefer to remain anonymous.

- May I quote you with attribution?

Section I. Contact Information

Please provide me with current contact information, your name address, e-mail, phone, etc.

- Are you willing to be contacted for further follow-up questions?

Section II: Measures of Success (or not)

PNNL mentors and faculty advisors

1. Was this summer's activity part of an on-going collaboration?

2. How likely is this summer's experience to contribute to future collaboration outside the auspices of the summer program?

3. Did the work contribute to your research or project aims? How?

All

4. How likely is this work to appear in publication(s), presentation(s)? (If you are planning to publish or present, please provide some detail: where, when, etc.)

5. (*Grad students only)* How likely is this work to contribute to your Ph.D. Thesis?

6. Were any new avenues of research opened?

7. Did your work here produce any intellectual property (IP) or is it likely to lead to IP development? (If yes, please give some description without disclosing the IP itself)

8. Would you recommend others to apply to or participate in this program?
Please add any additional comments you wish on the intellectual, technical or scientific success or shortcomings of the program.

Section III. The Experience

All

1. What aspects of the program did you feel were particularly good?

2. What can we do to improve the program?

3. (*Participants who visited PNNL)* What difficulties did you encounter coming here or during your stay?

Section IV. Comments

Please take a moment to add any additional comments, opinions or anecdotes about the program, your visit, the research, etc.

Thank you,

Stephan E. Barlow
Director
ICPCPSRI
(509) 376-9051
se.barlow@pnl.gov

Survey Results and Lessons Learned

As with last year, all of the participants who responded to the survey or who were polled informally were enthusiastic about the program. Everyone—visitors, PNNL hosts, and academic advisors or supervisors—felt that the program provided much value to its participants. All participants reported significant accomplishments during their stay at PNNL. Most also reported that the work initiated during the Summer Research Institute will continue in some form in the future.

The largest single area of difficulty was associated with PNNL's reorganization of the internal visitor and internship programs. The major problem encountered was sending firm offers to candidates in a timely fashion, which created some uneasiness on the part of the candidates. However, no one withdrew his or her application or was otherwise unable to participate on account of problems related to the reorganization. It appears likely that in future years, this problem will not recur. As discussed below, several features of the reorganization are likely to be beneficial to the Summer Research Institute.

Much of the reorganization was in response to recent changes in the U.S. tax code and the way it was interpreted. Our major challenge was to make sure the participants avoided any unnecessary requirements associated with these tax-code changes. Our participants came in through various PNNL Science and Engineering Education Office programs. Some of these programs required participation in a new "diversity" and "enrichment" series mandated by the education program office. This series was set-up for non-scientists who spend time at PNNL to gain exposure to a scientific environment, but it not applicable to the professional scientists who participate in the Summer Research Institute. However, in response to requests from our 2005 participants, we will organize one or two technical get-togethers to allow participants a technical area to grow in 2006.

A second area of confusion was associated with the on-line application process. A number of participants apparently were confused about their summer support and expected the Summer Research Institute to provide a full stipend. Budgetary constraints as well as our general philosophy about support and the reorganization discussed above all make it difficult for us to provide such support. We will be revising our on-line application process to address this issue. There also was one case in which an individual lost his university support just prior to coming to PNNL. Fortunately, for this participant, we were able through a variety of sources to secure the necessary extra funding from outside sources (i.e., non-Summer Resource Institute sources).

The final area of difficulty for some participants involved arranging for local housing. In 2006, we will be more aggressive in getting participants to make housing arrangements as early as possible, thereby avoiding unnecessarily high costs or long commutes. Some participants also were confused about what travel expenses we could or could not cover. Again, in the future, we will attempt to clarify these issues during the application process.

This year we received noticeably fewer inquiries and applications than in 2004. We attributed this drop-off to the fact that our initial program announcement was made early in December 2004 and many would-be applicants simply forgot about it over the holiday season. This year we intend to send the first announcement out in early December and follow-up with a second reminder early in January.

Continuing a tradition started in 2004, Dr. Barlow, Director of the Summer Research Institute, hosted two weekend barbeques at his home. These events were quite successful and gave everyone the opportunity to meet in a non-working, social environment. Dr. Barlow intends to continue this "tradition" in 2006.

Reports

Technical Reports

The remainder of this document is devoted to the technical reports provided by each young scientist. Some of these are single paragraph abstracts and, therefore, have rather limited content. Other reports, however, are nearly complete papers. These documents are "as received," apart from minor formatting changes in some cases. We have made no effort to edit or evaluate these reports. Given the limited distribution intended for this report, none of the results in these reports should be considered "published" by virtue of appearing here.

The dissociation of protonated peptide radical cations

Ivan Keung Chu
Hong Kong University
Hong Kong

and

Julia Laskin and Gene H. Futrell
Pacific Northwest National Laboratory
Richland, WA

I have enjoyed productive collaborative experience during the Summer Research Institute fellowship, funded recently by the Institute in Interfacial and Condensed Phase Chemical Physics, Pacific Northwest National Laboratory in summer of 2005. Our collective efforts have lead to successful execution of the proposed project and result in significant contribution toward understanding of the gas phase chemistry of novel radical cationic peptides. The dissociation of peptide radical cations has been used to model molecular wires in studies of charge transfer in biological systems[1] and to investigate intramolecular vibrational redistribution in these systems.[2] Capture of low-energy electrons, which results in electron capture dissociation (ECD), is an alternative method[1] for converting a multiply protonated peptide into a protonated peptide radical cation, $[M + nH]^{\bullet(n-1)+}$, and has attracted considerable interest.[3] The dissociation pathways of protonated species have been studied extensively and the fragmentation of protonated peptides is used routinely for generating sequence tags for protein identification and even complete *de novo* sequencing in proteomics analysis.[4] In contrast to protonated peptides that fragment predominantly by the cleavage of a peptide bond to form y and b ions, the dissociation of protonated peptide radical cations requires cleavages of $N–C_\alpha$ bonds to form predominantly c and z product ions.[3-4] Fragmentation of peptide radical cations provides an analytical means for *de novo* sequencing, especially for locating post-translational modifications, improves the sequence coverage relative to that attainable from protonated species.[6] Despite some recent advances in studies of the reactivities of molecular radical cationic oligopeptides, their fragmentation mechanisms are not well understood. Comprehensive studies for these systems have been hindered by difficulties in generating gas phase peptide radical cations. Recently, we developed a new approach for synthesizing peptide radical cations through the gas phase decomposition of peptide–Cu(II)–ligand complexes,[5] thus, this process allows us to initiate the exploration of the gas phase chemistry of these species using a unique 6 Tesla Fourier Transform Ion Cyclotron Resonance (FTICR) Mass Spectrometer at PNNL for the first time during the Summer Research Institute fellowship.

The initial phase of our project has devoted to explore complexes system toward generating novel radical cationic angiotensin III(DRVYIHPF) in the gas phase. We have successfully produced radical cationic $M^{\bullet+}$ (where M is RVYIHPF) though one-electron transfer from the peptide to ligated copper(II) amine complexes via up-front collision induced dissociation. The ability to form peptide radical cations in the gas phase raises a question about their stability relative to those of the corresponding protonated species and smaller organic radical cations. Are the energetics of dissociation of these species similar to the dissociation energetics of smaller radical cations? It is known that the bond dissociation energy for organic radical cations is in the range 2.5–6 eV,[6] while dissociation of protonated peptides requires only 0.8–2 eV.[7] This relative ease of dissociation of protonated peptides has been attributed to the presence of a proton that migrates along the backbone of the peptide and weakens the peptide bond in its vicinity—the "mobile proton model".[8] Studies of peptide radical cations can help to bridge the gap between small organic cations and protonated peptide ions and facilitate an understanding of the factors that govern bond strengths in ionic
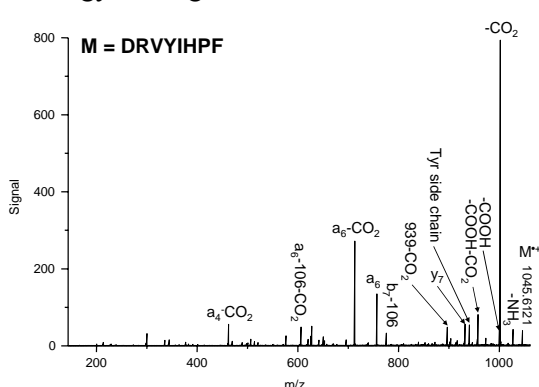
Figure 1

systems. We found similarities and differences exist in the fragmentation behaviour of angiotensin III radical cations $M^{\bullet+}$ and protonated peptides $[M + H]^+$ under surface induced dissociation (SID). The diverse range of fragmentations of peptide radical cations is demonstrated by the SID spectrum of $M^{\bullet+}$ displayed in Figures 1. It is apparent that fragmentation of $M^{\bullet+}$ results in facile charged-induced cleavage of the tyrosine side chains and neutral loss of CO_2 of DRVYVHPI $^{\bullet+}$ and both radical- and charged-induced fragment ions $[a_n - H]^{\bullet+}$, $[b_n - H]^{\bullet+}$, $[b_n + H]^{\bullet+}$, and $[z_n + H]^{\bullet+}$, which is in contrast to the dissociation of $[M + H]^+$ that leads to conventional y_n^+, b_n^+, and a_n^+ ions.

We have utilized time- and energy-resolved SID studies on the dissociation of molecular radical cationic angiotensin III and its derivatives. The dissociation of large peptide ions of RVYVHPF $^{\bullet+}$ is driven by the kinetic shift (KS),[2] the internal energy in excess of the dissociation energy that is required to produce the detectable dissociation of a polyatomic ion on the timescale of a mass spectrometer. Coupling SID with an FT-ICR mass spectrometer provides the distinct advantages provided by long and variable reaction times (milliseconds to seconds), which both greatly reduce the kinetic shift and allow access to the lowest-energy dissociation pathways for such large peptides. Futrell and Laskin have developed a novel approach for studying the energetics and dynamics of the dissociation of large complex molecules by using surface-induced dissociation (SID) in conjunction with FT-ICR MS.[9] This approach involves RRKM modeling of time- and energy-resolved MS/MS data obtained using collisional activation. Collision energy-resolved studies provide important information on the appearance energies of different product ions and on the amount of energy required for dissociation of the precursor radical ion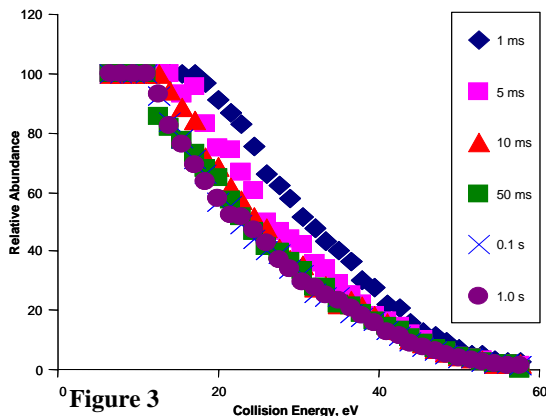s of RVYIHPF $^{\bullet+}$. Another dimension is added to SID experiments by conducting kinetic studies through varying the delay time between the ion–surface collision and the analysis of the
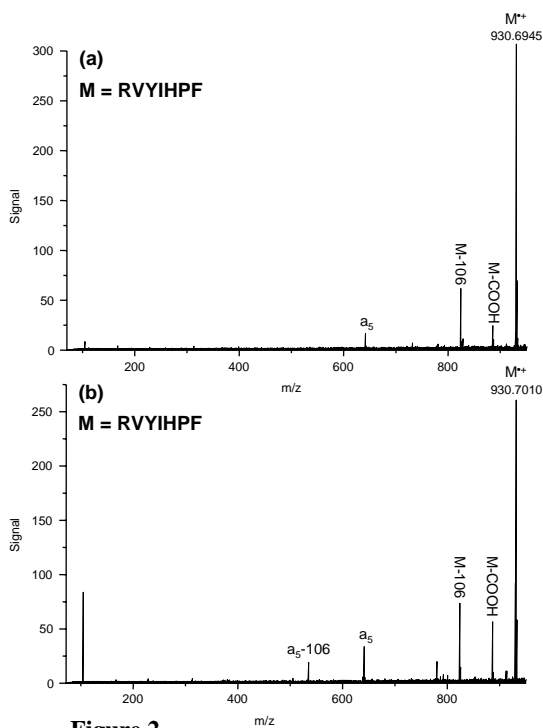
Figure 2

resulting products. RVYIHPF$^{\bullet+}$ was a good candidate on our initial investigations, partly because they have a large number of vibrational degrees of freedom, which results in slow dissociation; and partly because an ion of almost identical molecular weight—protonated angiotensin III(RVYIHPF) analogues— has been studied extensively and validated using the same methodologies in which could be used as a reference to calibrate the energy-transfer efficiency in collision of ions with the surface.[9] Figure 2a-b presents an example of time-dependent CID spectra of the $M^{\bullet+}$ ion which differ only in delay time between the ion–surface collision and the analysis of the resulting products due to the kinetic shift. Figure 3 displays survival curve of precursor ion of RVYIHPF$^{\bullet+}$ by plotting the relative intensity of the precursor ion verse the SID collision energy at six different delay times (1m, 5ms, 10ms, 50ms, 0.1s and 1s) These curves demonstrated that short delay times have shifted the curve to higher collision energies. We are making progress with analysis of time- and energy-resolved SID data, combined with an RRKM-

Figure 3

17

based modeling approach to conduct the first studies on the energetics of radical cationic peptide dissociation. We will present the results of this fundamental gas phase ion chemistry research at the 54th ASMS conference on mass spectrometry to be held in May in Seattle, USA, 2006. Our results are now in preparation for the publications. (Please Refer to Appendix I) The key experimental results were very successful and have opened up many research opportunities. Although only the first few M$^{\bullet+}$ angiotensin derivatives have been examined using this time- and energy-resolved, our results have demonstrated a great potential for allowing the detailed elucidation of fragmentation energetics and mechanisms for large radical cationic peptides.

With the preliminary demonstration of kinetic studies with molecular radical angiotensin, we will extend our investigation on the reactivity of radical cationic peptides using Ion Trap quadrupole tandem mass spectrometry in HKU and Surface induced Dissociation FT-ICR in Pacific Northwest National Laboratory (PNNL). The latter is in collaboration with Prof. Jean H. Futrell, and Dr. Julia Laskin (JL) in PNNL. A research proposal on investigating the dissociation of radical cations of oligopeptides has been funded for 2005 Competitive Earmarked Research Grants application. We are also planning to extend the work to anionic radical cationic angiotensin III using similar methodologies. Studies of odd-electron radical cationic M$^{\bullet+}$, [M+2H]$^{\bullet+}$, and anionic [M-2H]$^{\bullet-}$ peptides can help to bridge the gap between small cations and protonated peptide ions and facilitate a better understanding on the role of hydrogen atom that governs radical peptide fragmentation. A Ph.D student, Mr. Siu Shiu On will be responsible to conduct CID experiments and modeling of he low-energy radical anionic angiotensin III in the form of [M-2H]$^{\bullet-}$ in collaboration with JL.

References:
1. Schlag, E .W., Lin, S. H., Weinkauf, R., Rentzepis, P. M. Proc. Natl. Acad. Sci. USA **1998,** 95, 1358-1362.
2. Cui, W.; Hu, Y.; Lifshitz, C. Eur. Phys. J. D **2002**, 20, 565–571.
3. (a) Zubarev, R. A.; Kelleher, N. L.; McLafferty, F. W. J. Am. Chem. Soc. **1998**, 120, 3265–3266. (b) Kjeldsen, F.; Haselmann, K. F.; Sorensen, E. S.; Zubarev, R. A. Anal. Chem. **2003**, 75, 1267–1274. (c) Mann, M; Jensen, O. N. Nat. Biotechnol. **2003**, 21, 255–261. (d) Zubarev, R. A. Mass Spectrom. Rev. **2003**, 22, 57–77. (e) Zubarev, R. A. Curr. Opin. Biotechnology **2004**, 15, 12–16.
4 (a) Fenn, J. B.; Mann, M.; Meng, C. K.; Wong, S. F.; Whitehouse, C. M. Science 246, 64-71. (b) Tanaka, K.; Waki, H.; Ido, Y.; Akita, S.; Yoshida, Y.; Yohida, T. Rapid Commun.Mass Spectrom. **1988**, 2, 151-153. (c) Aebersold, R.; Goodlett, D. R. Chem. Rev. **2001**, 101, 269-295.
5. (a) Chu, I. K.; Rodriquez, C. F.; Lau, T. C.; Hopkinson, A. C.; Siu, K. W. M. J. Phys. Chem. B **2000**, 104, 3393–3397. (b) Chu, I. K.; Rodriquez, C. F.; Lau, T. C.; Hopkinson, A. C.; Siu, K. W. M. J. Am. Soc. Mass Spectrom. **2001**, 12, 1114–1119. (c) Bagheri-Majdi, E.; Ke, Y.; Orlova, G.; Hopkinson, A. C.; Siu, K. W. M. J. Phys. Chem. B **2004**, 108, 11170–11181.(d) Chu, I. K.; Siu, S. O.; Lam, C. N. W.; Chan, J. C. Y.; Rodriquez, C. F. Rapid Commun. Mass Spectrom. **2004**, 18, 1798–1802.
6. McLafferty, F. W.; Turecek, F. Interpretation of Mass Spectra, 4th Ed., University Science Books, 1993.
7. (a) Laskin, J. Eur. J. Mass Spectrom. **2004**, 10, 259–267. (b) Schnier, P. D.; Price, W. D.; Jockush, R. A.; Williams, E. R. J. Am. Chem. Soc. **1996**, 118, 7178–7189. (c) Schnier, P. D.; Price, W. D.; Strittmatter, E. F.; Williams, E. R. J. Am. Soc. Mass Spectrom. **1997**, 8, 771–780.
8 (a) Jones, J. L.; Dongre, A. R.; Somogyi, A.; Wysocki, V. H. J. Am. Chem. Soc. **1994**, 116, 8368–8369. (b) Dongre, A. R.; Jones, J. L.; Somogyi, A.; Wysocki, V. H. J. Am. Chem. Soc. **1996**, 118, 8365–8374. (c) Rodriquez, C. F.; Cunje, A.; Shoeib, T.; Chu, I. K.; Hopkinson, A. C.; Siu, K. W. M. J. Am. Chem. Soc. **2001**, 123, 3006–3012, and references cited therein.
9. (a) Laskin, J.; Denisov, E.; Futrell, J. H. J. Am. Chem. Soc., **2000**, 122, 9703–9714. (b) Laskin, J.; Denisov, E.; Futrell, J. H. Int. J. Mass Spectrom. **2002**, 219, 189–201. (c) Laskin, J.; Bailey, T. H.; Futrell, J. H. J. Am. Chem. Soc. **2003**, 125, 1625–1632. (d) Laskin, J.; Bailey, T. H.; Futrell, J. H. Int. J. Mass Spectrom. **2004**, 234, 89–99.

Appendix I:
Below is a list of new developments related to our ongoing collaborations:
1. A research proposal on investigating the dissociation of radical cations of oligopeptides has been funded for 2005 Competitive Earmarked Research Grants application.
2. Publications that are in preparation are attached with this report.

i) S. O. Siu, Ivan K. Chu, Julia Laskin, Jean H. Futrell., "Fragmentation of radical cationic Angiotensin III Derivatives by means of FTICR-SID" in preparation.

ii) C. N.W. Lam, Ivan K. Chu, Julia Laskin, Jean H. Futrell, "Time and Energy- Resolved Surface Induced Dissociation of Radical Cationic Angiotensin III Derivatives Ions" in preparation.

iii) Ivan K. Chu, S. O. Siu, Julia Laskin, Jean H. Futrell, "Formation and Dissociation of radical anionic Angiotensin III Derivatives in the gas phase" in preparation.

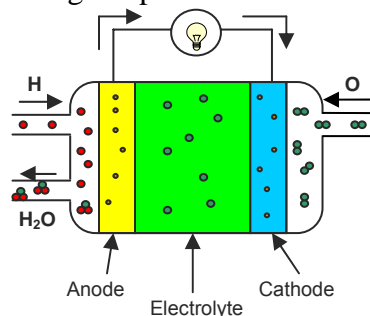# Atomic Structure of Nanoscale Layered Ceramic Films

Michael Dyer and Anteer El-Azab   Fei Gao
Florida State University   and   Pacific Northwest National Laboratory
                                           Richland, WA

I. Introduction

The oxide materials ceria (CeO_2) and zirconia (ZrO_2) are useful materials in many applications. Currently of prime interest is the ability of these two materials to conduct oxygen ions. This ability makes ceria and zirconia particularly good candidates for use in devices such as oxygen sensors and solid oxide fuel cells.

Fuel cells use the reaction of hydrogen and oxygen to produce an electrical current, with water as a byproduct. Several different types of fuel cells have been developed; the solid oxide fuel cell holds particular promise as an industrial power generator. The current operating temperature for this type of fuel cells is on the order of 1000 °C. Most of this heat is generated in the ceramic electrolyte; if the ionic conductivity of the electrolyte can be improved, this would result in a reduction of the operating temperature of the fuel cell. Typically the electrolytes in solid oxide fuel cells are made from bulk ceria or zirconia doped with materials such as yttria (Y_2O_3) or gadolinia (Gd_2O_3). The introduction of the doping agent into the crystal structure produces a charge imbalance, which is rectified by the creation of oxygen vacancies in the lattice. These oxygen vacancies greatly increase the mobility of oxygen ions in the crystal. Also the addition of dopant to zirconia causes the crystal to stabilize to the cubic fluorite structure at room temperature. This helps to prevent cracking and fracture of the crystal due to temperature change. However, it has been observed that thin layers of pure zirconia deposited on a substrate can exist in the cubic structure at room temperature.

Figure 1: Solid Oxide Fuel Cell

Recent studies have shown that a significant increase in the ionic conductivity can be achieved with a structure consisting of alternating thin films of doped ceria and zirconia[1]. The exact mechanism for this increase is not well understood, but could be related to the interface structure between the ceria and zirconia layers. There are two interface classifications of interest in the ceria-zirconia system; semicoherent and coherent. For very thin films the system is capable of absorbing the entire lattice mismatch by strain, resulting in a well-ordered interface in which each layer has the same lattice parameter; this is

Incoherent
Each layer maintains its natural spacing

Semicoherent
Layers partially strain to account for mismatch

Coherent
Layers strain until spacing is completely matched
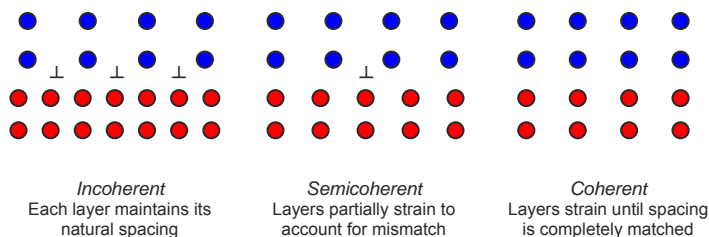
Figure 2: Types of interfaces

known as a coherent interface. As the film becomes thicker, dislocations form periodically along the interface. These dislocations help relieve the strain energy and so the system is called semicoherent. A third type of interface, incoherent, exists when the layers are so thick that none of the mismatch is compensated by strain.

Using the molecular dynamics (MD) method, we have examined the structure of coherent and incoherent interfaces in order to gain more knowledge about the ionic conductivity in coherent and semicoherent ceria-zirconia films. A combination of computational studies and experimentation was used to investigate the mechanism of phase transformation in these films.

II. Ceria-Zirconia Interface Simulation

Since ceria and zirconia are primarily ionically bonded materials, they can be modeled reasonably with well established two-body potentials. Some studies have also incorporated more complex elements, such as shell model polarization. While being more correct from a first-principles point of view, such models require a large increase in computing time while showing little increase in accuracy over simpler pair terms. We chose a standard potential consisting of a Coulomb term for long range forces plus a Buckingham term to account for shorter ranged forces:

$$V = \frac{q_i q_j}{r} + A e^{-r/\rho} - \frac{C}{r^6}$$

This potential has the advantage of a quick computing time, as well as a large body of potential parameters that have been derived for the elements of interest. The particular parameters used in this study were taken from previous research by Zacate[2] and Minervini[3] and are listed in Table 1. The actual calculation was performed using the molecular dynamics code DL_POLY[4].

	Zr-O[2]	Ce-O[3]	Gd-O[2,3]	O-O[2,3]
A	1502.11	1809.68	1885.75	9547.96
ρ	0.3477	0.3547	0.3399	0.2192
C	5.1	20.4	20.34	32

Table 1: Potential parameters used for interface simulation

Simulations were performed first on coherent and then on semicoherent systems in order to isolate the effects of dislocations on the interfacial structure. Also, the simulation was run for each interface using pure and doped layers. Doping was incorporated by random substitution of the cations in each layer with gadolinium at a concentration of approximately 12 at%. Correspondingly, a number of oxygen vacancies equal to twice the number of gadolinium atoms were randomly incorporated in order to provide electrostatic neutrality.

Before attempting to analyze the interface structure, the equilibrium structure of pure and doped ceria and zirconia was determined for a 4x4x4 unit cell at a temperature of 0 K and pressure of 0 kbar. The number of particles, pressure, and temperature were all fixed (NPT). The results of these simulations were used to determine the lattice parameter of each material. This information was then used to help construct

	Lattice Parameter (Å)
ZrO_2	5.11623
ZrO_2, 12at% Gd	5.15563
CeO_2	5.40978
CeO_2, 12at% Gd	5.42203

Table 2: Calculated lattice parameters for ceria and zirconia single crystals

the ceria-zirconia interface. This also provided a check on the accuracy of the potential and simulation method through comparison of the experimental lattice parameter against reference values.
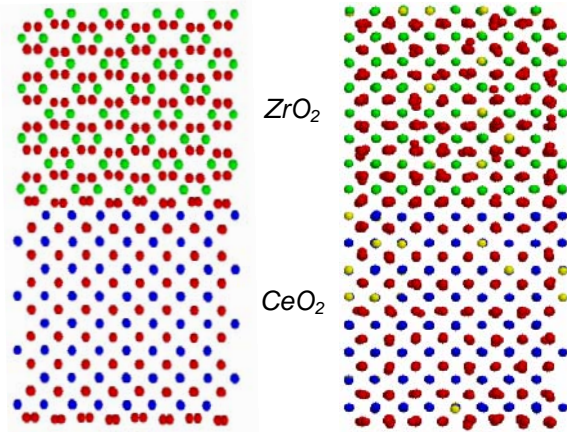

Figure 3: Comparison between pure (left) and doped (right) coherent interface film structures for 2nm thick layers

The coherent interface was constructed as a column with a depth and width of 4 unit cells and varying thickness from 4 to 16 unit cells, with each layer being of equal thickness. This corresponds to an approximate layer thickness range of 1 to 4 nm. For all thicknesses of pure ceria-zirconia, the zirconia layer underwent a phase transformation to what appears to be an orthorhombic structure, possibly of space group Pca2$_1$[5]. This structure does potentially exist on the zirconia phase diagram as a possible high-pressure phase, but likely occurred here due to a defect in the potential. Ceria layers remained in the cubic form, in agreement with the actual material. The addition of gadolinium to both layers did stabilize the zirconia to a cubic structure. The stabilizer also had the effect of increasing the amount of disorder in the oxygen sublattice, particularly in the zirconia layers. This disorder is expected as the oxygen ions change position to compensate for the oxygen vacancies introduced by the addition of the stabilizer. A distortion of the lattice parameter perpendicular to the interface plane was also observed in both systems due to the Poisson effect. The perpendicular lattice parameter of ceria increased slightly, while the lattice parameter of zirconia decreased slightly. Again, this type of distortion is in good agreement with theory.

To simulate the semicoherent interface, the size of the simulation cell was chosen so that the zirconia layer would have more atomic planes along the width of the cell than the ceria layer, resulting in the formation of a dislocation. The total width of the cell was approximately equal for each layer however, since zirconia has a slightly smaller lattice parameter than ceria. This allowed periodic boundary conditions to be validly applied to the system. Again, a range of layer thicknesses was tested,
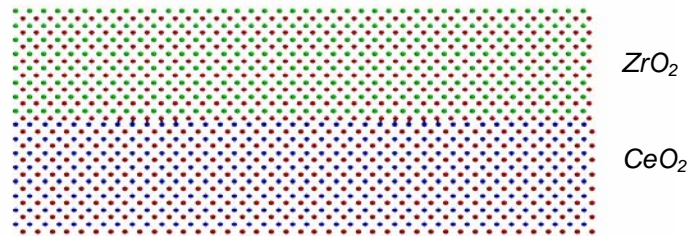
Figure 4: Inital atomic structure of 2nm layers with a semicoherent interface

from 2 to 15 nm, for both doped and pure. Phase transformation was observed in pure zirconia layers, apparently to the same orthorhombic structure as seen before. Near the dislocation, however, the structure changed to a cubic or possibly a tetragonal form. The orthorhombic structure became less apparent at larger layer

thicknesses. Also, a significant variation in the dislocation structure could be seen as the layer thickness changed. At thinner layers, the region around the dislocation was highly disordered. As thickness increased, the structure became more organized and a clear dislocation formed in the cation lattice. This behavior most likely occurred due to the artificial
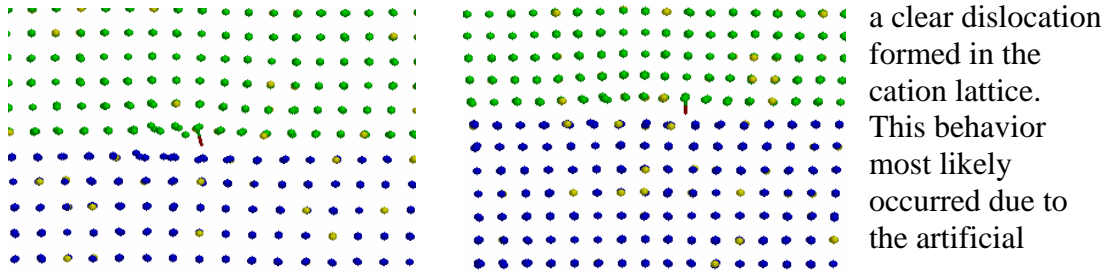
Figure 5: Comparison of dislocation structures of doped semicoherent layers at 2 nm (left) and 9 nm (right) film thicknesses

imposition of the dislocation onto the crystal structure. The critical thickness at which the interface changes from coherent to semicoherent is not experimentally known but can be estimated to be around 4-5 nm for stacked layers. The simulated structure showed a large amount of disorder and no clear dislocation at thicknesses under 6 nm, consistent with this estimation. Also, some disorder may have been caused by the change in crystal structure in the zirconia layer. This is supported by results from the doped crystals, which do show less disorder than pure at very small thickness, although the disorder is still apparent.

II. Cubic Stabilization of Thin Zirconia Films

Pure zirconia normally exists in three phases depending on temperature: a low temperature monoclinic phase, a high temperature tetragonal phase, and a very high temperature cubic phase. This can be a concern in high temperature use of zirconia as the phase transition will cause cracking and fracture upon cooling. To avoid such destructive phase transitions, a stabilizing element is added. Depending on the amount and type of stabilizer added, the zirconia will stabilize to either the tetragonal or cubic form. As mentioned previously, stabilization also serves to increase the ionic conductivity of the zirconia by introducing oxygen vacancies into the crystal. In fact, previous simulation study by Fabris et al., has suggested that oxygen sublattice distortion caused by the vacancies is the primary mechanism of the stabilization[6]. Stabilization to the cubic structure has also been observed in thin zirconia films deposited on sapphire substrates[7]. Cubic zirconia films have successfully been deposited onto r-cut sapphire substrates up to a thickness of 40 nm before the precipitation of a second phase.

The increase in ionic conductivity caused by the addition of a stabilizer is well known; it increases with dopant concentration, then peaks at about 20 at% yttrium[8]. At any greater concentration than this the conductivity decreases. An analogous behavior is seen in the multilayer ceria-zirconia system; conductivity increases with decreasing layer thickness until the thickness reaches a value of about 15 nm, then conductivity begins to decrease[1]. Knowing that there is a close relationship between dopant stabilization and ionic conductivity seems to imply that there could be a similar relationship between them mechanism of stabilization in pure thin films and the conductivity. A combination of simulation and experiment was used to examine this mechanism. First, simulation was used to attempt to determine whether the

stabilization is caused by sizing or by mismatch strains at the interface. Then experiments were performed to approximately determine the critical thickness of stabilization on a yttrium stabilized zirconia (YSZ) substrate.

MD Simulation

The first step taken to determine whether the stabilization is an interfacial strain effect was to first eliminate the possibility that it is purely a sizing effect. Crystal structure changes due to grain sizing are well documented; zirconia itself has been observed in a tetragonal structure at low temperatures in grain sizes of < 30 nm [9]. A similar effect could occur in a single free film of zirconia. To test this, various thicknesses of pure zirconia were simulated using DL_POLY. The simulation cells used were orthorhombic with a buffer zone at each surface, allowing periodic boundary conditions to be applied. This resulted in the simulation of single layers of zirconia with infinite length and width but finite thickness. A constant volume and temperature (NVT) ensemble was used to maintain the size and shape of the simulation cell.
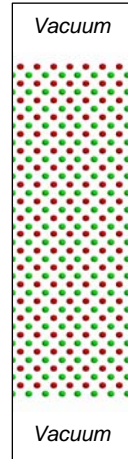
Figure 7: Initial configuration of 5nm film showing buffer layers added to approximate free surfaces

The simulation of phase transitions by molecular dynamics is often challenging due to the limitations of the interatomic potentials used. For zirconia, no potential currently exists that is capable of accurately representing all three of the low pressure phase. Most potentials are tailored to a specific crystal structure, generally the cubic. Several attempts have made to model multiple phases, but these have proven to be inaccurate, computationally expensive, or both. Schelling et al., however, have developed a Coulomb plus Buckingham potential[10], based on the Zacate and Minervini potentials, which reproduces both the tetragonal and cubic structures.

	Zr-O	O-O
A	1502.11	9547.96
ρ	0.345	0.224
C	5.1	32

Table 3: Potential parameters developed by Schelling et al.[10]

Using this potential, the phase transition from tetragonal to cubic can be seen in the position change of the oxygen ions and in the dimensions of the zirconia unit cell.

Using these parameters, the film atomic structure was simulated for 0K and 300K at thicknesses of 5 nm up to 15 nm. Judging from the position of the oxygen ions in the 5 nm and 7 nm thicknesses, the atomic structure of the films was probably tetragonal. Above 10 nm, the tetragonal structure transformed to the orthorhombic structure previously seen, but only at 300K. These simulations seem to indicate that zirconia films will not stabilize without being deposited onto some substrate. However, this
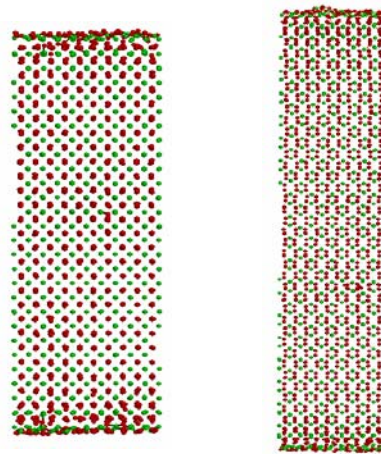
Figure 6: Atomic structure of 7nm (left) and 10nm (right) single zirconia films at 300 K

conclusion depends fully on the accuracy of the potential used; the appearance of the orthorhombic phase may indicate that the potential is not entirely realistic in this situation.

Experimental Procedure

Knowing that the stabilization is probably a mismatch-related effect, an experimental investigation was undertaken to determine the critical thickness of stabilization on a ytrrium-stabilized zirconia (YSZ) substrate. The difference between this critical thickness and the critical thickness determined for sapphire may help to explain the stabilization mechanism. Pure zirconia was deposited on 1cm x 1cm YSZ substrates by rf reactive sputtering. In this method, a pure zirconium target was sputtered onto YSZ in the presence of oxygen gas, causing the formation of a ZrO_2 film on the substrate. Oxygen flowed into the chamber at a rate of 3.0 sccm; argon, the sputtering gas, flowed into the chamber at 10 sccm. The rf power used was 100 watts, and prior to deposition the substrates were heated to 600 °C to encourage single-crystal epitaxial growth. Test depositions showed the growth rate under these conditions to be 1.389 Å/min. X-ray diffraction (XRD) analysis of the two test films, deposited on YSZ (111) substrates, showed only cubic structure at thicknesses of 73Å and 146Å. To ensure that stabilization was not caused by diffusion of yttrium into the film from the substrate, X-ray photoelectric spectroscopy (XPS) was performed on both test samples. XPS analysis indicated a yttrium concentration of no more than 0.11% in either film, well below the amount required to produce cubic structure throughout the film. Also, the concentrations determined by XPS showed that the concentration of oxygen was about 65.8% in both films. This is slightly below the ideal stoichiometric value of 66.7% oxygen, possibly indicating the presence of some oxygen vacancies in the film. However, this amount of oxygen vacancies is still too low to affect the crystal structure significantly.

After these initial tests, films were deposited on YSZ (100) substrates at various thicknesses in an attempt to determine the critical thickness of stabilization. At a thickness of 444Å, XRD analysis still detected no presence of a second monoclinic phase. Additionally, the XRD plot showed a dynamic scattering pattern which is indicative of high quality single crystal epitaxy. This rules out cubic stabilization due to any grain sizing
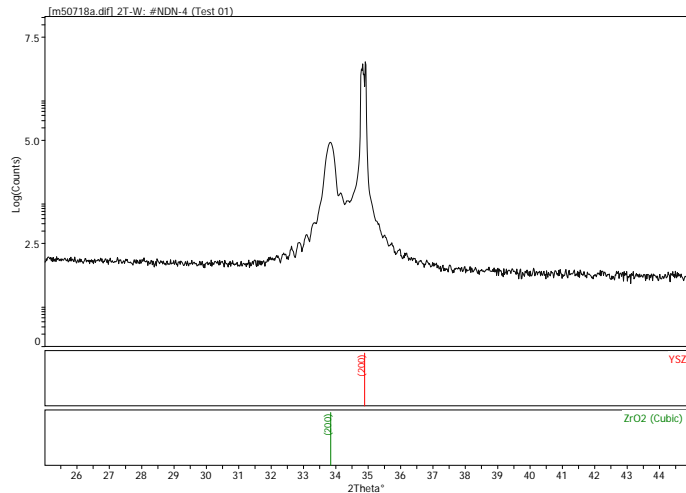
Figure 8: XRD spectra of 444Å cubic zirconia film on YSZ (100)

effects. It is important to note that it is difficult to distinguish between the cubic and tetragonal phases by XRD; however, previous observation indicates that a second phase appearing in the film structure would probably be monoclinic[7], which is easily recognizable by XRD.

At this point it is clear that the critical thickness on YSZ will be greater than the 40 nm exhibited on r-cut sapphire. This seems to imply that the much lower mismatch between ZrO_2 and YSZ (0.65% compared with 6.09% for ZrO_2-sapphire) is beneficial for the formation of thicker cubic layers. This implies a possible relationship between stabilization and the interfacial misfit dislocations; there may be an optimal dislocation spacing range that interacts with the epitaxial strains to help form cubic-ZrO_2. Generation of thicker films that reach the critical thickness will help to clarify this behavior. Also, a transmission electron microscopy study of the film in order to determine the dislocation structure could be useful.

References

1. S. Azad, O.A. Marina, C.M. Wang, L. Saraf, V. Shutthanandan, D.E. McCready, A. El-Azab, J.E. Jaffe, M.H. Engelhard, C.H.F. Peden, and S. Thevuthasan, Applied Physics Letters 86, 131906 (2005).
2. M.O. Zacate, L. Minervini, D.J. Bradfield, R.W. Grimes, K.E. Sickafus, Solid State Ionics 128, 243 (2000).
3. L. Minervini, M.O. Zacate, R.W. Grimes, Solid State Ionics 116, 339 (1999).
4. W. Smith, T.R. Forester, J. Mol. Graphics 14, 136 (1996).
5. J.K. Dewhurst, J.E. Lowther, Phys. Rev. B 57, 741 (1998).
6. S. Fabris, A.T. Paxton, M.W. Finnis, Acta Materialia 50, 5171 (2002).
7. S.C. Moulzolf, Y. Yu, D.J. Frankel, R.J. Lad, J. Vac. Sci. Technol. A 15, 1211 (1997).
8. M. Filal, C. Petot, M. Mokchah, C. Chateau, J.L. Carpentier, Solid State Ionics 80, 27 (1995).
9. G. Baldinozzi, D. Simeone, D. Gosset, M. Dutheil, Phys. Rev. Lett. 90, 216103 (2003).
10. P.K. Schelling, S.R. Phillpot, D. Wolf, J. Am. Ceram. Soc. 84, 1609 (2001).

A multielement spectrometer for studying the momentum transfer dependence of nonresonant x-ray Raman scattering

T.T. Fister[1], G.T. Seidler[1,*], L. Wharton[1], A.R. Battle[1], T.B. Ellis[1],
J.O. Cross[2], A. Macrander[2], T. Tyson[3] and Qing Qian[3]

[1] Physics Department, University of Washington, Seattle, WA 98195
[2] Advanced Photon Source, Argonne National Labs, Argonne IL
[3] NJXRS Tech, Trenton NJ zip

Non-resonant x-ray Raman scattering (XRS) is the inelastic scattering of hard x-rays from the core shell of low-Z elements or the less tightly bound shells of heavier elements. In the limit of low momentum transfer, q, this couples to the same transition matrix element as is measured in x-ray absorption spectroscopies (XAS). However, unlike XAS, which is almost exclusively limited to dipole transitions ($\Delta l = \pm 1$) for elements with Z < 100, XRS at higher q can often access higher order multipole transitions. These previously forbidden transitions can help separate the symmetry of various contributions to the local density of states. The main drawback of XRS is its low cross section — a problem that is compounded for a q-dependent study. To address this issue, we have constructed a multielement spectrometer to measure XRS at ten different values of q simultaneously. We report here on the design and performance of this apparatus.

(*) Corresponding author: seidler@phys.washington.edu
8/2/05

I. Introduction

Inelastic x-ray scattering (IXS) has a rich history [**2001 Bergmann ref**] and plays a key role in many parts of contemporary research in molecular and condensed phases of matter. [**1-3**] Multiple beamlines at x-ray synchrotrons worldwide are now dedicated to the measurement of various different types of IXS, with each instrument reflecting the interests of their developers and users through different energy resolutions, momentum transfers, monochrometer bandwidths, and scanning modalities. [**refs**]

One type of IXS measurement which is poised to play a growing role in structural and electronic studies is the inelastic scattering from the core-shells of low-Z elements or the less tightly bound shells of heavier elements; this IXS is often called non-resonant x-ray Raman scattering (XRS). While critical, early XRS experiments were performed at the 2nd-generation synchrotrons [**ref**], it is only with the advent of the 3rd-generation synchrotron x-ray sources that the low cross-section and frequently high background can be overcome to allow XRS measurements in a wide range of materials. This has led to a steady increase in the applications of XRS [**core dump**] and in the development of instrumentation optimized for XRS measurements. To date, several XRS spectrometers have been built which use multiple spherically-bent analyzers to increase the collection angle for the IXS resulting in faster measurements. [**refs**] However, these instruments generally operate only in the low-q regime, integrate over q, or require realignment and retuning to move between different q.

We report here a novel instrument which has been optimized for simultaneous measurement of XRS at multiple q, for low background from stray scattering, and for ease and diversity of use by the general users of the light source. Our apparatus uses 10 spherically-bent Si analyzers, each of which is matched with an independent detector.

The analyzers collect scattered radiation at a wide range of q, thus providing 10 simultaneous but independent measurements of q-dependent IXS spanning from the low-q, dipole limit to near-backscattering from the sample, the maximum allowed momentum transfer.

Below, we first provide background information on XRS in section II. This includes a brief theoretical treatment, and a more extended discussion of the relationship between XRS and more traditional measurements core-shell spectroscopies such as x-ray absorption fine structure (XAFS) and electron energy loss spectroscopy (EELS). In section III we describe the design of our apparatus. In section IV we discuss the performance of the apparatus, including presentation of initial results. We then conclude.

II. Background

In an inelastic x-ray scattering (IXS) experiment, the energy and momentum transfer from the scattering photon to the system is given by

$$\hbar\omega \equiv \hbar\omega_1 - \hbar\omega_2 = E_1 - E_2$$
$$\vec{q} \equiv \vec{k_2} - \vec{k_1}$$

(1)

where the 1 and 2 indices refer to the incident and scattered photons, respectively. The non-resonant portion of the double-differential scattering cross section naturally separates into a Thompson scattering contribution and the dynamic structure factor:

$$\frac{d^2\sigma}{d\Omega d\omega} = \left(\frac{d\sigma}{d\omega}\right)_{Th} S\left(\vec{q},\omega\right)$$

$$= \mathrm{r}_0^{\,2}\left(\hat{\varepsilon}_2 \cdot \hat{\varepsilon}_1\right)^2 \frac{\omega_2}{\omega_1} \sum_f \left|\left\langle f \mid \sum_j e^{i\vec{\mathbf{q}}\cdot\vec{\mathbf{r}}_j} \mid 0\right\rangle\right|^2 \cdot \delta\left(E_f - E_0 - \hbar\omega\right)$$

(2)

Eq. 2 provides a basis for understanding non-resonant IXS, including scattering from phonons, plasmons, valence electrons (Compton scatting) and core-shell electrons (XRS). Henceforth, we focus on our discussion on XRS.

The dipole limit in XRS is defined by the condition $qa \square 1$ where a is the average spatial extent of the initial state of the photoelectron, i.e. the mean diameter of the core shell wavefunction. In this regime, the expansion of the e^{iqr} operator in Eq. 2 can be truncated at the $i\vec{q} \cdot \vec{r}$ term, thus allowing only dipole transitions ($\Delta l = \pm 1$). Consequently

$$S(\vec{q},\omega) \underset{qa \square 1}{\rightarrow} \sum_{f} q \left| \left\langle f \mid \hat{q} \cdot \vec{r} \mid 0 \right\rangle \right|^2 \delta(E_f - E_0 - \hbar\omega), \qquad (3)$$

which is clearly proportional to the absorption coefficient

$$\mu = \sum_{f} \frac{4\pi^2 e^2}{m^2 c \omega_1 n} \left| \left\langle f \mid \hat{\varepsilon} \cdot \vec{r} \mid 0 \right\rangle \right|^2 \delta(E_f - E_0 - \hbar\omega_1), \qquad (4)$$

but with $\hat{q}$ playing the role of the polarization direction $\hat{\varepsilon}$ in x-ray absorption fine structure (XAFS) or related x-ray absorption spectroscopies. In comparing XAFS and XRS, two issues must be addressed: the different applications in the low-q limit, and the additional experimental degree of freedom provided in XRS by the momentum transfer.

First, as mentioned above, in the small-q limit XRS and XAFS probe the same transition matrix element and have similar directional-sensitivities. Recall, however, that we are specifically concerned about transitions starting from shells with relatively low binding energies, typically 50-600 eV; this includes the K-edges of first-row elements, L-edges of second-row and some third-row elements, etc. Consequently, the requirement for XAFS that the incident photon energy be comparable to the binding energy of the

relevant electronic shell can be very restrictive. The low-energy incident x-rays result in a measurement which can be predominantly surface sensitive and which requires a vacuum environment or other accommodations. In addition, low-energy x-rays are incompatible with the apparatus needed to create some extreme sample environments, such as high pressure chambers for liquids or solids: the x-rays cannot penetrate the walls of the chamber, so that direct XAFS of first-row elements, for example, cannot be performed inside diamond anvil cells. XRS measurements, on the other hand, can use hard x-rays (typically 5-10 keV) because it is the *energy loss*, not the incident or final photon energy which appears in the dynamic structure factor. This results in a measurement which is inherently bulk-sensitive, and is compatible with a wide range of sample environmental chambers.

Hence, even in the dipole limit, where both techniques provide analogous information, XRS and soft x-ray XAFS have significant differences in applicability because of the differences in incident radiation which is used. Three recent studies deserve note for both their scientific results and for their demonstrative value for the breadth of applicability of XRS to experiments which are problematic or impossible with direct, soft x-ray XAFS measurements. First, based on MD simulations, XANES calculations, and dipole-limit measurements of XRS a new local structure for liquid water has been proposed [44]. Second, a high-pressure XRS study of graphite revealed a new, ultrahard form of carbon [45]. Third, a high-pressure XRS study of hexagonal boron-nitride provided a clean signature of the transition to the hexagonal close-packed polymorph, which could previously be best studied only in pressure-quenched samples.

[**46**]   In each of these experiments the large penetration length of the incident hard x-rays was put to good use.

Second, while XRS measurements in the dipole (low *q*) limit are clearly valuable, additional information about previously forbidden final states can be obtained by studying the XRS when *qa* becomes larger. In this case, the matrix element in Eq. 2 does not simplify to that of Eq. 3, and higher order selection rules--beginning with the quadrupole transitions $\Delta l = 0$ and $\Delta l = \pm 2$ --become relevant. In early examples, the use of *q*-dependent XRS has shown itself to be especially suitable for spectroscopy of the final state for core excitons or other pre-edge resonances. [4**8-50**] This information is inherently unavailable from direct measurement of XANES on low-Z elements and is difficult (but possible, with the right materials and enough effort [**51**]) to acquire from EELS measurements, which seldom use momentum transfers larger than a few inverse Angstroms.

Key topics in the continuing development of *q*-dependent XRS as a spectroscopy related to, but unique from, XAFS and EELS will be the theoretical treatment of *q*-dependence throughout the entire accessible range of energy in $S(q,\omega)$ and improved background subtraction of the valence and core contributions to Compton scattering. Along these lines, the recent work of Soininen, Rehr, and Ankudinov [**47**] shows great promise to extend *ab initio* theoretical treatment of *q*-dependent XRS throughout the entire spectra, from pre-edge resonances through to the extended fine structure. In that paper, excellent agreement is found between the predictions of a real-space, full-multiple scattering Green's function approach and measurements of the direction- and *q*-dependent XRS from pure Be. [**56**] As we show below, progress on phenomenological

subtraction of the Compton scattering may be made with the Bayes-Turchin approach which has recently made significant inroads in XAFS analysis. [**58-61**] It is, however, important to note that this approach would be well superceded by a full *ab initio* calculation of the Compton background to avoid any possible complications from the weak but measurable fine structure which can occur in Compton scattering, especially when outside of the impulse approximation as is the case in most XRS measurements. [**refs**]

In summary, XRS provides an alternative to and extension of existing core shell spectroscopies such as XAFS and EELS. In the limit of small momentum transfer, all such techniques probe the same transition matrix element and can be treated with essentially the same theoretical framework. At higher momentum transfers, XRS becomes sensitive to and may be dominated by non-dipole transitions, thus giving new information about the local density of excited states.

III. The multielement XRS spectrometer

In Fig. 1 we show a perspective line-drawing of the apparatus design. As shown in the figure, the major components are the support frame, analyzer modules and corresponding detectors, detector shielding, helium-filled scattering enclosure, and sample enclosure and positioning assembly. We now describe these components in turn.

The support frame was machined from 2.5cm-thick Al jig plate. Large apertures cut in the support frame decrease the overall weight of the apparatus without significantly affecting the stiffness of the support. The vertical plate contains 19 equally-spaced locations where analyzer modules can be attached with dowel pins to assist with precise, reproducible positioning. The diffractive element of the analyzers (described below) is positioned 97.5 cm from the sample location. This plate also supports the scattering

enclosure and sample placement assembly. Given the horizontal polarization of the synchrotron radiation, the vertical scattering plane was chosen to maximize the polarization dependence of the Thompson prefactor.

In Fig. 2 we present an exploded assembly drawing of an analyzer module. The spherically-bent Si (111) diffractive elements have a 1-m radius of curvature and were manufactured by NJ-XRS Tech. The diffractive elements can be rocked through the Bragg angle (defining tilts normal to the vertical scattering plane) or normal to it ( ) using a kinematic, spring-loaded three-point tilt. By pairing a differential screw micrometer (OptoSigma xxxx) with a stepper motor (MicroMo 1524 containing a 41:1 spur gearhead), we obtained 6 microradian precision and better than 50 microradian unidirectional reproducibility, far finer than the width of the rocking curve of the analyzer crystals in the typical operating conditions. The analyzer crystals are prealigned using a small diode laser with a diverging optic at the sample position. Final tune-up references the strong elastic scattering from a polycarbonate sample at the Si <555> reflection at 9890 eV, precisely lining up each analyzer at the same Bragg angle (88.2 deg). The stepper motors are rapidly driven by a home-made assembly of 20 motor drivers controlled by TTL pulses from a computer board (Measurement Computing DIO96) working in the LabView environment. This allows rapid, simultaneous alignment of all 10 analyzer modules. After alignment, the motor drivers are turned off. No measurable drift in analyzer settings was found over many days of subsequent data collection. The 10 analyzers are placed at scattering angles corresponding to momentum transfers of q =.0.8 – 10.1 Å^{-1} respectively.

In Fig. 3 we show a perspective rendering of the detector assembly with the front cover removed for clarity. The detectors are NaI scintillation detectors with Be windows (Oxford Cyberstar). Strong spatial filtering against stray scattering is provided by 5 mm entrance apertures followed by 16 mm [ID, 48 mm OD] masks placed over the face of the detectors to decrease their exposed size to match the projection of the spherically-bent crystal through the entrance apertures. The vertical slats which separate the detectors reduce cross-talk between detectors due to air scattering within the detector module. A flux of 10^7 counts per second through one aperture induces less than one count per sec in the neighboring detector. The entrance apertures to the detector assembly are 105 cm from the face of the spherically-bent crystals of the analyzer modules, thus defining 10 Rowland circles that are perpendicular to the vertical scattering plane, with the sample and the detector entrance apertures off-circle by 2.5 cm. This has negligible effect on energy resolution because of the large depth of focus of the x-ray optics.

Given the distance between sample, analyzer, and detector, a He flight path is necessary. The scattering enclosure was constructed from Lucite and includes Kapton-covered apertures for the analyzer faces and for various places where incident, transmitted, or scattered radiation must enter or leave the enclosure. During operation, a small He flow and overpressure are maintained, and the absorption of the gas in the enclosure is monitored by observing any drifts in the transmission through the entire assembly.

Finally, in Fig. 4 we show a rendering of the sample enclosure. Three-axis positioning is provided by standard translation stages driven by motorized micrometers (Zaber T-LA28, Newport 426, 433 linear translation stages). Sample rotation about the

horizontal axis normal to the incident beam is also stepper-motor driven. Additional shielding against stray scattering is provided by a 12.5 cm diameter sample enclosure with a slot cut to allow scattering only near the vertical plane. This slot is sealed by a Kapton window and the sample enclosure is sealed to the positioning assembly by a flexible polyethylene diaphragm. The sample enclosure is then filled with He gas to decrease air scatter and to eliminate ozone formation, a dominant mechanism for beam damage for samples exposed to air. The relatively large volume of the sample enclosure allows for future modifications for furnaces, cryostats, electrochemical cells, pressure cells, and other extreme sample environments.

IV. Experimental

All measurements were performed at Sector 20-ID at the Advanced Photon Source x-ray synchrotron. This undulator beamline includes a Si (111) double crystal monochromator with energy resolution of 1.3 eV at 10 keV. The monochromatized radiation is focused by a toroidal mirror to a spot size of 0.3 mm (vertical) by 0.5 mm (horizontal). The incident and transmitted beams were monitored by identical He-filled ionization chambers (company name from Julie).

High sample throughput is an advantage of this technique, allowing for 40 samples—often with multiple edges—to be measured within one week during our last experimental run. Most of these samples were inorganic materials rich in low-Z elements, including a variety of boron glasses, hydrocarbons and their boron-nitrogen analogs, lithium hydrides? (get appropriate phrase from Linehan), lithium intercalated graphite, and new candidates for hydrogen storage [autrey ref]. XANES spectra typically

take 30 minutes to obtain 100:1 STN for a first-row monatomic (?) sample [double-check this on benzene or something]. Due to the relatively small size of the initial state core orbitals (0.1 – 0.2 Å, the q-dependence is often dipole-limited to anisotropies caused by the direction of q in a highly oriented sample or pre-edge pi* resonances. With adequate background subtraction, spectra lacking any **q**-dependence can be averaged over the 10 analyzers, vastly increasing the overall count rate in the dipole limit. The data can also be normalized by an f-sum rule to eliminate differences in the geometric sample thickness at different scattering angles [eisenberg/platzman original paper ref, schulke scaling ref].

We have also measured a variety of second and third row elements in materials containing Na, Mg, Al, Si, S, Cl, Ti, and V. Due to the higher absorption, these samples are substantially thinner, leading to a decrease in the overall signal from incoherent scattering [ref: J. Phys. Chem. Ref. **29** (4) 597-1048 (2000)]. However, the valence orbitals of higher-Z atoms typically have mean radii of 0.3 – 1 Å, enhancing both the signal and q-dependence of the L and M edges from these materials. For example, the count rate at boron K-edge for an analyzer at a momentum transfer with minimal Compton background is 2000 Hz (check this) for a 5 mm thick sample. In contrast, a similar measurement on a 0.25 mm Mg sample yields 250 counts-per-second at the L-edge and an average of 20 counts per second at the K-edge.

V. Results and Discussion

XRS data referenced the (555) Bragg reflection at 9890 eV for both the energy lost and the energy resolution. At this setting, the energy resolution is limited by the 111 monochrometer. There are two options for improving the overall energy resolution: insert PNC's 311 monochrometer with an intrinsic resolution of 0.5 eV at 10 keV or reference the (333) Bragg reflection. Both methods result in resolutions of 0.6-0.9 eV resolution, depending on the quality of the analyzer crystal, but are undesirable due to the substantial decrease in bandwidth and the increase of photoelectric cross-section with respect to the incoherent at the lower energy setting. Even for strongly scattering samples the background from stray scattering is 2 counts per second at each detector.

As an example of a quick (20 minute) XANES dataset, we present data taken at benzene's carbon K edge. The features, match Bergmann's previous work on solid benzene [2003 ref], but include moderate q-dependence in the height of the pi* pre-edge resonance (*…I'm tempted to claim that we are the first to document liquid benzene using XRS. I'm a little skeptical of this, but I've yet to find any references that measure the XRS off the liquid phase. I averaged the data for liquid benzene and it agrees well with Bergmann's data*)

VI. Conclusions

X-ray Raman scattering has been shown to be a bulk alternative to x-ray absorption spectroscopy for the core-shell excitations of low-Z material. New excitation channels resulting from high-q mulitpole transitions can sort out the symmetry components of the exicited LDOS, ultimately leading to information about the local

structural symmetry of a material. We have constructed a multielement apparatus that combines rapid sample-to-sample tuneup and simultaneous energy loss spectroscopy at different momentum transfers. This vastly improves the statistics and throughput of this new technique, while making it easier for the public to operate. This instrument will become available to general users following the present fiscal year and has been allocated 10% of operations at sector 20ID-B at the Advanced Photon Source.

Bibliography

[**44**] P. Wernet, D. Nordlund, U. Bergmann, M. Cavalleri, M. Odelius, H. Ogasawara, L.A. Naslund, T.K. Hirsch, L. Ojamae, P. Glatzel, L.G.M. Pettersson, A. Nilsson, "The structure of the first coordination shell in liquid water," Science **304**, 995-999 (2004).

[**45**] W.L.Mao, H.K. Mao, P.J. Eng, T.P. Trainor, M. Newville, C.C. Kao, D.L. Heinz, J.F. Shu, Y. Meng, R.J. Hemley, Science **302** (5644), 425-427 (2003).

[**46**] Y. Meng, H.K. Mao, P.J. Eng, T.P. Trainor, M. Newville, M.Y. Hu, C.C. Kao, J.F. Shu, D. Hausermann , and R.J. Hemley, "The formation of sp(3) bonding in compressed BN," Nature Mater. **3,** 111-114 (2004).

[**47**] J.A. Soininen, A.L. Ankudinov, J.J. Rehr, "Inelastic scattering from core-electrons: a multile-scattering approach," accepted Phys. Rev. B, 2005, arXiv:cond-mat/0503736v1.

[**48**] K. Hamalainen, S. Galambosi, J.A. Soininen, E.L. Shirley, J.P. Rueff, A. Shukla, "Momentum dependence of fluorine K-edge core exciton in LiF ," Phys Rev. B **65**, 155111 (2002).

[**49**] Y.J. Feng, G.T. Seidler, J.O. Cross, A.T. Macrander, J.J. Rehr, "Role of inversion symmetry and multipole effects in nonresonant x-ray Raman scattering from icosahedral B4C," Phys. Rev. B **69**, 125402 (2004).

[**50**] Y. Feng, J. A. Soininen, A. L. Ankudinov, J. O. Cross, G. T. Seidler, A. T. Macrander, J. J. Rehr, and E. L. Shirley, "Exciton spectroscopy of hexagonal BN using non-resonant x-ray Raman scattering," submitted Phys. Rev. B (2003).

[**51**] J.J. Ritsko, S.E. Schnatterly, P.C. Gibbons, Phys. Rev. B **10**, 5017 (1974); N. Jiang and J.C.H. Spence, Phys. Rev. B **69**, 115112 (2004), and references therein.

[**56**] C. Sternemann, M. Volmer, J.A. Soininen, H. Nagasawa, M. Paulus, H. Enkisch, G. Schmidt, M. Tolan, W. Schulke, Phys. Rev. B **68**, 035111 (2003).

[**58**] J.J. Rehr, J. Kozdon, J. Kas, H.J. Krappe, H.H. Rossner, "Bayes-Turchin approach to XAS analysis," J. Synch. Rad. **12**, 70-74 (2005); J. Kas, J.J. Rehr, unpublished.

[**59**] K.V. Klementev, "Extraction of the fine structure from x-ray absorption spectra," J. Phys. D-Appl. Phys. **34**, 209-217 (2001).

[**60**] H. Rossner, H. Krappe, "The influence of experimental and model uncertainties on EXAFS results," J. Synch. Rad. **8**, 261-263 (2001).

[**61**] H.J. Krappe, H.H. Rossner, "Bayes-Turchin approach to x-ray absorption fine structure data analysis," Phys. Rev. B **66**, 184303 (2002).

Figure Captions

FIG 1: SolidWorks rendering of qIXS spectrometer from a diametric perspective and a sectioned beam-on view: each pair of cones connecting the sample, spherically bent crystal (SBC) analyzer, and detector represents the path of a solid angle of x-rays. Currently we simultaneously measure ten energy loss spectra for q = 0.7 – 10.1 Å^{-1} and space for nineteen. The apparatus rests on an optical table, whose weight requirements led to large holes throughout the spectrometer's frame
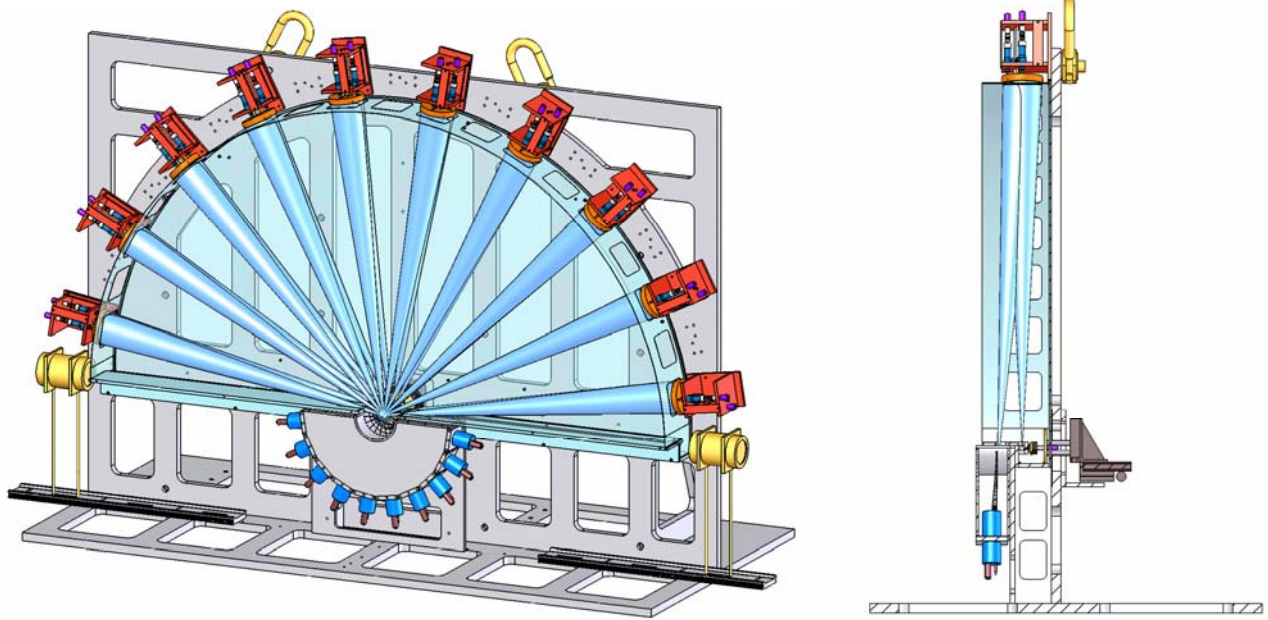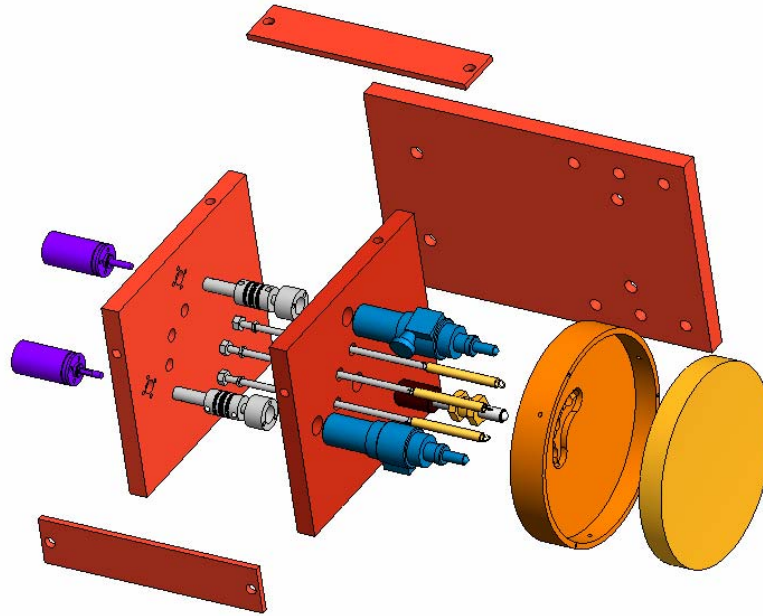
FIG 2: Analyzer module: (from right) the analyzer crystal is kinematically tilted in the 2θ and χ directions by a pair of differential screw micrometers (OptoSigma xxxx) that are driven by stepper motors (MicroMo 1524 15/8). The other degrees of freedom are controlled by a center pivot screw and the fixed position one the spectrometer frame (fig 1).
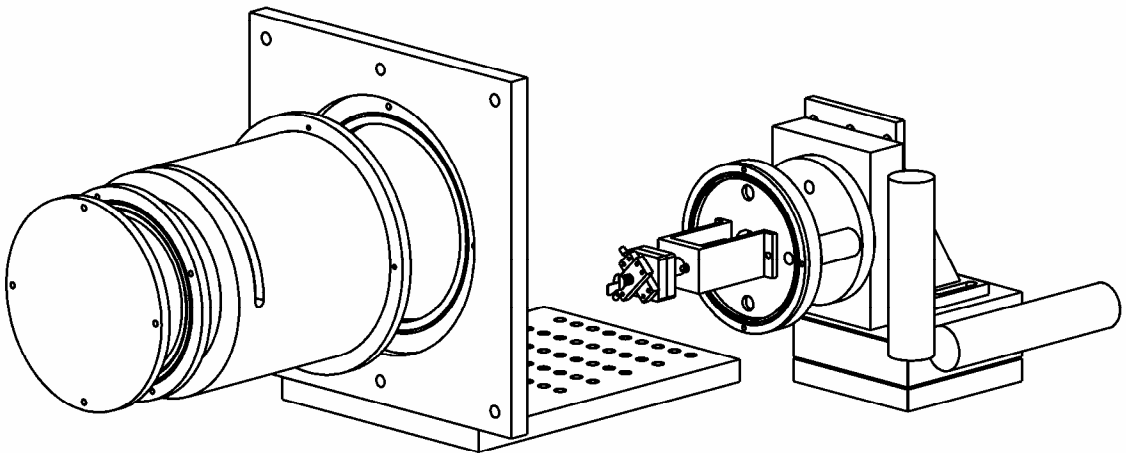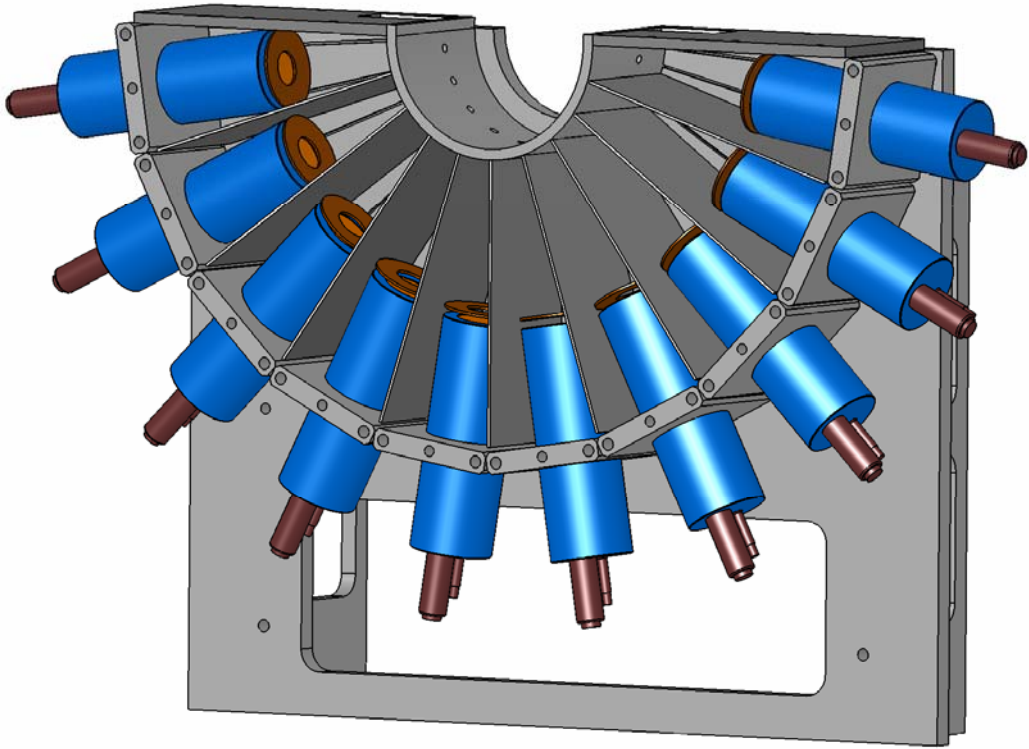
FIG 3: (above) Pinholes leading to the detectors spatially filter the x-rays coming from each analyzer. The slats and detector masks also reduce the number of stray scattering to 1-2 counts per second. (below) The sample is contained within helium-flowing loadlock chamber. This provides additional baffling while protecting the sample from ozone damage caused by incident x-rays. The sample has 4 motorized axes: three translational and one rotational axis perpendicular to the vertical scattering plane. Future versions of this unit will include both a cryostat and a heating element.

ION-SOFT LANDING AND EX SITU SURFACE ANALYSIS BY ATOMIC FORCE MICROSCOPY

Jason R. Green and R. Graham Cooks
Purdue University

and

Omar Hadjar, Julia Laskin
and Jean Futrell
Pacific Northwest National Laboratory
Richland, WA

1.   Abstract

Atmospheric atomic force microscopy (AFM) was used to probe the interface of a mass spectrometrically prepared (i.e. by ion soft-landing) surface and extract details regarding the environment of deposited material. Construction of a home-built apparatus was completed for the soft-landing procedure. Atmospheric tapping mode AFM images of various surfaces, collected prior to landing, revealing that gold coated mica surfaces are atomically flat over several hundred nm regions and a topologically convenient substrate. Au/mica surfaces further afforded formation of a self-assembled monolayer (SAM), such that these surfaces could be systematically subjected to an ion beam for varying times. After a given deposition time, surfaces were exposed to ambient conditions and images progressively collected.

2.   Introduction

Ion-soft landing is a method of preparing modified surfaces by gently landing intact polyatomic ions from the gas-phase onto a monolayer surface at room temperature that has led to recent novel experiments in preparative mass spectrometry. During these experiments ions delivered in the form of a beam, incident on a self-assembled monolayer surface, are trapped in the fluorocarbon, hydrocarbon and other functionalized matrices. In some cases they may be trapped for many hours and then released in situ, intact, upon sputtering at low or high energy or by thermal desorption.[1]

The ability to directly deposit intact polyatomic ions into F-SAM/polycrystalline Si wafer surfaces at low collision energies is a striking result, although the deposition occurs into only a small fraction of the available surface sites. The alternative process, in which the intact molecular entity is deposited but with loss of its charge (by deprotonation or other mechanisms) is also of interest, as are the factors that allow charge retention. A combination of steric hindrance in the polyatomic ions and the inert and ordered matrix formed by the fluorinated alkylthiolate chains of the F-SAM surface is believed to be important for successful ion softlanding with charge retention. Electrostatic interactions between the soft-landed ions and induced electric dipoles in the surface substrate may also contribute significantly to their binding to the F-SAM surface. At least in the case of small organic ions, intact soft-landing of the ion is more successful with closed-shell rather than open-shell ions, a result ascribed to the ease of neutralization of the latter. Confirmation of molecular composition is achieved by isotopic labeling, high-resolution

mass measurements, more rarely, by x-ray photoelectron spectroscopy and here by tapping mode AFM.[2]

Atmospheric tapping mode AFM places no restrictions on the characteristics of the surface (i.e. insulator properties) in contrast to STM but most importantly, data obtained from AFM measurements has information inherently encoded, regarding the electric interaction of the surface and AFM tip (related to the charge retention of soft-landed ions). Finally, convenience, availability and prospect for manipulation of ionic species at the nanoscale further contributed to the decision to use AFM.

3.   Research Summary

It was previously proposed to explore the use of scanning probe microscopy (e.g. AFM and/or STM) to recognize the presence of free ions in interfacial layers and to study the interfacial interactions of ions on a surface. Independent confirmation is also sought, of a recent in situ FT-ICR and ex situ TOF secondary ion mass spectrometry (SIMS) analysis, where it was shown that many soft-landed peptides retain charge even when exposed to atmosphere for several hours.[3]

3.1 Experimental

3.1.1 Mass Spectrometry

The device used for ion deposition is shown in Figure (1). Briefly, it is comprised of an electrospray ion source, an electrodynamic ion funnel, heated capillary, two Extrel quadrupoles (one for collisional cooling, one for m/z selection), a bending quadrupole, a pair of Einzel lenses and a wire mesh for deceleration. The collisional and resolving quadrupoles were operated in RF

Figure 1: Soft-landing device.
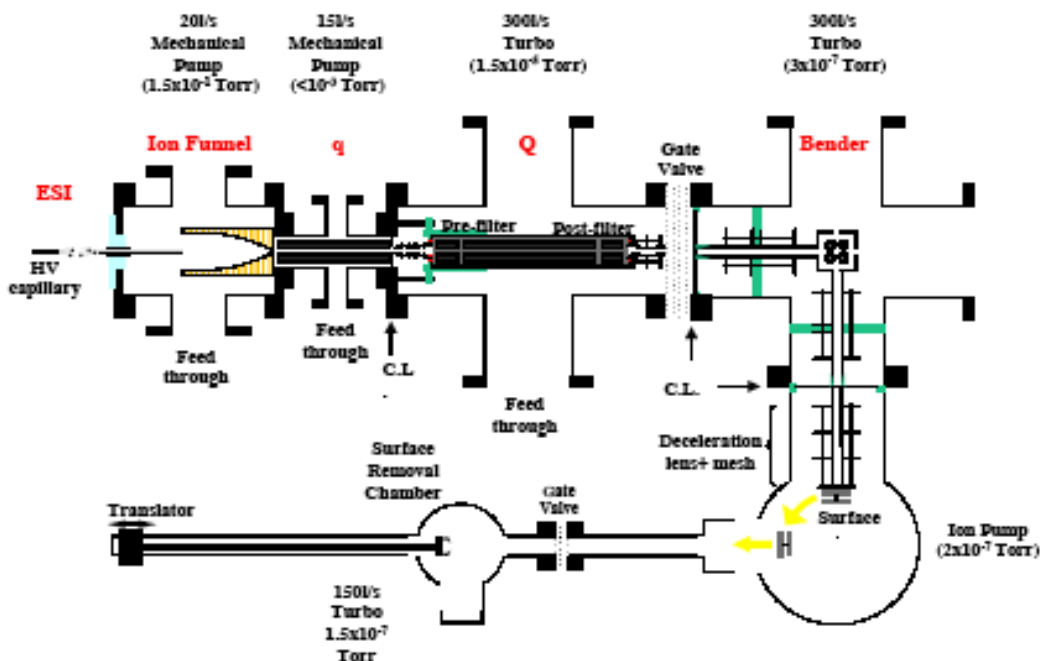
only mode in these cursory experiments so as to maximize the amount of material deposited – 50-100pA of ion current was common. Rough estimations suggest that after 30 minutes of landing $\approx 10^4$ ions strike a surface area of $1\mu m^2$, which translates into approximately $\approx 100 - 1000$ ions assuming a $1 - 10\%$ survival efficiency. The surface dimensions were 5mm x 5mm while TOF-SIMS indicated a beam size of roughly $4 - 5mm^2$ (≈ 1 count/$3\mu m$ x $3\mu m$). A 16eV laboratory frame collision energy (the surface was typically grounded) and substance P (m/z 1347) were used throughout.

3.1.2 AFM

A Digital Instruments(TM) Nanoscope IIIa MultiMode scanning probe microscope in tapping mode was used for image acquisition. Equipped with an E scanner, the scan size was 10μm x 10μm with a vertical range of 2.5μm. The tip offset was 0nm in x, y and rastered at 1Hz in the "fast axis." Cantilevers were tuned to oscillate near (within 1-5%) the resonant frequency $\approx 350kHz$ and oriented on the surface with a Nikon 10x objective and CCD. Feedback controls were variable but typically the integral gain was ≈ 0.2 with a proportional gain of $0.3 - 0.5$. Au/Cr/Si wafers were UV cleaned, rinsed with ethanol before and rinsed/sonicated in ethanol after ≈ 12 hours in dodecanethiol. For Au/mica, SAMs were formed after ≈ 12 hours in thiol and used following an ethanol rinse. Sonication, UV cleaning or improper handling resulted in delamination of the Au from the mica and destruction of the surface order. The basic experimental protocol was to collect images of the surface prior to SAM formation, soft-landing and rinsing. This was done for varying deposition times and successively, over many hours, while exposed to ambient conditions.

3.2 Results

Soft-landing of ions is typically into a self-assembled monolayer built on a Au/Cr/Si polycrystalline wafer. Cursory AFMon this surface (prior to SAMformation or landing) quickly revealed topographical interference of the interfacial features with those anticipated for deposited material, Figure (2). In this image there is some evidence that a dull tip was used, in the repeated image stamped out. Thus, the xy-dimensions of the surface structures are uncertain, though there is little doubt as to the z-axis measurement. Other obstacles were faced in the course of this research, which degraded image quality/reliability, namely, tip contamination (a problem associated with loosely bound material - see below) and multiple tips (a manufacturing defect).
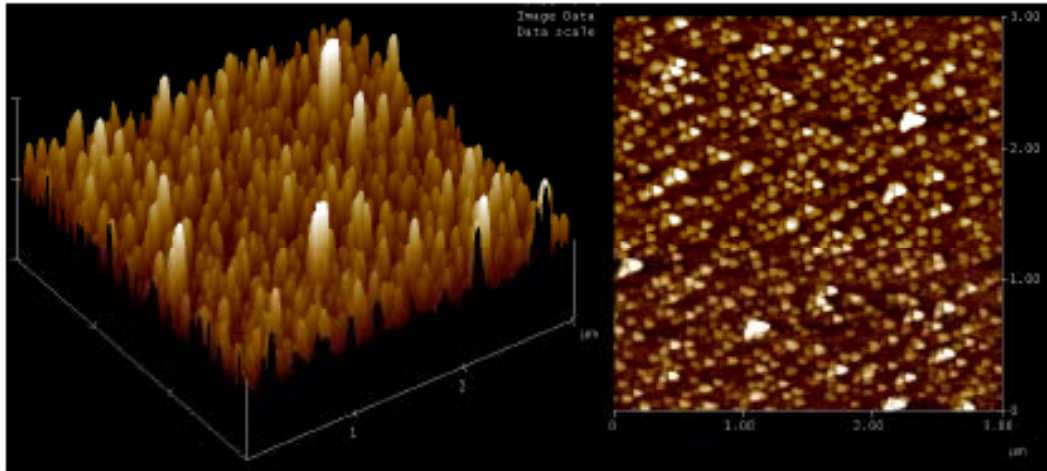
Figure 2: TappingMode image of Au/Cr/Si polycrystalline wafer typically used for soft-landing experiments on a 50nm z -scale. Average "peak" height was estimated to be ≈ 30nm.
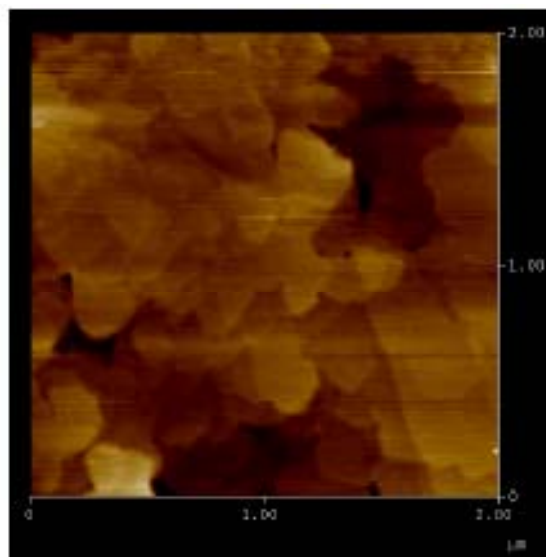

Figure 3: TappingMode image of an HSAM/Au/mica surface collected prior to soft-landing. z -scale is 5nm.

To lessen the experimental difficulty associated with imaging soft-landed material, atomically flat substrates were sought. Au/mica was found to be readily available. Figure (3) was acquired after formation of a HSAM and before landing. From this figure it is apparent that the SAM material is not directly observable due to the limited resolution of this technique, in atmosphere, and the properties of the surface being probed; however, the presence of material is indirectly evident. With the HSAM/Au/mica surfaces imaging was difficult at times, presumably due to our inability to effectively remove excess layers that the AFM tip could then pick-up, drag, etc. Nevertheless, "terraces" can be clearly seen - atomically flat regions, hundreds of

nanometers wide. This distinctive form of the interfacial landscape are a good indicator of a clean surface that does not interfere with the features of the landed material. Following 5 and 10 minutes (net) exposure of a clean HSAM surface to an ion beam of the multiple charge states, fragments, etc. of substance P and extraction from the vacuum chamber, images such as Figure (4) were obtained. A quick comparison reveals a definite increase in landed material. Images were similarly obtained for 15, 30 and 85 minutes (Figure (5)) of soft-landing. It can be seen that a deposition time in excess of an hour (in fact, 20-30 minutes is all that is required) completely conceals the underlying surface structure. Some of these surfaces were monitored as a function of exposure to ambient conditions but are excluded here for brevity. Finally, despite the fragility of the Au/mica surfaces, it was found that they could survive at least one cycle of SAM preparation, landing, rinsing with interspersed AFM imaging. Figure (6) is a representative image of the surface after the rinsing step. Clearly the landed material has been effectively removed and the HSAM/Au/mica features revealed.
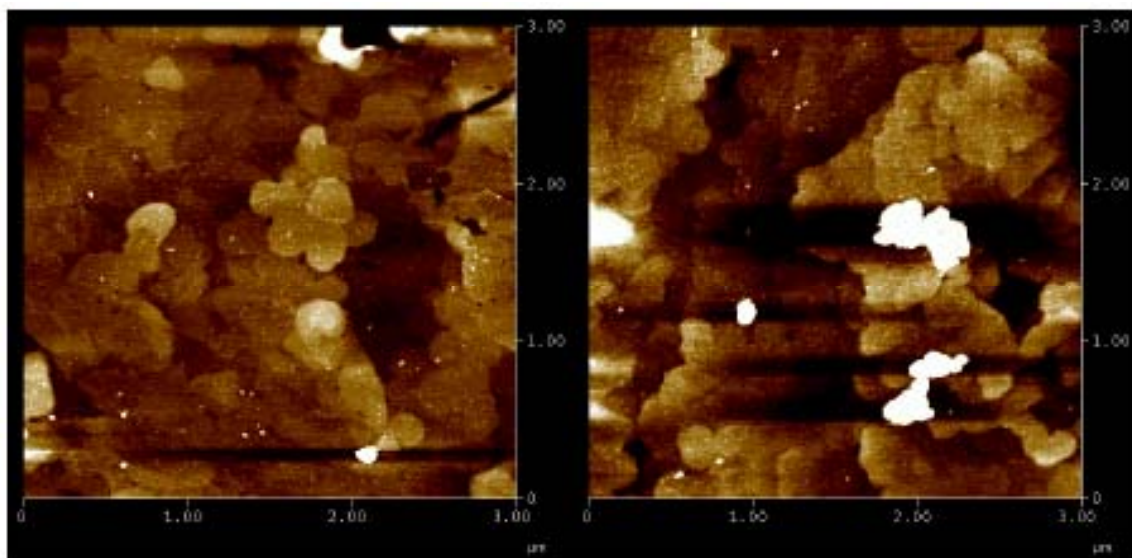

Figure 4: TappingMode image collected after 5 (left) and 10 (right) minutes of soft-landing on a 5nm z -scale.

4.   Conclusions

As mentioned, data obtained from AFM measurements has information inherently encoded, regarding the electric interaction of the surface and AFM tip which is directly related to the charge retention of soft-landed ions. An open question is whether this electrostatic information can be deconvolved from topographical data, either by making another measurement (electrostatic force microscopy, EFM) or by image processing and analysis. The latter option is currently being pursued with the data described below and a freeware program, Image J. If this can be accomplished then one should be able to follow changes in charge state of ions at the surface, including the sequential neutralization of such ions as doubly-charged peptides. Understanding gleaned, of the local chemical environment of landed ions, may further allow exploration of the possibility of manipulating ions for subsequent reaction or construction of nanoscale device

References

[1] R.G. Cooks, S.-C. Jo, J.R. Green "Collisions of Organic Ions with Surfaces" Appl. Surf. Sci. **2004**, 231-232, 13-21.

[2] B. Gologan, J.R. Green, J. Alvarez, J. Laskin, R.G. Cooks, "Ion/Surface Reactions and Ion Soft-Landing" Phys. Chem. Chem. Phys. **2005**, 7 (7), 1329 and 1490-1500.

[3] J. Alvarez, R.G. Cooks, S.E. Barlow, D.J. Gaspar, J.H. Futrell and J. Laskin. "Preparation and in situ Characterization of Surfaces Using Soft-Landing in a Fourier Transform Ion Cyclotron Resonance Mass Spectrometer" Anal. Chem. **2005**, 77, 3452-3460.

Ligand effects in transition metal coordination compounds: Rendering a molecular picture to electrochemical results"

Christos E. Kefalidis and Constantinos
A. Tsipis
*Aristotle University of Thessaloniki
Department of Chemistry
Laboratory of Applied Quantum
Chemistry
Greece

and

Sotiris S. Xantheas
Pacific Northwest National Laboratory
Richland, WA

Introduction

The ligand bonding effects described by the σ-donor and π-acceptor capacities of the ligands in relation to the π-donor and σ-acceptor capacities of the molecular fragments containing the central metal atoms or ions are the key to the understanding of the structural, energetic, electronic and catalytic properties of transition metal coordination compounds. Therefore, all attempts to quantify these effects either by experimental or theoretical parameters are of a great potential interest, for it could assist in the design of coordination compounds with novel properties and technological applications.

The goal of this project is to investigate the correlation between oxidation potentials and molecular properties (like the adiabatic ionization energies or the metal-ligand vibrational frequencies) for a series of closed shell octahedral $[Cr^{(0)}(CO)_5L]$ and $[Ru^{(II)}(NH_3)_5L]$ complexes in the gas as well as in the condensed phase.

Basic Concepts

The P_L constant, introduced by Pickett and co-workers, is a parameter of ligand constants which is defined (for the Cr coordination complexes as an example) according to:

$$P_L = E_{1/2}^{ox}[Cr(CO)_5 L] - E_{1/2}^{ox}[Cr(CO)_6]$$

This scale is used to analyze the $E_{1/2}^{ox}$ of various closed-shell octahedral complexes according to:

$$E_{1/2}^{ox}[M_s L] = E_s + \beta \cdot P_L$$

where E_s is a measure of the electron-richness of the metal and β a measure of its polarisability.

Computational Details

All calculations were carried out using the **NWChem** suite of programs. The geometry optimizations and vibrational analysis were performed at the DFT level of theory using the B3LYP functional. For the Cromium compounds we used the 6-311+G(df) basis set for the Cr atom and the 6-311+G(d) for all other atoms. For the Ruthenium complexes we used the "Stuttgart RSC 1997 ECP" Effective Core Potential for Ru and the 6-31G(d,p) basis set for all other atoms.

Results

Starting from the standard complex $Cr(CO)_6$, we replace one carbonyl ligand with various ligands as N^+, NO^+, Cl^-, OH^-, N_2, etc. We followed the

same approach for the ruthenium complexes, $Ru(NH_3)_6$. The results for the Chromium complexes are summarized in Table 1 below:

Complex	E_{homo} (Kcal/mol)	$R(Cr-CO_{trans})$ Å	$R(C-O_{trans})$ Å	ω (CO) (cm^{-1})
$[Cr(CO)_5(N)]^+$	-0.452874	2.594	1.129	2274.8
$[Cr(CO)_5(NO)]^+$	-0.446241	2.068	1.132	2218.0
$Cr(CO)_6$	-0.266215	1.928	1.150	2065.1
$[Cr(CO)_5(N_2)]$	-0.257121	1.899	1.153	2053.0
$[Cr(CO)_5(CNMe)]$	-0.235440	1.905	1.155	2043.0
$[Cr(CO)_5(NCMe)]$	-0.225794	1.879	1.158	2020.0
$[Cr(CO)_5(NH_3)]$	-0.229952	1.870	1.159	2013.8
$[Cr(CO)_5(NCS)]^-$	-0.083738	1.855	1.169	1949.0
$[Cr(CO)_5(CN)]^-$	-0.083622	1.860	1.162	1952.8
$[Cr(CO)_5(Br)]^-$	-0.083510	1.839	1.172	1934.8
$[Cr(CO)_5(Cl)]^-$	-0.084282	1.841	1.173	1933.0
$[Cr(CO)_5(H)]^-$	-0.072348	1.865	1.172	1929.3
$[Cr(CO)_5(OH)]^-$	-0.044268	1.838	1.178	1903.1

Table 1: Results of electronic structure calculations for the Chromium complexes

When the ligand is a good π-acceptor, then there exists a competition for the electron density of the metal between that ligand and the CO that is trans to ligand (see figure below). This competition has an effect in the bond distance R(Cr-L), making this bond shorter and consequently the bond distance $R(Cr-CO_{trans})$ longer and consequently the R(C-O) shorter. This last effect results in a larger vibrational frequency for the CO ligand in the complex. This effect has been clearly indicated from the results of the Table.

pi acceptor ligand

Competition for electron density
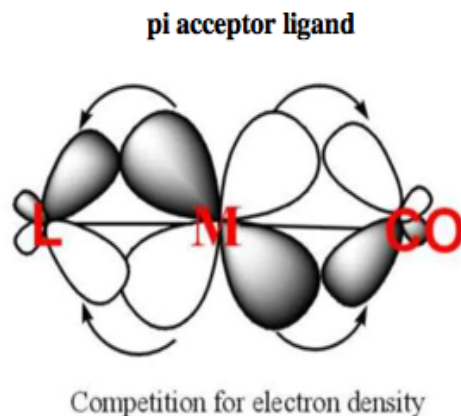
We can furthermore correlate the P_L constants with the vibrational frequencies of $(CO)_{trans}$ for the 13 ligands studied here. This correlation is clearly linear as indicated from the results of Table 2 and Figure 2.

Complex	P_L (V)	$\omega(CO)$ (cm^{-1})
$[Cr(CO)_5(N)]^+$	1.46	2274.8
$[Cr(CO)_5(NO)]^+$	1.40	2218.0
$Cr(CO)_6$	0.00	2065.1
$[Cr(CO)_5(N_2)]$	-0.07	2053.0
$[Cr(CO)_5(CNMe)]$	-0.43	2043.0
$[Cr(CO)_5(NCMe)]$	-0.58	2020.0
$[Cr(CO)_5(NH_3)]$	-0.77	2013.8
$[Cr(CO)_5(NCS)]^-$	-0.88	1949.0
$[Cr(CO)_5(CN)]^-$	-1.00	1952.8
$[Cr(CO)_5(Br)]^-$	-1.17	1934.8
$[Cr(CO)_5(Cl)]^-$	-1.19	1933.0
$[Cr(CO)_5(H)]^-$	-1.22	1929.3
$[Cr(CO)_5(OH)]^-$	-1.55	1903.1

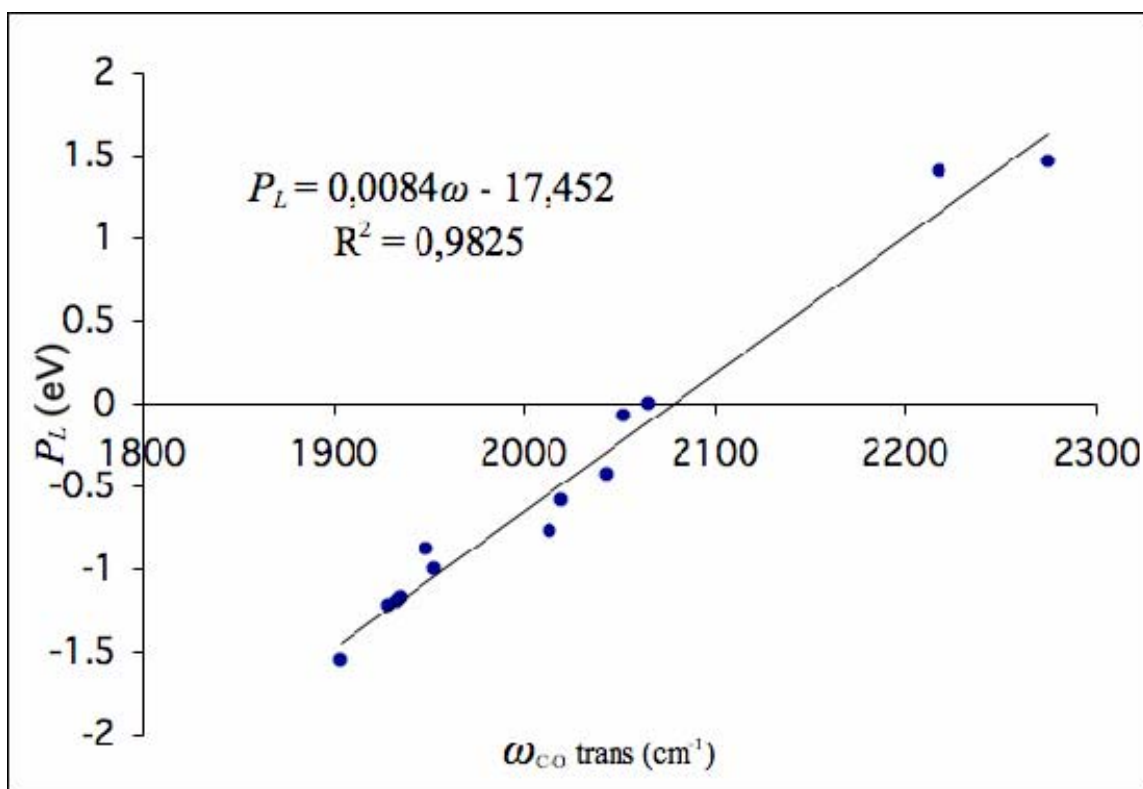Table 2: Correlation between P_L and $\omega(CO)$ for the Chromium complexes

Figure 2: Correlation between P_L and $\omega(CO)$ for the Chromium complexes

The next step was to correlate the P_L constants with the adiabatic ionization energies for the chromium complexes. This correlation is listed in Table 3 and schematically shown in Figure 3.

Complex	P_L (V)	$I.E^a$ (Kcal/mol)
$[Cr(CO)_5(N)]^+$	1.46	5.237895
$[Cr(CO)_5(NO)]^+$	1.40	4.818078
$Cr(CO)_6$	0.00	0.000000
$[Cr(CO)_5(N_2)]$	-0.07	-0.233828
$[Cr(CO)_5(CN)]^-$	-1.00	-4.567815
$[Cr(CO)_5(OH)]^-$	-1.55	-5.605467

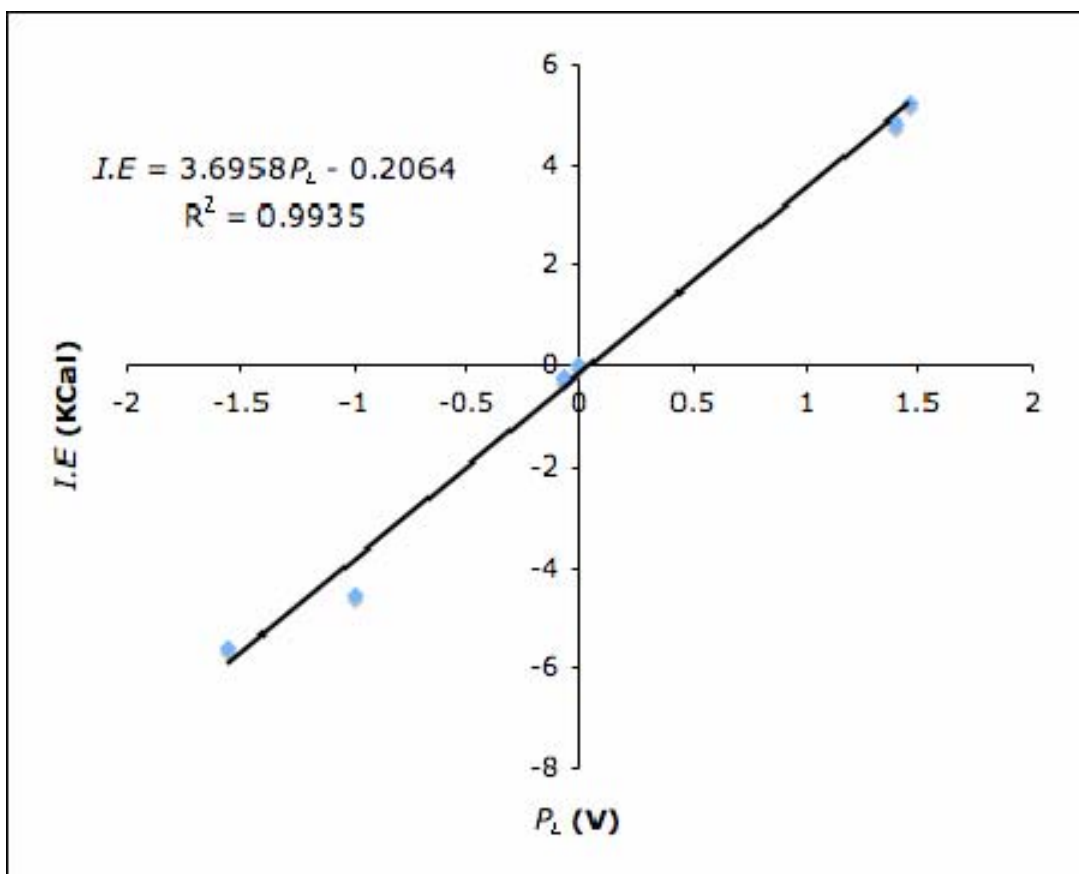Table 3: Correlation between P_L and Ionization energies

Figure 3: Correlation between Ionization Energy and P_L constants

The above graph shows an almost perfect correlation (R^2=0.9935) between the ionization energies and P_L.

Calculations for the ruthenium complexes are underway. Some preliminary results are shown in Table 4 below:

Complex	E_{homo} (Kcal/mol)	D_e (Kcal/mol)	D_0 (Kcal/mol)	d(Ru-NH$_3$)$_{trans}$	v(RuN)$_{trans}$ (cm^{-1})
[Ru(NH$_3$)$_5$(H)]$^+$	-130.3	-681.7	-699.0	2.422	340.8
[Ru(NH$_3$)$_5$(Cl)]$^+$	-124.7	-675.9	-659.8	2.208	361.7
[Ru(NH$_3$)$_6$]$^{2+}$	-149.0	-491.9	-473.2	2.199	383.4
[Ru(NH$_3$)$_5$(SiH$_3$)]$^+$	-138.2	-681.7	-699.0	2.422	225.6
[Ru(NH$_3$)$_5$(CNPh)]$^{2+}$	-154.9	-523.3	-540.9	2.268	327.1
[Ru(NH$_3$)$_5$(SCN)]$^+$	-130.5	-649.4	-666.4	2.222	343.2
[Ru(NH$_3$)$_5$(PH$_3$)]$^{2+}$	-142.0	-488.5	-506.8	2.248	328.1
[Ru(NH$_3$)$_5$(OH)]$^+$	-131.6	-737.7	-755.7	2.000	341.2
[Ru(NH$_3$)$_5$(NCPh)]$^{2+}$	-188.2	-508.9	-526.1	2.200	366.9
[Ru(NH$_3$)$_5$(N$_2$)]$^{2+}$	-130.2	-477.0	-495.0	2.186	377.7
[Ru(NH$_3$)$_5$(CNMe)]$^{2+}$	-154.8	-519.4	-501.5	2.266	327.1
[Ru(NH$_3$)$_5$(CO)]$^{2+}$	-130.5	-500.9	-482.1	2.260	330.9
[Ru(NH$_3$)$_5$(CN)]$^+$	-128.6	-694.9	-677.9	2.303	305.2

Table 4: Selected structural, spectroscopic parameters, energy of HOMO and zero-point energies for the complexes of ruthenium

Future Studies

A future goal of our study will be the generation of a database of DFT-calculated descriptors either for donor or acceptor ligands in a range of representative complexes. The prototype ligand knowledge base (LKB), resulting from various statistical analysis methods should be used for the study of specific properties, as well as for the prediction of properties concerning novel or untested ligands.

References

J. Chatt, C. T. Kan, G. J. Leigh, C. J. Pickett and D. R. Stanley, *J. C. S Dalton*, **1980**, 2032.

J. Chatt, H. Neukomm, G. J. Leigh, C. J. Pickett and D. R. Stanley, *J. C. S Dalton*, **1980**, 121.

M. K. Lloyd, J. A. McCleverty, D. G. Orchard, J. A. Connor, M. B. Hall, I. H. Hall, I. H. Hillier, E. M. Jones and G. K. McEwen, *J. C. S Dalton*, **1973**, 1743.

C.J. Pickett and D. Pletcher, *Journal of Organometallic Chemistry,* 102, **1975**, 327

C. A. Tsipis, *Coord. Chem. Rev.* **1991**, *108*, 163.

X-Ray Photoelectron Spectroscopy and Transmission Electron Microscopy Studies on nanocrystalline Cerium Oxide Particles

Satyanarayana Kuchibhatla and S. Seal
Central Florida University
Orlando, FL

and

Don Baer
Pacific Northwest National Laboratory
Richland, WA

Cerium oxide (Ceria) is one of the widely studied rareearth oxide. Cerium oxide in nano scale domain has gained attention in a variety of applications like electrocatalytic reactors, water-gas shift catalysts, fuel additives, solid electrolytes, and exhaust control, UV-absorber etc. The key feature that made ceria most popular is the presence of mix valence states. In spite of a number of studies by researchers the exact reasons and the conditions under which the ceria exhibits the mixed valence states; or complete 3+ oxidation state are issues of debate. Various experimental and theoretical studies have been reported in the literature. However, one major draw back in the existing literature is the lack of simultaneous particle size and oxidation state analysis on a same set of particles. During the course of this work an effort has been made to characterize the ceria particles on Carbon/ Farmvar coated Cu grids using Transmission Electron Microscope (TEM) and X-ray photo electron Spectroscope (XPS). This study has revealed some facts about the cerium oxidation state dependence on the substrate, synthesis media, amount of loading on the substrate etc.

Ceria nanoparticles were synthesized using a room temperature wet chemical method in DI water and 20% Poly(ethylene)glycol systems. Microemulsion based synthesis in Toluene and AOT has been used to synthesize third category of ceria particles. All these particles were synthesized using Ce (III) Nitrate hexahydrate precursor and suitable

oxidizing agent. Particles were analyzed by vertically dipping the TEM grids in the sols containing the ceria particles. These TEM grids were dried over night at room temperature in a vacuum desiccator before analysis. TEM and XPS studies both were carried on the TEM grids, although the quantity of Ce signal is not very high, results were consistent in a number of cycles. Predominant 3+ oxidation state has been found in almost all the samples including both fresh and aged sols. Effect of number of particles loaded on the grid and the synthesis media have been studied as two separate parameters. Existing literature gives a great importance to the role of X-ray damage to the reported 3+ oxidation state in ceria. Current set of experiments did not support this particular aspect completely. The X-ray exposure did not reveal any significant reduction in the oxidation state in ceria nano particles. Although it is too early to make any statement about the results, when analyzed the simultaneous TEM, XPS data are encouraging and demand various experiments of similar nature. Following are some of the TEM images taken on JEOL HRTEM at EMSL.
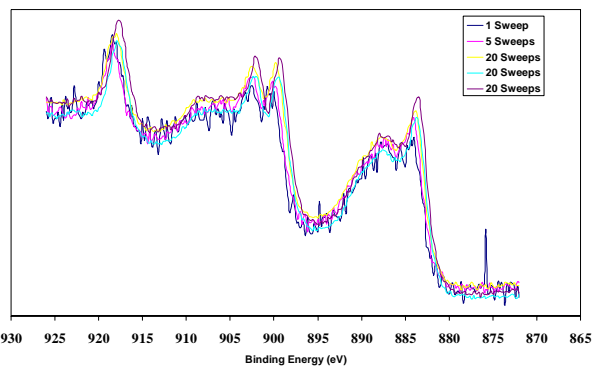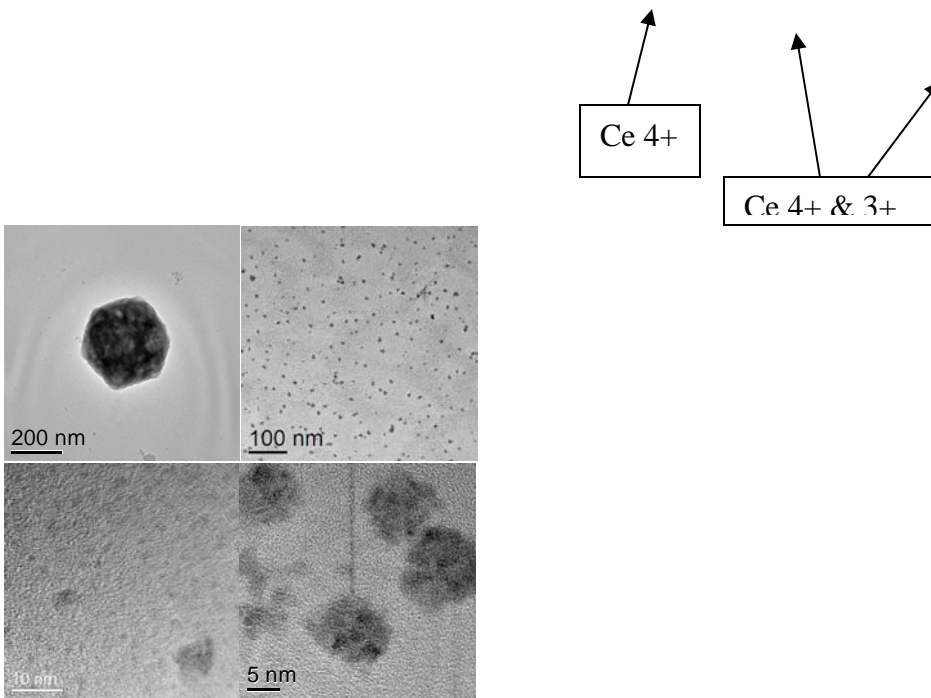
Fig 1) High Resolution TEM images of Ceria nano particles synthesized in various solvents and a typical XPS Spectra showing both the 3+ and 4+ Oxidation states in Ceria

FPGA- based Image Capture System – A SmartCam Initiative

Anoop M. Mayampurath and
Scott Budge
Utah State University
Logan, UT

and

Derek F. Hopkins, Kenneth A. Perrine, Brian L. LaMarche, Marianne B. Sowa and James Solinsky
Pacific Northwest National Laboratory
Richland, WA

Introduction

Ongoing research at Pacific Northwest National Laboratory (PNNL) aims at elucidating the complexities behind intercellular communication. Standard two-dimensional viewing of cell samples places constraints on the study of cell signaling, since, for this particular area, observations must be made in the same domain as the cell themselves, i.e. in three-dimensions. The confocal microscope aids in this aspect, due to the Z-plane attachment to the standard domain of observations. This allows 3-dimensional reconstruction of cellular structures, which in turn, allows observation of signaling in spatially localized areas of cells [1, 2].

PNNL houses a confocal microscope which has been designed to capture 1280x1024 dimension images at the rate of 15 frames per sec or 640x480 images at 30 frames per second. Figure 1 depicts a photograph of the microscope.
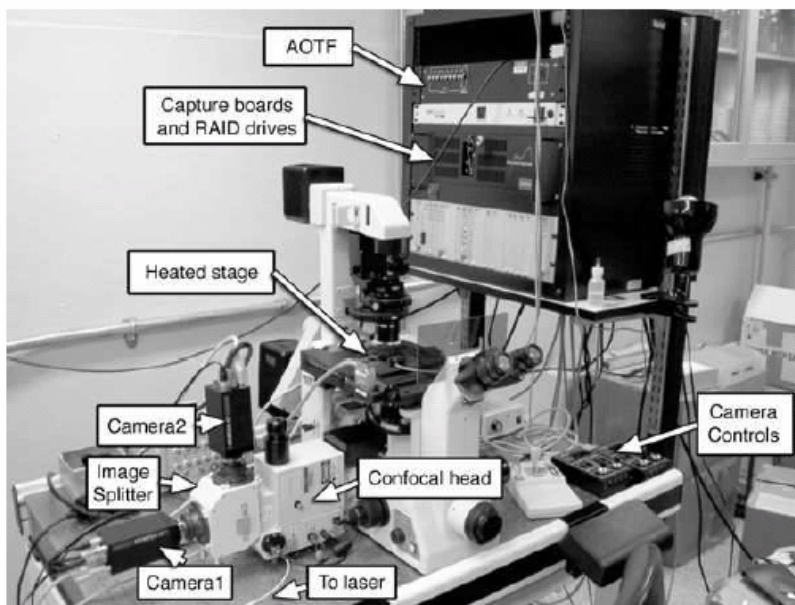
Fig 1: The confocal microscope

The confocal scanning head is connected to two Uniq-1800 CCD cameras, which are attached to an image splitter that resolves the two wavelengths of excitation using a dichroic. The wavelengths of excitation are – 487 nm (green) and 647 nm (red). The Z-axis is adjusted using a PT piezo focus drive. Varying the Z-Axis will result in a stack of images corresponding to each depth of observation. Techniques such as FRET

(Fluorescence Resonance Energy Transfer) and blob analysis can then be applied to the images to study cell signaling [1, 2]

Over a period of time, a team of biologists and computer scientists have been working in tandem to develop an in-house system that controls the operation of the microscope, and do processing such as FRET, on the images acquired. The idea behind this initiative was to gain more control over the system than a third-party vendor could possible provide. This offers many flexible options for the biologists in terms of application specific requirements, changes and updates. A good depiction of the system is shown in Figure 2.
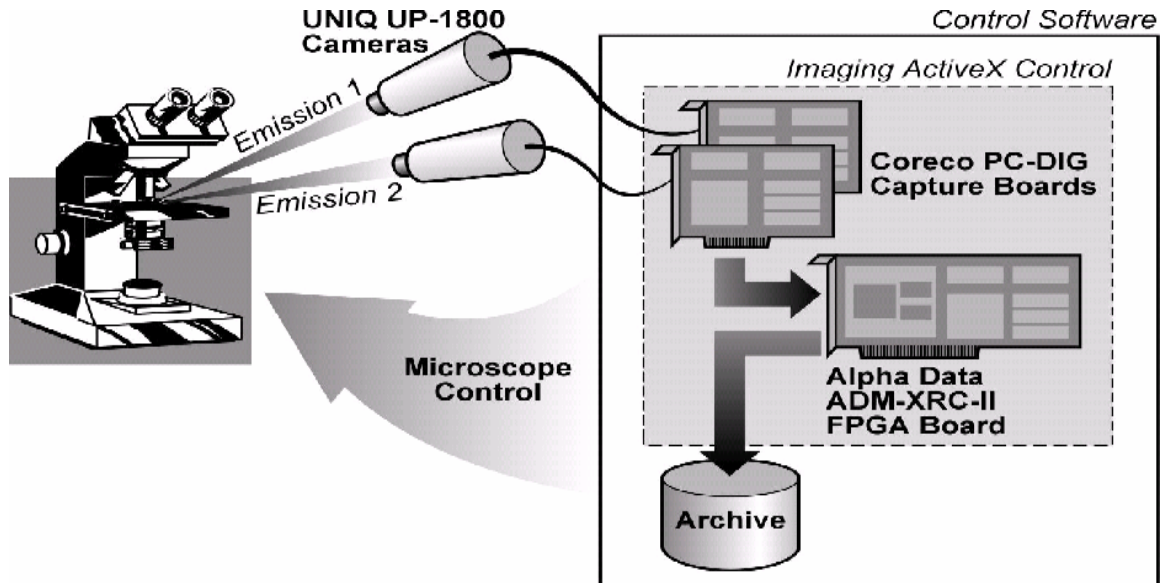

Fig 2: Existing Configuration

The Uniq-1800 cameras have capabilities of operating in double speed (2x2 binning), gives a 10-bit RS-644/LVDS digital output per pixel, and can operate in free-running and asynchronous modes [3]. The images from the cameras are captured using Coreco PC-DIG capture boards. These are basically PCI-bus plug-n-play framegrabbers having a 4 MB temporary buffer storage capacity [4].

The interface to the microscope, written in Microsoft Visual Basic, allowed the biologists to control laser wavelength, stage position, capture settings and also write their own scripts for automated control using a SAX-engine. For handling images, an ActiveX subsystem was designed.

For the design of image processing procedures such as accurate co-registration of the multiband images, blob analysis and FRET, a stand-alone system using an FPGA (Field Programmable Gate Array) was chosen. The computational complexities of a general purpose computer and the expensive nature of application-specific hardware make them both illogical choices as means of realization of real-time image analysis systems. High-level languages such as Handel-C can be used without extensive hardware knowledge. Availability of ANSI C like constructs, inherent parallelism, user-defined widths and

channels for communicating between two parallels block of code are some of the features that make Handel C a good tool to program the FPGA.

In moving forward with the objective of acquiring control over the system, it necessitated the replacement of the capture boards with the FPGA themselves. This has several advantages besides gaining flexibility with respect to image capture. One, the maximum frame rate that was acquired from the capture board was 7 frames/sec. By using the FPGA as a pseudo-capture board, the intention was to achieve full frame rate. Second, replacing the capture board would result in freeing of considerable PCI bus space, which could be used by for other purposes. For e.g., a network card could tap into the PCI bus and send an image down a network to a remote location.

Visions of development of an on-camera FPGA imaging system, titled "SmartCam" emerged. The FPGA would interact with the camera, grab frames, perform certain image processing functions such as image cropping (to remove the significant central portion of the frame) frame averaging (to remove noise) and dewarping (to remove distortions) and provide the host PC with nice, clean , cropped images. This report describes the methods used by the team to design a system that would act as a proof of concept behind the idea of SmartCam.

The System

For establishing the proof of concept, the following system was designed. As an alternative to actual cameras, the National Instruments NI PCI-6602 board was used.
A simple application in Visual Basic was written to output a definite pattern of 1's and 0's as pixel data to the FPGA at the same time providing the necessary pixel clock and the two control signals Line Enable and Frame Enable as per the camera specifications.
The emulator was designed to provide control and data signals in the same manner as the original camera specifications, with the exception that the pixel clock was set at a much lower frequency of 100 KHz as opposed to the camera's 27 MHz.

The NI PCI-6602 DAQ board is basically a PCI-based high-speed digital I/O board. It offers four 32-bit counter channels and up to 32 lines of configurable TTL/CMOS digital I/O [5]. Using the NI-DAQ driver software to gate the channels in a suitable manner, the camera data and the control signals were generated.

The output signal voltage was at +5V. The operation of the FPGA was set at +3.3 V. A suitable voltage divider circuit was built and the three inputs where then given to the Celoxica ADMXRC II card (that contains the Xilinx Virtex-II FPGA) by means of a 34-pin end connector. The design is illustrated in Figure 3.
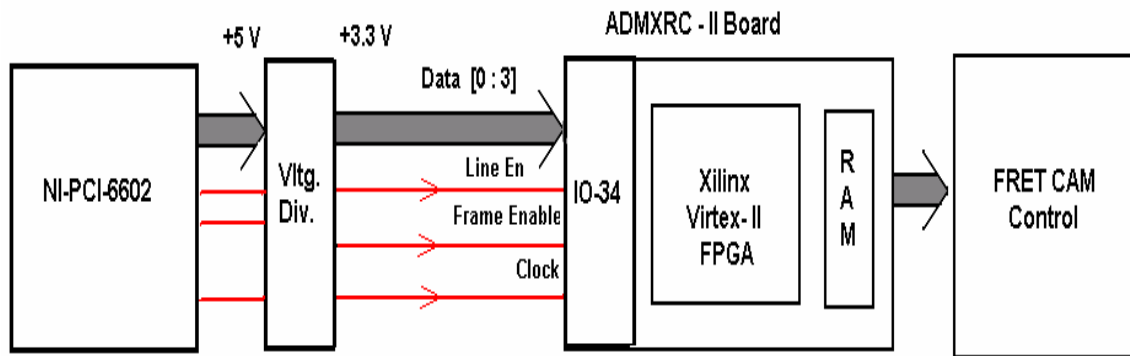
Fig 3: Block diagram of the system

The DSM (Data Stream Manager) libraries of Celoxica DK Design Suite provide a bus-and-OS independent transfer of data from the reconfigurable hardware to the host PC and vice versa. The transfer is done through underlying hardware and software bus controllers. Figure 4, from [6], depict the structure of DSM.
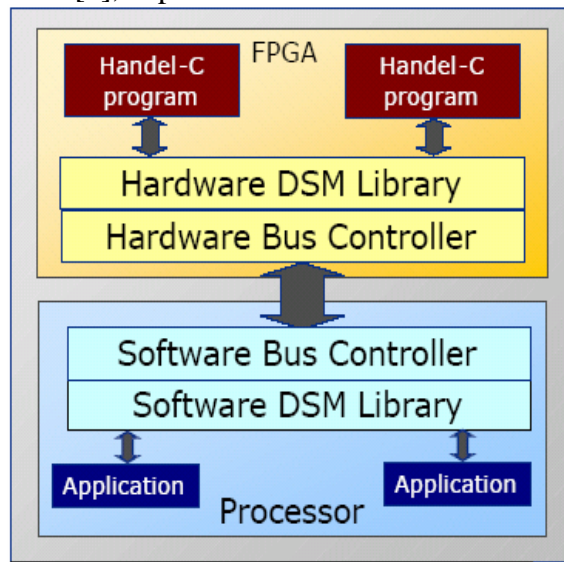

Fig. 4: Basic operation of the DSM

As the low frequency of the input clock was insufficient for transfer of data across the bus from the FPGA to the camera, a multiple clock domain configuration was designed. One domain reads in data from the pins and sends them down a channel, while the other operating at a faster rate transfers the data across the bus, into a buffer located on the host PC memory. However, the multiple clock domains configuration led to problems of missing data. This might be due to the latency in sending data down the channel which resulted in certain fixed amount of data that appeared at the pins during this intermediate stage, to be lost.

Thus, an alternative design had to be implemented, wherein a fast internal clock was used to run a single clock domain. The data from the pins were however latched at the rising edge of the external clock. This design was subsequently tested out for higher frequencies such as 27MHz and found to be stable. The image acquired from the FPGA was integrated into the existing FRET Cam application. This application, originally designed to interface with the capture board was changed now to interface with the FPGA. Due to the definite two 0's two 1's pattern that the camera emulator gave as input to the FPGA, the resulting image given to the host is in the form of stripes as shown in Figure 5.
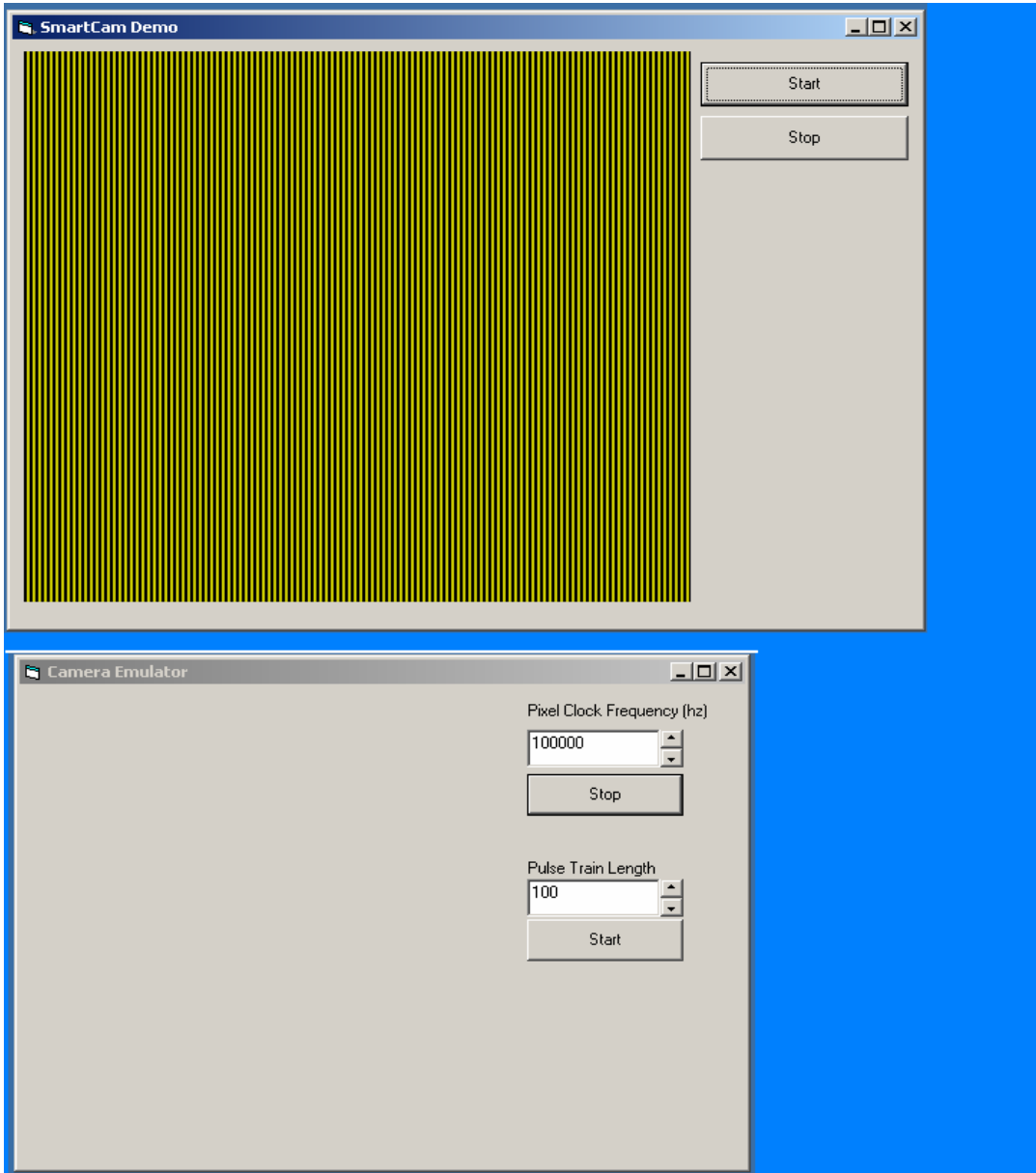

Fig. 5: The Camera Emulator and SmartCam Applications

The bottom "Camera Emulator" box is used to program the NI PCI-6602 DAQ board at a user–defined frequency (here set to 100 KHz). The "SmartCam Demo" box illustrates one 800x600 frame acquired from the DAQ board using the FPGA. The stripes show an enhanced depiction of the alternating 001100...pattern that the DAQ was designed to give.

Future Work

Once the proof of concept is complete, the next step would be to test out the configuration on the Uniq 1800 cameras. The 34-pin connector will be replaced by a 146-pin connector with proper LVDS (Low-Voltage Differential Signaling) termination that is required for proper interfacing with the camera.

The next step would be incorporate plug and play modes of transfer such as USB-II and Firewire. Another intended direction of work is to provide various image processing functions such as averaging and dewarping, along the lines of previous work explained in [7], which can be performed subsequent to capture.

References:

[1] M. S. Resat, J. C. Solinsky, H. S.Wiley, K. A. Perrine, T. A. Seim, and S. E. Budge, "3-d multispectral monitoring of living-cell signaling using confocal-imaging and FPGA processing," in IEEE International Symposium on Biomedical Imaging (ISBI 2004), (Washington D.C.), p. 680683, 2004

[2] J. C. Solinsky, C. R. Batishkoa, S. E. Budge, P. D. Majors, M. Sowa-Resat, and B. Rex, "Real-time, image analysis of living cellular-biology measurements of intelligent chemistry," in Sixth International Conference on Quality Control by Artificial Vision, vol. 5132, (Bellingham, WA), 2003

[3] Uniq Cameras, "UP-1800 Progressive Scan CCD Camera User Manual"

[4] Coreco Imaging, Inc., "PC-DIG Hardware Product Brief"

[5] National Instruments Corp., "NI PCI 6601/6602 DAQ User Manual"

[6] Celoxica, Inc., "Platform Developer's Kit –DSM User Manual"

[7] S. E. Budge, A. M. Mayampurath, and J. C. Solinsky, "Real-time registration and display of confocal microscope imagery for multiband analysis," in Thirty-Eighth Asilomar Conference on Signals, Systems and Computers, Nov. 2004.

Fabrication of carbon nanotube, metal, and polymer nanowires composite

Fung Suong Ou and Pulickel Ajayan
Dept. of Material Science and
Engineering
Rensselaer Polytechnic Institute

and

Laxmikant Saraf
Pacific Northwest National Laboratory
Richland, WA

A rob like building blocks consisting of gold and conductive polymer has been fabricated by using template electrochemistry synthesis. They were reported to have interesting self-interaction, and interesting self-assembly. The template not only helps to align the wires. Further, by varying the sizes of the anodic alumina template, different sizes of the nanowires can be produced. We have successfully reproduced this structure made by Mirkin et al. This is however only the beginning for our envisioned final structure which is a composite of carbon nanotube, metal, and polymer nanowires. Coupling our ability to grow nanotubes inside the alumina template in our laboratory with the electrochemical deposition experience at PNNL, one should be able to fabricate the composite. We still were not able to fabricate the structure due to some technical difficulties. But with continuing work, the envisioned structure can certainly be accomplished.

[1] Sungho Park *et al.* Science, 303, 348

Hydrogen Storage: Studies on ammonia borane as a possible solidstate material

Benjamin A. Schmid   S. Thomas Autrey
University of Oregon   and   Pacific Northwest National Laboratory
Eugene, OR   Richland, WA

The DOE's goals for the weight percent of hydrogen in a material are: 2005 (4.5 wt%); 2010 (6.0 wt%); 2015 (9.0 wt%). In addition to these storage requests, the material should also be able to deliver at temperatures between -20 and 85˚C. A material that has garnered interest is ammonia borane (NH_3BH_3). This compound has notably high hydrogen content. Starting from NH_3BH_3 and ending at BN provides ~19 wt.% hydrogen. The temperatures for the evolution of hydrogen are respectively <100˚C, <170˚C, > 500˚C.

Tom Autrey and coworkers at PNNL have targeted this material to meet the DOE's goals. A major drawback to this material is the formation of borazine, a benzene analog, upon decomposition. Also, the temperatures are above those desired for the applications of interest, specifically fuel cells. It was discovered that upon placing the NH_3BH_3 onto a mesoporous silica "scaffold", significant improvements are made in the material. The temperature for hydrogen release is significantly reduced, and more importantly, the formation of borazine is inhibited.

This summer I worked in several areas of the project. Synthesis of the desired compounds was needed for conducting measurements. NH_3BH_3 can be commercially purchased; however our experiments required deuteration and/or functionalization of the original material. Several methods were explored to develop optimal pathways for the synthesis of the desired compounds. Pathways leading to high yields and purity were necessary, since the scaffold loaded material quickly degrades, even with refrigeration.

Characterization of these compounds was obtained primarily through either differential scanning calorimetry (DSC) or nuclear magnetic resonance (NMR). Two different DSCs were utilized to study the thermal decomposition of the materials. Baseline data for the heat of decomposition was determined with a Calvet C80 calorimeter. Data collected with a Netzsch 490 STA/TGA with attached quadrupole mass spectrometer was sought to determine the formation of borazine, both pure and on the scaffold. Different loading ratios were studied to determine the optimal amount of NH_3BH_3 on the scaffold. Our results indicated that the formation of borazine is significantly reduced for initial lower loadings of NH_3BH_3 onto the scaffold. The borazine reappears at higher loadings showing a return to pure NH_3BH_3 decomposition character. These initial results are encouraging and lead us to believe there is a maximum loading density, or surface interaction, after which the properties given by the scaffold deteriorate. Optimization of the material has yet to be achieved but will continue to be targeted.

Studies of rotational dynamics in the material neat and on the scaffold were conducted using four different NMRs. Three 300 MHz and an 800 MHz NMRs permitted measurements from -165^0C to 80^0C. This allowed us to slow the kinetics down

to an observable speed, for low temperatures, and decompose the material as it was being observed in situ, at higher temperatures. The last five weeks of my internship were mainly focused on data collection using the above two methods. I will be assisting Tom's group in running simulations and interpreting the data upon returning to the University of Oregon.

My internship will culminate with my finally week being spent at the National Institute for Standards and Technology (NIST) in Gaithersburg, MD. There I will be assisting in neutron scattering experiments to supplement our NMR data.

Holding single molecules in solution using magnetic tweezers: a new approach to studying DNA damage recognition by proteins

Andrew D. Shaller, Jason J. Han and Alexander D. Li
Washington State University
Pullman, WA

and

Douhai Pan and H. Peter Lu
Pacific Northwest National Laboratory
Richland, WA

Abstract

The research objective for the 10-week summer internship at PNNL was to continue to demonstrate the technical feasibility of coupling single molecule spectroscopy (SMS) with magnetic tweezers as a new method for studying DNA-protein interaction on single DNA molecules in solution. This method combines magnetic tweezers, which are used to attenuate Brownian motion and hold a single DNA molecule in solution, and SMS, which provides dynamic and conformational information of non-ensemble DNA-protein interactions. Jason Han, a 2004 SRI participant and graduate student also working for Alex Li at WSU, adapted a method for tethering magnetic beads to a glass cover slip utilizing the cohesive ends of bacteria phage λ-DNA and the biotin-streptavidin interaction.[1] The goals for continuing this work included: 1) optimize the attachment procedure to achieve consistent coverage of tethered beads on each slide while maintaining sufficient separation to reduce interactions with adjacent tethers; 2) Optimize addition of intercalating fluorescent dye to achieve a high signal-to-noise ratio and demonstrate feasibility of SMS; 3) Characterize and develop a protocol for the newest generation of magnetic tweezers; 4) Use the magnetic tweezers to study a specific DNA-protein interaction. Significant progress was made on each of these goals; however the quantity of data is not currently sufficient to publish in a peer-reviewed journal.

Background

While the coupling of magnetic tweezers and SMS has been suggested[2] but not realized, the use of magnetic fields to manipulate single molecules of DNA has been well established. Streptavidin coated superparamagnetic beads attached to biotinylated DNA have been used to measure the force-extension curve of dsDNA,[3] the force-extension curve of super-coiled dsDNA,[4] and the torque as a function of DNA twist.[5] Other methods have been used to manipulate or measure forces in single molecules such as covalently attaching DNA to a polystyrene bead trapped with optical tweezers,[6] holding a bead with a glass pipette by suction,[7] using hydrodynamic drag forces,[8,9] or utilizing covalent attachment to an AFM tip.[10] However, magnetic tweezers offer several advantages over these techniques. First, they allow low force (fN to ~200pN) manipulation or measurements. Second, the magnetic field does not heat or otherwise disturb the sample. Magnetic tweezers are able to control the force over a relatively large area (20μm to 2 cm), which is ideal for high NA lenses, and they can be used to apply torque to rotate the molecule. Finally, it is possible to use a computer to control the

magnetic field and thus regulate the attenuation of Brownian motion during single molecule studies.

Several different magnetic tweezer designs are reported in the literature. The most common approaches use strong rare-earth permanent magnets that are either rotated as a pair around the sample[11-13] or stacked vertically above the sample.[14,15] Micro-magnets have been attached to the end of glass pipettes as a near-field approach.[16] Advantages of permanent magnets are they provide a strong magnetic field over a large area with no generated heat or electrical current. With typical magnets and 2-4 μm diameter beads, the magnets can be positioned up to one centimeter away from the sample and still provide enough force (at least 0.5 pN) to significantly extend the DNA. However, micro-sized adjustments in distance are required to precisely control the force. Another methodology uses electromagnets where the force can be adjusted by manipulating the current. Designs range from large-current (2-6 ampere) water-cooled tweezers with a two centimeters working distance[17] to a lower-current approach with micron-sized tweezer tips that are only 20μm apart.[18] Advantages of electromagnets are they can be electronically controlled without bumping or disturbing the sample. This allows precise two-dimensional manipulation of magnetic beads in solution when combined with a computer feedback mechanism.[19, 20]

In the method reported here, millimeter-sized electromagnetic tweezer tips are positioned only 2 to 3 millimeters apart centered above the microscope objective (Figure 1). Using this approach, a moderate 1.5 amps or less is required to create significant perturbations to 1.5μm sized superparamagnetic beads with minimal heat generation.
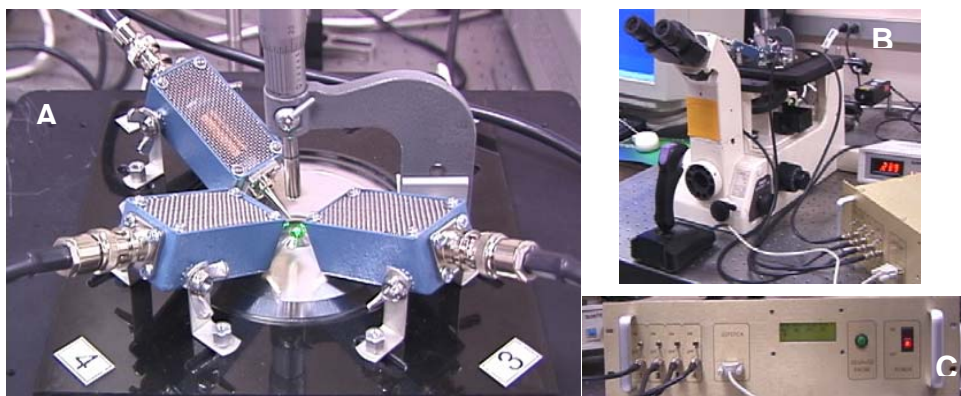

Figure 1. Magnetic tweezers. A) Close-up of the 3rd generation magnetic tweezers designed at the EMSL. Notice the permanent magnet located vertically above the sample. (One of the four electromagnets is missing in this picture while it was being used in the development of the 4th generation tweezers.) The 4th generation (not shown) adds micro-precision adjustment of the magnets. B) Experimental set-up. Nd-Yag laser (532) is seen behind inverted microscope. Tweezers are positioned on the stage. Joystick in front of scope controls the magnetic field. C) Controller that allows joystick manipulation of current to each magnet separately.

There are a few published methods for attaching DNA between a magnetic bead and the cover slip. Several papers report annealing biotin or digoxigenin modified oligos to the cohesive ends of the l-DNA and then attaching them to an antidigoxigenin coated slide and streptavidin coated bead.[3,11,21] Alternatively, l-DNA and oligo-coated beads were

added to an oligo-covered slide; the DNA was then tethered by annealing to the complimentary probes on the bead and slide.[14] Another approach ligated a biotinylated oligo to one end of the l-DNA in solution and then hybridized the biotinylated DNA target to probes attached to the surface.[17] We adapted the procedure here from the last method. Nucleic acids were silanized using disulfide bonds and then attached to a glass cover slip. The 48 kbp biotinylated l-DNA target was then hybridized to the probes on the slide surface.

Procedure

The procedure established by J. J. Han[1] was generally closely followed and only deviations from this procedure are included in this report.

Materials. All materials were re-purchased at the beginning of the 10-week research period and stored as recommended by the manufacturer as described in the original procedure. The exceptions were superparamagnetic beads, POPO-3 dye, and (3-mercaptopropyl) trimethoxysilane, which were stored for one year under the manufacturers suggested storage conditions.

Magnetic bead attachment. As described previously,[1] many non-tethered beads adsorb directly to the glass surface. By adding a drop of TET buffer prior to application of the beads, non-specific attachment was greatly reduced and the majority of the non-tethered beads were washed away when rinsed with TET buffer following attachment. Most of the remaining non-tethered beads were pulled from the viewing area to the edge of the drop with a permanent magnet and removed from the slide by pipette. This is necessary prior to using the magnetic tweezers, which pull non-tethered beads back and forth in solution where they may magnetically couple with tethered beads under observation.

It was also discovered that repeated sonication of the bead solution to divide aggregates following storage results in degradation of the beads and less coupling efficiency. Over about ten storage-use cycles, the beads break-up into tiny micron or smaller shards which apply less force in a given magnetic field, have less affinity for biotinylated tethers, and tend to aggregate more. Using a vortex to resuspend the beads was found to sufficiently break-up aggregates and did not cause significant degradation over several weeks.

Drop confinement. Using a Sharpie marker to circle the treated area on each slide makes finding the sample area easy and maintains a hydrophobic perimeter to contain the aqueous solution. However, the dried ink frequently flakes off when in contact with the buffer solution. This is especially true when using TET buffer (containing Tween-20). The flakes do not affect the attachment chemistry or the fluorescence of the intercalating dye, nor do they fluoresce under the 532nm laser. However, they may interfere with the DNA tethers. More importantly, when the liquid drop is contained by the hydrophobic force of the ink and it suddenly breaks, the hydrodynamic forces of the solution flowing out of the contained area are enough to break some DNA strands while others become "combed" onto the surface; this also frequently results in tethered beads becoming

adsorbed to the surface or tangled with other tethers. The contact angle of the buffer was found to be sufficient to contain the sample during reactions and measurements. Also, this made rinsing of the slide between steps easier.

Drop size. Upon application of biotinylated DNA to the slide during hybridization, DNA not specifically attached to the slide tends to aggregate near the perimeter of the drop due to evaporation or convection currents within the solution. This effect was even more pronounced in low-ionic (10mM) solution where 90+% of the DNA aggregated on the slide surface at the liquid-vapor interface. Using smaller drop sizes in an array pattern with a smaller volume-to-surface-area ratio minimized this problem. Also, by using smaller (~1uL) drops for the silanized-oligomer application and slightly larger drops (~4uL) for the biotinylated DNA application, it was possible to tell under the microscope by the size of the radius if changes in coverage densities were a result of changes to the DNA or the silanized-oligomer application.

Biotinylated DNA concentration. The DNA concentration (8μg/mL) was determined to be too high after staining and viewing by fluorescence. Most DNA was either tangled with adjacent strands or close enough to be significantly perturbed even when not extended. Since λ-DNA stretches out to almost 17μm under moderate forces (0.5-65 pN), it is ideal to have the tethered DNA strands at least this far apart. However only 10-20% of the DNA attaches to any beads and thus the coverage should not be so dilute that only a few tethers are found on the slide. It was found that a further dilution of 1:100 was required for ideal coverage. An important factor to remember when considering the dilutions is the degradation of the oligonucleotides over time (2-3 months) in storage at –20C. Thus, as the reactants degrade, this "optimum" concentration may need to be increased.

Ionic concentration. Following hybridization, up to 90% of the DNA became non-specifically aggregated to the slide near the perimeter of the solution (as discussed above). The aggregates were so dense that many beads became attached with each bead connected to multiple tethers. At a given concentration of DNA, only a small percentage became evenly spaced single tethers available for attachment to a single bead. It was discovered that adding NaCl in a concentration range of 0.5 to 2M caused the DNA to singly tether to the surface with an even distribution across the entire slide. There was only a slight perimeter effect with the density of coverage in the center almost identical as near the edge of the drop. Similar ionic effects have been characterized before.[22] Thus a concentration of 1M NaCl was used for all successive experiments.

Fluorescent staining. POPO-3 dye was used for staining as in the previous procedure[1] where it was suggested the dye caused unacceptable background fluorescence for SMS. Hence the first attempt was to stain the DNA in solution prior to hybridizing to the slide. It was found that the DNA could be stained (at the manufacturer recommendation of one dye molecule for every 4-5 base pairs) and the stain would remain intercalated after running through a sephadex-G25 column. This stained product could then be stored at –20C and used for later hybridization. However, the dye established equilibrium with the solution and insufficient amounts remained intercalated when the sample was diluted

upon storage, application, or rinsing. It was found that the best method for staining was to apply the dye directly to the slide at dilute concentrations. When the dye was too concentrated, the solution had unacceptable background and signal-to-noise. At too low of a concentration, the DNA was not visible. However, when small volumes of highly concentrated dye were added to the slide, some areas became excessively stained while others were under-stained. An optimum concentration of dye with fairly homogeneous distribution was found when 1-10 μM POPO-3 (diluted in TE buffer) was added to the slide by micropipette in μL sized drops.

One detail for adding the dye is that it should be diluted in TE buffer with a pH very close to the pH of the sample solution. If the dye is diluted in water, the pH may be excessively low and will cause the DNA to irreversibly adsorb to the surface as a single visible fluorescent point and remain unavailable for further tethering. Another important point is that, as reported elsewhere,[23] POPO-3 stained DNA is not visible at high ionic concentrations.   The addition of 1M NaCl will cause almost complete loss of fluorescence. Thus when sodium chloride is used during hybridization, the slide must be rinsed thoroughly to ensure the ionic concentration is reduced prior to staining. A final point regarding the storage of POPO-3 is that it was found to be stable for at least one year when stored in DMF at –20C. The manufacturer recommends using the dye within an hour of diluting it in aqueous solution, but once diluted in TE buffer, the dye was found to be fully functional when stored at –20C for up to one year, or at 4C for a week or two.

Addition of radical scavenger. The intercalated POPO-3 dye was found to photobleach too quickly to capture spectra or lengthy video images upon laser excitation in TE or TET buffer. At laser power high enough to view wide-field fluorescence with the human eye (about 25mW) the dye was photobleached >90% in 8-10 seconds. At higher laser power sufficient for 15 frames/sec video recording, this was 2-3 seconds. It was attempted to bubble N_2 gas through the buffer solution prior to rinsing and viewing the slide to remove dissolved oxygen but this was found to have little effect. Then three different radical scavengers were tried: 1,4-phenylenediamine, ascorbic acid, and mercaptoethanol. All three were found to significantly reduce photobleaching of the dye from 8-10 seconds without the scavenger to 50-70 seconds with the scavenger (at ~25mW). However, ascorbic acid can change the pH of the solution if not carefully prepared in buffer and the mercaptoethanol can undergo an exchange reaction with the disulfide linkage of the tethered DNA. Thus, one to five μL of 0.015M 1,4-phenylenediamine was used as a scavenger for all subsequent fluorescent measurements.

Results and discussion

Bead Trajectories. As a method of quantifying tethered bead travel while undergoing Brownian motion or while under the influence of a magnetic field, .avi video files captured from a CCD were converted to multiple .tif single-frame pictures. These were

then successively analyzed using a gaussian fitting algorithm written in the Lu lab that provides precise x and y coordinates of the bead in each frame. This data was input into an x-y plot that allows a time-lapse visualization of the 2-dimensional bead movement (Figure 2). Further analysis is then possible such as calculating the standard deviation in bead position or bead velocity. In Figure 2, the (x, y) positions (in pixels) have a standard deviation of (3.4, 3.6) in the absence of a magnetic field but are reduced to (2.4, 2.9) under the influence of a Co-Sm magnet. The deviation is reduced even further when the magnet is moved closer to the sample, where the DNA tether is stretched near its full-extended length and the standard deviation for (x, y) is reduced to (1.4, 1.2).
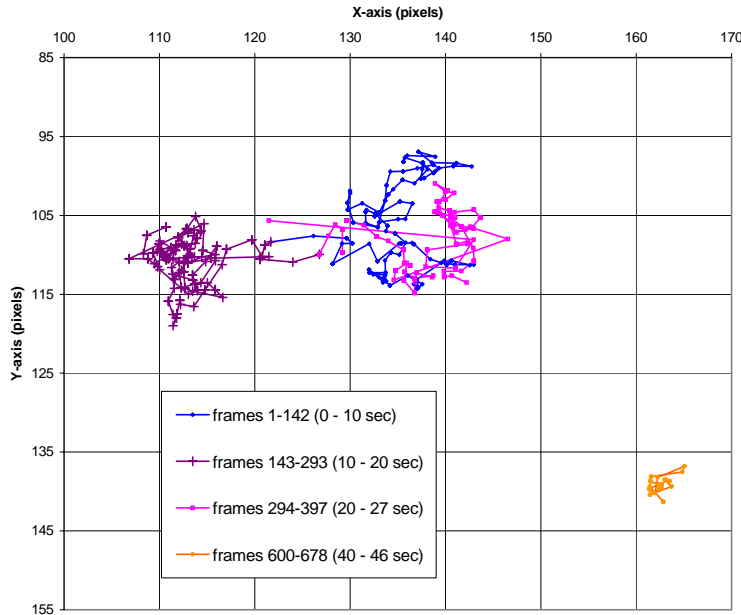
Figure 2. The x-y trajectory of a single tethered bead (non-stained DNA). From 0 to 10 seconds, the bead is undergoing Brownian motion in the absence of a magnetic field. From 10 to 20 seconds, a permanent magnet is used to pull the tethered bead laterally (and slightly vertical) from its original average position and the Brownian motion is attenuated somewhat. At the twenty-second mark, the magnet is removed and the bead returns to the vicinity of the original position, with the previous range of Brownian motion. At 40 seconds, the magnet is applied in a different direction closer to the sample. This increases the force on the bead, the DNA tether is extended to near its full-extended length of 17μm, and the Brownian motion is attenuated significantly more. Video recorded at 14.8 frames / sec. Each data point represents two frames (~0.15 sec apart). Line is a straight-line fit between successive data points for visualization. Recoded image is 320 x 240 pixels, where 1μm is approximately 2.6 pixels.

Similar data analysis was performed on a bead under the influence of the 3rd generation magnetic tweezers developed at the EMSL (Figure 3). A single tethered bead was followed undergoing random motion. The magnet closest to the sample was then increase to 100% current and the bead trajectory recorded. As in the case of the permanent magnet, the standard deviation in the (x, y) position decreased from (3.4, 2.6) to (2.3, 2.4) after the magnet was applied. The deviation in the x and y directions can be plotted as histograms and compared to fitted gaussian curves (Figure 4). The tethered Brownian motion has considerable range and relatively low velocity; both x vs. y dissymmetry and imperfect gaussian curves are attributed to an insufficient period of data collection. The average position only changed by 22.5 pixels (~8 μm) indicating the tether was not fully extended. As predicted by the measurement of the magnetic field from the tip, the electromagnets are not strong enough to fully extend the DNA unless they are within a millimeter or two of the tether, which would place them inside the meniscus of the liquid drop. However, as in this case, when the magnet is 3 to 4 millimeters away (just outside the water drop) the magnet is still able to noticeably attenuate the Brownian motion and extend the tether to almost half its full-extended length. Positioning all of the magnets precisely within this distance was difficult with the 3rd generation tweezers but realized with the 4th generation prototype.
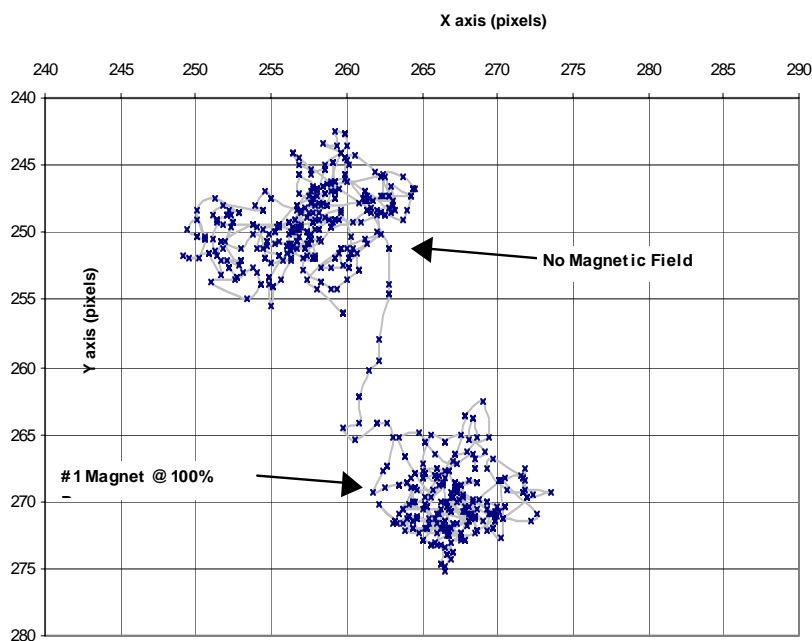

Figure 3. Trajectory of tethered bead before and after application of one electromagnet at 100% power. Video was recorded at 14.8 frames / second, with data points representing every 3rd frame (~0.2 sec interval). The line is a smoothed line fit to help visualize bead movement. Full recorded image was 640 x 480 pixels, where ~2.6 pixels = 1μm. Note the tether is extended only about 8μm, less than half of its full-extended length.
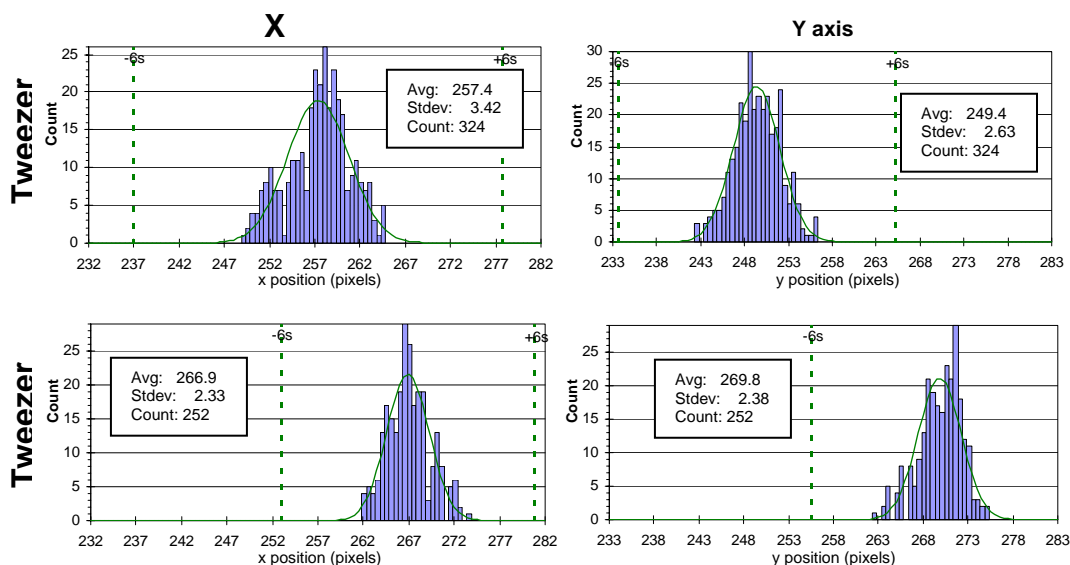
Figure 4. Histograms of bead position in the x and y axis both before the tweezers were turned-on and after. Prior to turning-on the magnetic field, the (x, y) standard deviation was (3.4, 2.6) and after application of the magnet decreased to (2.3, 2.4).

The x-y bead trajectory provides a visualization of the two-dimensional movement in solution but the tethered bead is actually undergoing motion in the vertical (z) direction, as well. While the z-direction movement cannot be recorded directly in a 2-dimensional CCD image, the vertical movement is indicated by plotting the intensity of the image over time (contrast between the bead and the background). With the 60X 1.4NA lens, the focal plane is about one micron deep. When the 1.5 μm bead is centered within the focal plane, the image intensity is near 100%, whereas when the bead is far out of focus the intensity drops to near zero (no contrast with the background). Thus if the bead is initially slightly out of focus prior to application of the magnetic field and then the field is applied, the bead is pulled more into or out of focus and is recorded in the bead intensity plot (Figure 5). It is generally the case that the z-direction fluctuations are smaller when the bead is undergoing Brownian motion and increase under application of the magnetic field. It is believed this is a result of the DNA exerting more force on the bead as the tether is extended which causes greater fluctuations in the z-direction.
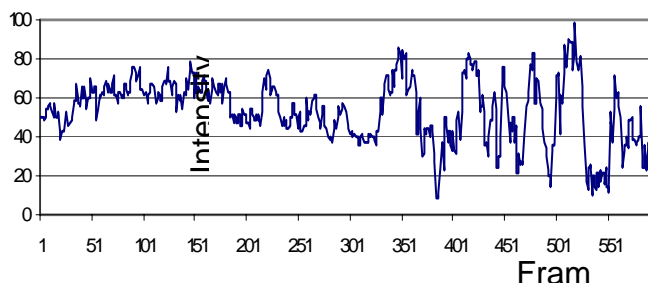

Figure 5. Plot of image intensity (contrast of bead against the background) for each frame. The first ~320 frames are recorded prior to turning-on the magnetic field. Around frame 320 one of the electromagnets is increased to 100% power and is noted by an increase in the fluctuations in intensity after this point. Image intensity is near 100% when the bead is exactly in focus and drops to near zero when the bead is far out of focus. There are about 14.8 frames per second.

Power of magnetic tweezers. It was observed with the third-generation magnetic tweezers that the electromagnets applied significantly less force to tethered beads than the

permanent magnet did. While the permanent magnet was able to fully extend the λ-DNA to its contour length of ~17µm at the point of elastic stretching, the electromagnets were only able to extend the DNA to less than half this length by opposing the entropic elasticity. To quantify this observation, a magnetometer was used to measure the magnetic field of both the Co-Sm magnet and of one of the electromagnets (Figure S4, supporting information). The magnetic susceptibility of 1.5 µm beads is not known, but the manufacturer published susceptibility of 2.8 µm diameter superparamagnetic Dynal beads is $M_{max} \cdot V = 1.42x10^{-13}$ A·m^2. Utilizing published force extension curves[3,6] at least 0.5 pN is required to extend λ-DNA to ~75% of its taut length. Thus the change in the magnetic field with distance is required to be at least 3.6 T/m for the 2.8µm beads, which is achieved up to 0.8cm from the surface of the permanent magnet but only to a distance of 0.2cm from the tip of the electromagnet at 100% current. 1.5µm beads are used in the procedure followed here; thus the field may be required to be up to four times stronger than calculated with 2.8µm beads.

Modification to 3rd generation tweezers. In an attempt to possibly strengthen the force from the tweezers, a mid-generation modification was made to the 3rd generation set. A micro-adjustable permanent magnet was added in a vertical position above the "focal point" of the electromagnets in order to extend the DNA tethers where the electromagnets might better attenuate the random motion (Figure 1). It was found that with the magnet adjusted to within one centimeter of the slide surface, all tethered DNA on the slide was extended vertically with the tethered beads in a focal plane 10-20 µm above the surface. In this case, the electromagnets were not strong enough to make significant horizontal changes to the bead position. Additionally, the electromagnets were not firmly fastened and could suddenly snap up towards the permanent magnet. However, when the vertical magnet was raised to between one and three centimeters high, it did not completely extend the tethers and the electromagnets became more important in controlling the bead position (Figure S1, supporting information).

Micro adjustment. In the 3rd generation tweezers, the electromagnets were fastened with screws and wing nuts that allowed the magnetic tips to move excessively (2-3 mm). Since the tips are required to be about one millimeter from the sample to exert sufficient force on the DNA, it was difficult to establish a fixed magnetic focus. Introducing micro adjustment to the 4th generation tweezers reduced this problem. Micrometers on each magnet allow facile adjustment of tip proximity and thus adjustable strength of the maximum magnetic field. This also enables fine-tuning of the magnetic field so that a bead experiences a symmetrical maximum force. (The magnets have slightly different maximum fields and a bead may not be in the exact equidistant focus of the tweezers). When tested, the 4th generation prototype was only fitted with temporary guides and still had unacceptable side to side or up and down movement which will be remedied in the final product.

The fourth generation magnetic tweezers were used to manipulate a tethered bead in four different directions by increasing the power to 100% successively between magnets (Figure 6). With the magnets adjusted to millimeter distance from the tethered bead, the electromagnets are capable of manipulating the bead in all directions. However, the force

on the bead by each magnet is dependent on the proximity of the magnetic tip to the bead. This is demonstrated by a bead trajectory (fig. 6) where the tether is extended further by some magnets than others. With the same tethered bead, a ~40 second trajectory was recorded both with and without an applied magnetic field (see supporting information, figure S2). It was found that the standard deviation in (x, y) was attenuated from (3.9, 4.0) to (2.9, 2.0) with the magnetic tweezers.

Addition of protein. To further demonstrate the feasibility of using the magnetic tweezers in the measurement of DNA-protein interactions, bead trajectories were captured and analyzed upon the addition of protein to the sample. Analysis of this type has been performed previously.[13,16] HMGA1a, a High Mobility Group protein, is involved in the regulation of chromatin structure.[24] It consists of 107 amino acid residues with three AT-hooks and an acidic C-terminal region. The three AT-hooks are responsible for binding to AT-rich sequences in the minor groove of DNA. The protein was hydrated in TET buffer and stored as 1μg/ μL aliquots at –20C until ready for use. The protein was diluted from 0.1 to 100ng per μL with TET buffer and added directly to the slide while a tethered bead was under observation. Trajectories were captured before, during, and after protein application. Generally, the protein caused a decrease in Brownian motion and the inability of the tethered DNA to be extended to the same length as before application. The reduction in the Brownian motion was dependent on the protein concentration.
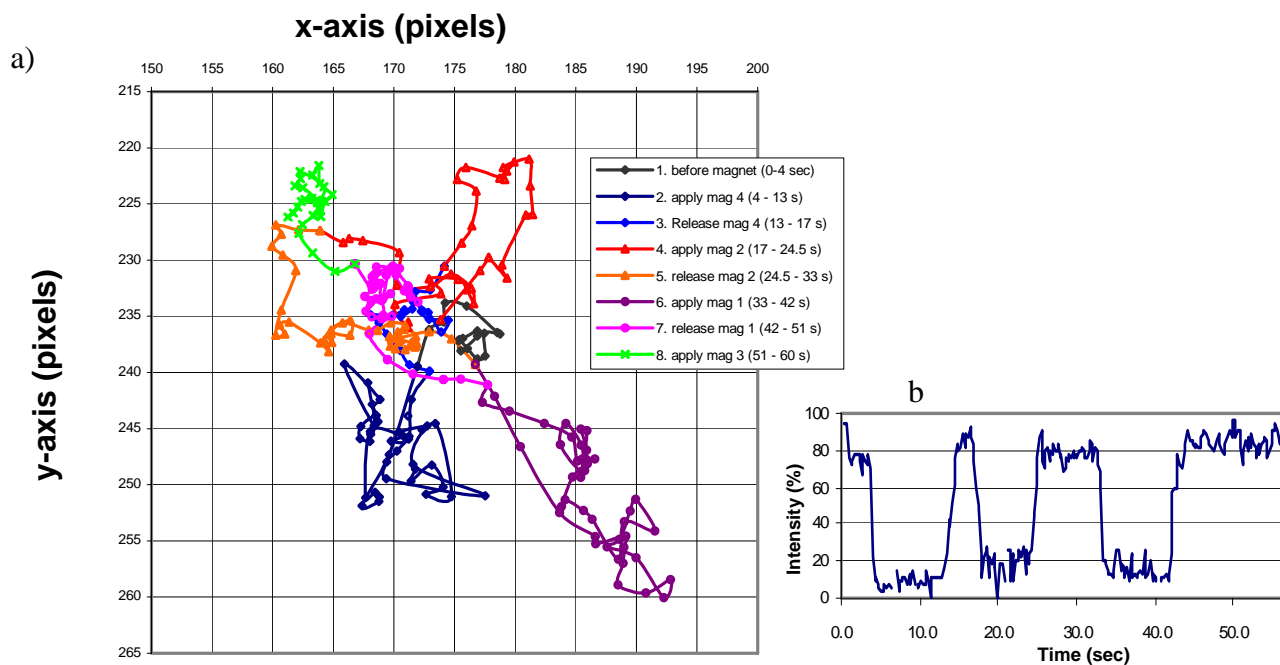
a)

Figure 6. a) Trajectory of a tethered bead under the influence of the 4th generation magnetic tweezers. The bead is first pulled to the lower left, then the upper right, the lower right, and finally the upper left. In each case the bead relaxes to nearly the same equilibrium position where it resumes Brownian motion. Some legs are longer than others because the tip of each magnet is a slightly different distance from the tethered bead. b) Bead image intensity vs. time plot for same trajectory. Bead is originally in good focus prior to application of magnetic field. Each time a magnet is turned-on, the bead is pulled out of the focal plane and the image intensity decreases. Note when magnet 3 is applied, the bead is pulled the least laterally and the bead remains mostly in focus.

When 4μL of 100 ng / μl protein was added to the approximately 40 μL solution on the slide, the attenuation was almost instantaneous and severe. All tethered beads on the

slide became immobilized with greatly reduced Brownian motion, and the magnetic tweezers made no noticeable extension of previously extendable tethers. At lesser concentrations, the attenuation rate was slower as the protein diffused across the drop. Under these conditions, the trajectories show a gradual decrease in Brownian motion until the tether eventually becomes practically immobilized in one location (Figures 7, 8). One forty-second trajectory was recorded at even more dilute concentrations (Figure S3, supporting information) with minimal difference before and after the protein application. Recording trajectories for longer time periods and at various intermediate concentrations will likely demonstrate examples where there is a noticeable change in the random motion but is not attenuated completely.

Additional analysis. It is possible to analyze the data from the bead trajectory in several ways. For example, the distance traveled in the x-y plane by a tethered bead can be plotted as a function of time. A tethered bead under random Brownian motion will fluctuate around an average distance traveled over time. However, during transient states such as when a magnetic field is applied, the bead has a higher velocity and thus a greater x-y distance trace (Figure 9). Another example is to calculate and plot the x-y angle between three successive data points (not shown). Under normal Brownian motion, the bead continues in the same general direction for 3 or 4 frames at a time on average so the average angle between three points is higher. However, when a magnetic field extends the tethered bead, the bead is confined to a smaller area by the magnetic field and the DNA tether, the bead changes directions much more often, and thus the average 3-point angle is smaller.
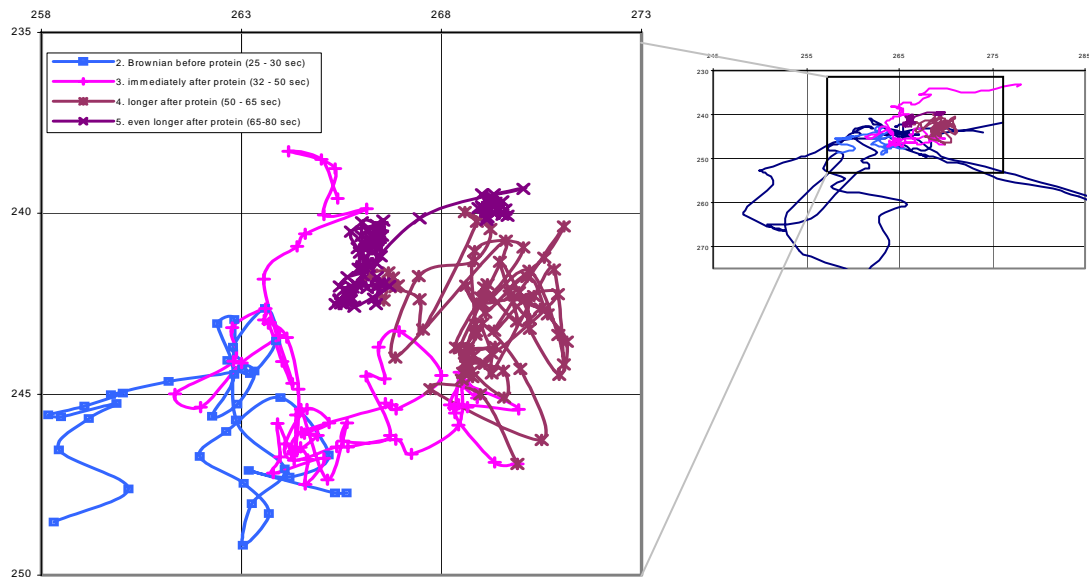

Figure 7. Trajectory of tethered bead just before and then after addition of HMGA1a protein to slide. From the moment of protein application, the Brownian motion becomes more and more attenuated until the standard deviation from 65 to 75 seconds is only (0.4, 0.8) pixels in the (x, y) coordinates. Inset shows Complete trajectory where a permanent magnet was used to extend the tethered bead several times prior to addition of the protein.
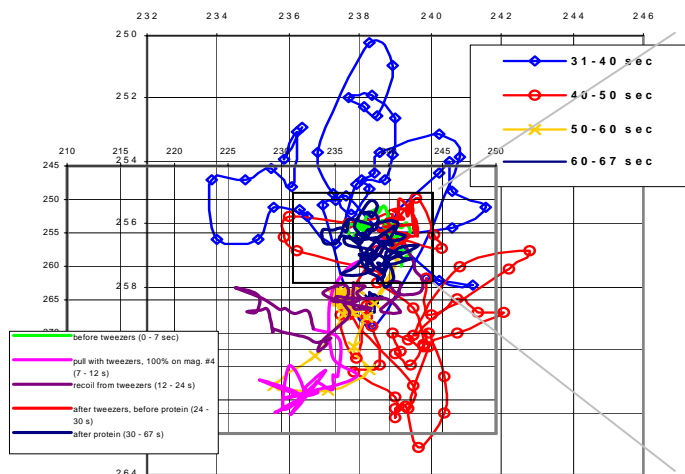
Figure 8. Full tethered bead trajectory is shown on the left where the tether is extended with the magnetic tweezers to demonstrate it is singly tethered. Then the bead rebounds to its original position where it resumes free Brownian motion prior to protein application. On the right is shown the enlarged trajectory of the bead after HMGA1a protein is added to the slide. As time progresses, the Brownian motion becomes more and more attenuated until the bead is practically confined to a fraction of its range prior to the protein.

Non-specific attachment. Upon discovering the hybridization step is more efficient when carried out in 1M NaCl, an experiment was performed to confirm the DNA attachment to the slide was specific hybridization instead of non-specific adsorption. From visual observation it appeared that >90% of the DNA was singly attached to the slide on one end. Further, with a bead attached to the free end, the magnetic tweezers were able to extend the DNA to about half its contour length. However, if even a small percentage (say 5kbp) of the 48 thousand base pairs were non-specifically attached to the slide, it would be impossible to tell by visual inspection if the DNA is truly hybridized or non-specifically attached. Further, up to five percent of the tethers were attached to the slide on both ends, indicating that non-specific attachment is possible. So, slides with and without silanized oligomer probe attachment were compared in the hybridization step using the same biotinylated DNA solution. The attachment efficiency was very similar for the silanized and non-silanized slide when viewed with fluorescent staining. This experiment was repeated with different concentrations of silanized probes. In every case, the results appeared similar. At probe concentrations described in the procedure, the slide prepared with probes had a slightly higher percent of DNA that was non-specifically attached near the perimeter of DNA treated area, but still less than 10% that was gathered around the edges. For slides that were treated with probes diluted 1:100, 1000, or 10000 the probe slide looked more and more like the control with increasing dilution. Thus, it is suspected that the DNA is mostly non-specifically attaching to the slide on one end and not truly hybridizing. The difference at higher probe application concentrations is attributed to either: 1) the silane is attaching to the slide and hindering the non-specific attachment of DNA to the slide but not hybridizing to the probe for some unknown reason, or 2) the buffer salt from the probe solution or some other wetting function of the probe treatment makes the non-specific attachment of the DNA less favorable. This apparent lack of true hybridization either needs to be solved (see suggestion for future work, below) or attributed as non-specific attachment in subsequent work. The latter

solution might be perfectly acceptable as the DNA is extended to close to its full apparent length, the attachment is able to withstand up to 10 pN which is less than required for significant Brownian attenuation, and more than 90% of the DNA is available for any protein interaction that would be studied.
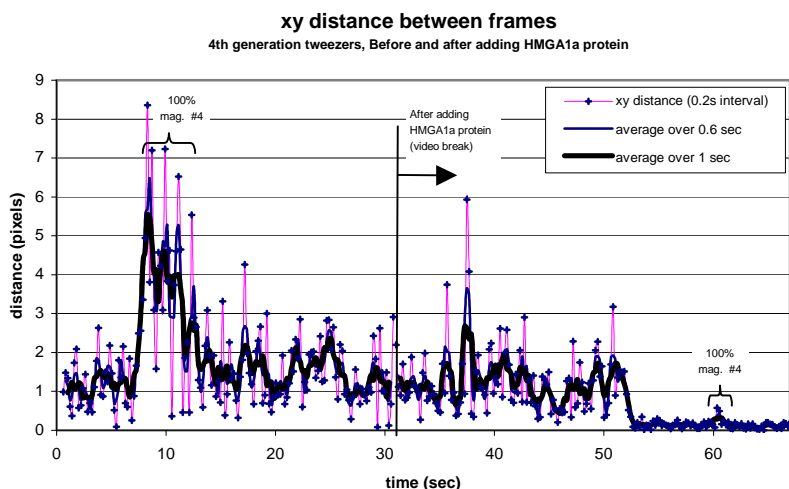

Figure 9. Plot of the x-y plane distance between successive points. Data is from the same trajectory shown in figure 8. The bold line is the data averaged over a one second interval. The bead travels a longer distance between points when the velocity is high (i.e. when the magnetic force is changing, between 8-12 seconds) and maintains an average range in the absence of the magnetic field. After the HMGA1a protein is added, the average distance is reduced somewhat and then abruptly and significantly declines to near zero around 52 seconds. Around 60 seconds, the tweezers are again applied but have little effect on the bead movement.

Ligase buffer and disulfide. The addition of T4 ligase was not optimized during this research period. T4 ligase and ligase buffer are added after biotinylation of the λ-DNA to covalently attach the biotinylated 12-base oligomer to one cohesive end of the DNA. This ligase and ligase buffer remain in solution during storage (-20C) and during hybridization where it is presumed the ligase is still active and can ligate the surface probe to the biotinylated target. Even if this ligation does not occur, the 12 complimentary base pairs of the probe and target should remain attached when pulled with less than 10pN.[25] The issue that has not been addressed is the ligase buffer contains 10 mM DTT, as well as 50mM Tris-HCl, 10mM $MgCl_2$, 1mM ATP, and 25μg/ml BSA. Thus, when 18uL of 10 mM DTT is added to 160uL of biotinylated DNA solution and subsequently diluted 1:100, it is present at 10 μM in solution. Since about 36 μL of biotinylated DNA is spotted on a slide, there are about 3.6×10^{-10} moles of DTT on the slide, which is on the order of the number of moles of disulfide linked silanized oligo probes on the slide. Thus there may a significant number of disulfide bonds between the surface and the probes that undergo an exchange reaction with the DTT. The ligase buffer is required as the T4 ligase can not function without the ATP. Some alternatives are the biotinylated DNA can be run through a sephadex column post-ligation, the ligation step can be eliminated, or a different attachment chemistry besides a disulfide linkage may need to be used.

Silane attachment. The silanized oligo must attach to the surface, yet there have been difficulties described with this chemistry. The silanes can polymerize in solution and

make surface attachment difficult.[26] Further, unreacted methoxy groups are susceptible to oxidation by the buffer solution. It has been discovered that vapor deposition is required to get good monolayer coverage of silanes on a silica surface.[27] Although perfect monolayer coverage is not required here, a finite number of silanized oligos need to be attached perpendicular to the surface so the DNA target has a reasonable probability to hybridize to the probe. At the same time, the probe density shouldn't be so dense as to decrease hybridization efficiency.[22] Further, several authors have stated the silane needs to be heat treated, ideally to 155C,[26] to cause cross-linking of the silane groups on the surface. Since heating the oligo to 155C is impractical in our case, the procedure is adapted from that of Kumar et. al.[28] where the dried oligo is heated to 50C for 5-10 minutes. This may be insufficient to prevent oxidation by the buffer and thus contribute to poor hybridization results.

   Video Recording issues. A Sony TRV-900 hand-held video camera was used to record video images of fluorescent DNA. The camera was configured to the front optical lens of the microscope. The "B" mode was selected where 20% of the image is directed to the eyepiece and 80% of the image is directed to the camera. The front optical image is magnified about twice that of the eyepiece, so the image is not as intense as seen through the eyepiece. However the camera has a zoom capability on it, so the image could be greatly magnified or reduced. There is an inverse relationship between the magnification and the intensity of the image; when the zoom was all the way in, the recorded image was very dark and it was required to increase the laser power. With the zoom at the other extreme, the image was much brighter and laser power could be reduced. Thus there is a trade-off between size of the image and rate of photobleaching and / or photo-damage.
\
Another important aspect of the camera is the adjustment of the frame rate of capture and the aperture. With the camera in automatic mode, the shutter speed is 60 frames per second (interlaced) and the aperture is fully open. The camera also adds 18dB of gain since the image is so dark. Under these settings, the recorded video appears to the human eye as fluent as the real-time image, but the picture is very grainy with a large loss of detail. In addition, any still photos taken from the digital image are of even lower quality than the moving video because it is only half of the interlaced image. It is possible to switch this particular camera to progressive scan mode, where the image is no longer interlaced. This results in a choppy video of 15 frames per second or less but an increase in intensity and picture quality. Also, the frame rate can be manually adjusted to 60, 30, 15, or 8 frames / second. With the slower frame rate, the image is much brighter but the video very choppy. The quality of the image from this commercially available camera was suitable for recording video during sample preparation optimization. A nitrogen-cooled CCD was not used during the 10-week internship, but will be required for use in collecting spectroscopic data. The frame rate required for spectroscopic data will be much slower than the video rate of 15 frames / sec. Thus, the DNA Brownian motion will need to be attenuated to remain mostly within a diffraction-limited area.

Suggestions for future work: As this is on-going research that has been tackled in segments by two researchers so far, a few suggestions for future work are included.

C6 instead of C3-SS linker. Both of the probe attachment papers cited in the procedure use C6 linkages between the probe and the disulfide.[28, 30] It has been shown[26] that increasing the linkage distance from the oligomer to the glass surface greatly increases probe attachment efficiency as the electrostatic repulsion between the negatively charged DNA and the surface retards attachment. This could also be achieved by extending the C3 linker of the silane (3-mercaptopropyl) but may be difficult because longer mercapto-functionalized silanes are not commercially available. Alternatively, a bisfunctional linker could be used (as demonstrated in other published methods[26, 30-32]) for probe attachment prior to hybridizing the 48kbp λ-DNA to the slide.

2.8 or 4.4 μm superparamagnetic beads. Increasing the amount of superparamagnetic material greatly increases the force of the magnetic field upon the DNA. Thus a sufficient force may be applied with less current. The disadvantages are that larger beads may interact more with the DNA strand or the surface and may distort or block the image during single molecule studies. However, the 2.8 μm beads will probably not interfere with the image when the DNA is fully stretched horizontally to the viewing angle. Even if the DNA is extended vertically, the larger beads may not affect the view because the DNA is observed from beneath the cover slip.

Software updates. The radial profile of 4.8μm diameter beads calibrated at various focal depths have been used to determine the vertical bead position from 2-dimensional CCD images with comparable accuracy to that in the x-y plane.[20] This method uses the wave properties of the diffraction rings and the linear relationship between the phase shift and the calibrated height to interpolate an accurate z-value. This would not be difficult code to write and could contribute much more detailed information from the bead trajectories. Another worthwhile investment of time improving the gaussian fitting program is to add a for-next loop for multiple image processing. A sixty-second video has about 900 frames and takes about eight hours to digitize with the current program. If the software was updated to automatically load each image in succession, the user could select the bead in each image without interruption and reduce this time to about 30 minutes. With a little more investment of programming time, the bead could be selected in the first image and the program would then automatically find the bead in each image and digitize the trajectory with only one click.

Alternative dyes. With the current laser excitation, ethidium bromide is a possible alternative as its absorbance maximum overlaps the excitation wavelength of the 532nm laser. It is possible that the loss of fluorescence at higher ionic strengths may not occur with ethidium bromide, and the rate of photobleaching may not be as fast. Also the dye is much cheaper than POPO-3.

5th generation magnetic tweezers; x-y translation. Since the proximity of the magnetic tweezer tips are on the order of 1mm apart and the tweezers currently move with the stage, an x-y translation of the tweezers would allow quick repositioning of the magnetic focal point when the slide is being translated.

Conclusions

The results from previous method development were repeated and then improved upon, while a method of staining and viewing the tethered DNA was developed. Some attachment procedure optimization issues were addressed. The 3rd and 4th generation of magnetic tweezers developed at the EMSL were characterized and evaluated and then used to attenuate the Brownian motion of tethered beads while viewing with wide-field fluorescence microscopy. A method of tracking bead trajectories over time was utilized and some methods of analyzing the trajectory data were presented. Finally, a protein was added to interact with the tethered DNA and changes in the bead trajectories were measured.

In order to collect spectroscopic data, the DNA must be held within the diffraction-limited focus of the laser, which is on the order of 500nm. In this report, it has been shown that the standard deviation in Brownian motion of one end of a tethered DNA molecule can be reduced to around 1µm with the magnetic tweezers. Of course, this is reduced further with stronger magnetic fields but then the DNA is stretched unnaturally and proteins may interact differently with the molecule in this case.[33] Thus, there is likely a trade-off between the ability to attenuate the Brownian motion sufficiently for SMS studies and the realism of the protein interaction. With slight tweaking of the current magnetic tweezer set-up, it should be short work to begin investigating these phenomena.

References

1) Han, J. J.; "Research Report for the 2004 Summer Research Institute for Interfacial and Condensed Phase Chemical Physics at Pacific Northwest National Laboratories," **2004**, 1-12.
2) Weiss, S., *Science*, **1999**, *283*, 1676-1683.
3) Smith, S.; Finzi, L.; Bustamante, C.; *Science,* **1992**, *258*, 1122-1126.
4) Strick, T.R.; Croquette, V.; Bensimon, D., *Proc. Natl, Acad. Sci USA*, **1998**, *95*, 10579-10583.
5) Bryant, Z.; Stone, M.; Gore, J.; Smith, S.; Cozzarelli, N.; Bustamante, C.; *Nature*, **2003**, *424*, 338-341.
6) Smith, S.; Cui, Y.; Bustamante, C.; *Science,* **1996**, *271*, 795-799.
7) Bennink, M.; Scharer, O.; Kanaar, R.; Sakata-Sogawa, K.; Schins, J.; Kanger, J.; de Grooth, B.; Greve, J., *Cytometry,* **1999**, *36*, 200-208.
8) Perkins, T.; Quake, S.; Smith, D.; Chu, S.; *Science*, **1994**, *264*, 822-825.
9) Lyon, W.; Fang, M.; Haskins, W.; Nie, S.; *Anal. Chem.*, **1998**, *70*, 1743-1748.
10) Florin, E.; Moy, V.; Gaub, H.; *Science*, **1994**, *264*, 415-417.
11) Strick, T.R.; Allemand, J.; Bensimon, D.; Croquette, V.; *Biphys. J.*, **1998**, *74*, 2016-2028.
12) Zlatanova, J.; Leuba, S.; *Biochem. Cell Biol.*, **2003**, *81*, 151-159.
13) Ali, B.; Amit, R.; Braslavsky, I.; Oppenheim, A.; Gileadi, O.; Stavans, J.; *PNAS*, **2001**, *98*, 10658-10663.
14) Assi, F.; Jenks, R.; Yang, J.; Love, C.; Prentiss, M.; *J. App. Phys.*, **2002**, *92*, 5584 – 5586.
15) Danilowicz, C.; Greenfield, D.; Prentiss, M.; *Anal. Chem.*, **2005**, *77*, 3023-3028.
16) Yan, J.; Skoko, D.; Marko, J.; *Phys. Rev. E*, **2004**, *70*, 011905.
17) Haber, C.; Wirtz, D.; *Rev. Sci. Instrum.*, **2000**, 71(12), 4561- 4570.
18) de Vries, A.; Krenn, B.; Driel, R.; Kanger, J.; *Biophys. J.*, **2005**, *88*, 2137-2144.
19) Amblard, F.; Yurke, B.; Pargellis, A.; Leibler, S.; *Rev. Sci. Instrum.*, **1996**, *67*, 818-827.
20) Gosse, C.; Croquette, V.; *Biophys. J.*, **2002**, *82*, 3314-3329.
21) Cluzel, P.; Lebrun, A.; Heller, C.; Lavery, R.; Viovy, J.; Chatenay, D.; Caron, F.; *Science*, **1996**, *271*, 792-794.
22) Peterson, A.; Heaton, R.; Georgiadis, R.; *Nuc. Acids Res.*, **2001**, *29*, 5163-5168.
23) Zhu, C.; Wu, Y.; Zheng, H.; Chen, J.; Li, D.; Li, S.; Xu, J.; *Anal. Sciences*, **2004**, *20*, 945-949.
24) Fedele, M.; Battista, S.; Manfioletti, G.; Croce, C.; Giancotti, V.; Fusco, A.; *Carcinogenesis*, **2001**, *22*, 1583.

25) Lee, G.; Chrisey, L.; Colton, R.; *Science*, **1994**, *266*, 771-773.
26) Hong, H.; Jiang, M.; Sligar, S.; Bohn, P.; *Langmuir*, **1994**, *10*, 153-158.
27) Haller, I.; *J. Am. Chem. Soc.*, **1978**, *100*, 8050-8055.
28) Kumar, A.; Larsson, O.; Parodi, D.; Liang, Z.; *Nuc. Acids Res.*, **2000**, *28*, e71.
29) Rogers, Y.; Jiang-Baucom, P.; Huang, Z.; Anderson, S.; Boyce-Jacino, M.; *Anal.Biochem.*, **1999**, *266*, 23-30.
30) Bhatia, S.; Shriver-Lake, L.; Prior, K.; Georger, J.; Calvert, J.; Bredehorst, R.; Ligler, F.; *Anal. Biochem.*, **1989**, *178*, 408-413.
31) Chrisey, L.; Lee, G.; O'Ferrall, E.; *Nuc. Acids Res.*, **1996**, *24*, 3031-3039.
32) Adessi, C.; Matton, G.; Ayala, G.; Mermod, J.; Mayer, P.; Kawashima, E.; *Nuc. Acids Res.*, **2000**, *28*, e87.
33) Harada, Y.; Funatsu,T.; Murakami, K.; Nonoyama, Y.; Ishihama, A.; Yanagida, T.; *Biophys. J.*, **1999**, *76*, 709-715.

Fabrication and characterization alternative-multilayer structures of gadolinia-doped ceria and zirconia thin film grown by sputter-deposition

Yiguang Wang and Linan An
Central Florida University   and
Orlando, FL

Chongmin Wang, S. Vaithiyalingam, D.E. McCready,
L.V. Saraf and T. Thevuthasan
Pacific Northwest National Laboratory
Richland, WA

Alternative multilayer structures of gadolinia-doped ceria and zirconia have been grown by sputter-deposition on (0001)-Al_2O_3 substrates. The films were characterized by x-ray diffraction (XRD), atomic force microscopy (AFM), x-ray photoelectron spectroscopy (XPS), and transmission electron microscopy (TEM). The ceria and zirconia showed fluorite structure with highly (111) textured. TEM indicated that the orientation direction was $(111)_{ZrO_2/CeO_2}//(0001)_{Al_2O_3}$ and $[11\overline{2}]_{ZrO_2/CeO_2}//[\overline{2}110]_{Al_2O_3.}$ XPS results showed that the CeO_2 was fully oxidized without showing Ce^{3+} peaks. The ion conductivity of this structure shows great improvement and reveals that it is a potential material structure for low temperature electrolyte application.

Key words: thin films, sputter deposition, ion conductivity

1. Introduction

One aim of the solid oxide fuel cells (SOFCs) is to reduce the operating temperature. If the operating temperature is blow $600^{\circ}C$, for examples, the economic benefits and lifetime of SOFCs will be greatly enhanced. It is essential to develop low temperature electrolyte materials to meet this requirement.

Stabilized zirconia is the most widely studied electrolyte materials due to its high ionic conductivity and a desirable chemical stability in both oxidizing and reducing atmospheres[1,2]. However, the operation temperature for stabilized zirconia is as high as

90

1000°C. Even reducing the thickness of this material, the operation temperature is unlikely lower than 700°C[3]. Another promising electrolyte material is ceria doped with rare earths. The ionic conductivity of this material is well established for gadolinia- and Samaria-doped ceria; these dopants have been shown to produce highest conductivities in ceria[4]. For low temperature operation (500-700°C), doped-ceria electrolytes remain the only candidate materials.

In a recent study, the nanoscale alternative CaF_2-BaF_2 multi-layer structure drastically enhances the fluorine ion conductance of the materials[5]. The authors attribute the enhancement of ion conductivity to the influence of space charge regions at the interface. Azad S. and co-authors found the similar phenomenon in the system of ZrO_2-CeO_2 system[6]. To fabricate alternative multilayer thin film structure is likely a novel way to increase the ion conductance of materials by using the interfacial effects. In this research, we try to use the sputter deposition to fabricate the alternative gadolinia doped ceria and zirconia highly textured multilayer. Compared with MBE, sputter deposition has fewer requirements for the vacuum system and is potential for mass production. The conductance of the film produced by this method is also discussed.

2. Experimental procedure

The films were grown on the (0001) Al_2O_3 substrate in the sputter chamber. Three targets are used in the same chamber: Zr, Ce, and Gd sources (99.98%, company). For the deposition, RF sputter device for Zr and DC sputter for Ce and Gd. A mixture gas of O_2/Ar was used as sputter gas. In all the deposition process, the gas flow for Ar is 10 sccm and for O_2 is 3 sccm. The coating pressure is kept at 8×10^{-3} torr. The coating rate is

determined by RBS and is controlled at the constant: for ZrO_2, about 0.24nm/min, for CeO_2, about 0.6nm/min.

To characterize the deposition films, several techniques were applied, such as, atomic force microscopy (AFM), X-ray diffraction (XRD), X-ray texture mapping, transmission electron microscopy (TEM), and X-ray photoelectron spectroscopy (XPS). The electrical conductivity was measure using a four-probe van der pauw technique.
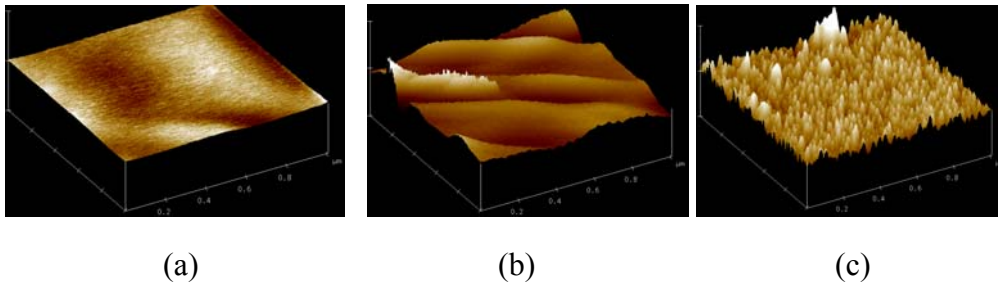
3. Results and discussion

3.1 AFM

| (a) | (b) | (c) |

Fig.1 AFM morphology for Ga_2O_3 doped ZrO2-CeO_2 multilayer thin films at different conditions. (a). 10-layer thin film deposited at 600^oC, (b) 32-layer thin film deposited at 600^oC, and (c) 10-layer thin films deposited at room temperature.

The temperature and the thickness of each layer effects on the roughness of thin films are studied by the AFM. The total thickness of all the thin films is controlled to ~240nm. Fig. 1 shows that the roughness of the thin films grown at room temperature and 600^oC. The results indicate that at room temperature, the roughness of the temperature is much higher than the ones at higher temperature. At the temperature of 600^oC, it was found that with the reduction of the thickness of each layer, the roughness will increase. But the morphology of the thin film with higher roughness at 600^oC is different to the one

at room temperature. Hence, the reason that results in the roughness is different. It is believed that at low temperature, the diffusion of atoms on the surface is so slow that they cannot rearrange themselves. The morphology shows island shape. At high temperature, though the diffusion is fast enough, the time for rearrangement of the atoms becomes critical. For thinner films, the deposition time is shorter. As can be seen in fig 1, the morphology of the film shows the ridge shape. If the deposition rate can be reduced or the deposition temperature can be increased, the roughness of the thinner films would improve.

3.2 XRD

Fig. 2 shows the XRD pattern of a film with five CeO_2 layers and five ZrO_2 layers alternative multi-layers. There are four strong narrow peaks belong to (0001) Al_2O_3 substrate. Both of CeO_2 and ZrO_2 exhibit highly (111) preferred orientation. Compared to the reference data of CeO_2 and ZrO_2[7, 8], all of the peaks shift to lower 2θ values due to the doping of gadolinia in the films. The lattice expansion for CeO_2 calculated from XRD pattern is about 0.92%. While for the ZrO_2, the expansion of the lattice is 1.97%, much larger than that of CeO_2. It may be because the radius of gadolinium is close to that of cerium and larger than that of zirconium. The difference of lattice expansion will reduce the mismatch, δ, which is defined as: $\delta=(a_{Ce}-a_{Zr})/a_{zr}$, where a_{Ce} and a_{Zr} are the lattice parameters of the CeO_2 and ZrO_2, respectively. Using the reference lattice values of 0.5411nm for CeO_2 and 0.5128nm for c-ZrO_2, a δ value of 5.5% can be obtained. The δ value determined from XRD pattern is about 4.4%.

For further determining the epitaxial growth, pole figures were done for ZrO_2 and CeO_2 respectively (Fig. 3). (220) is used as reflection face. The results indicate that CeO_2 and ZrO_2 have the single domain, indicating highly (111) preferred orientation.
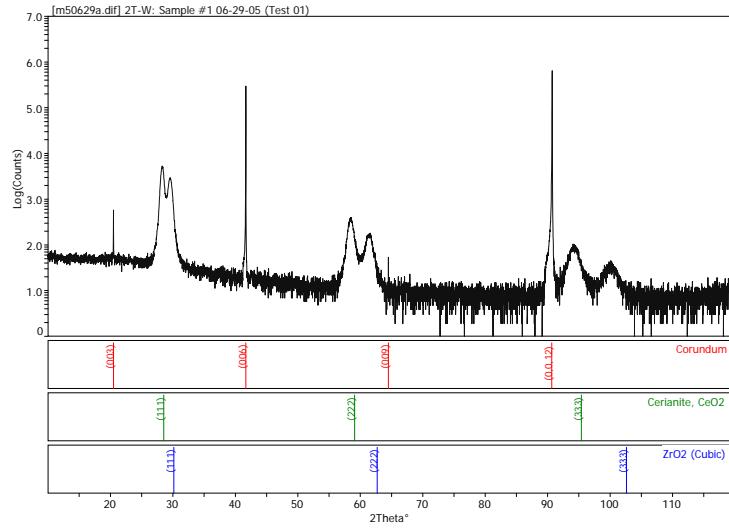

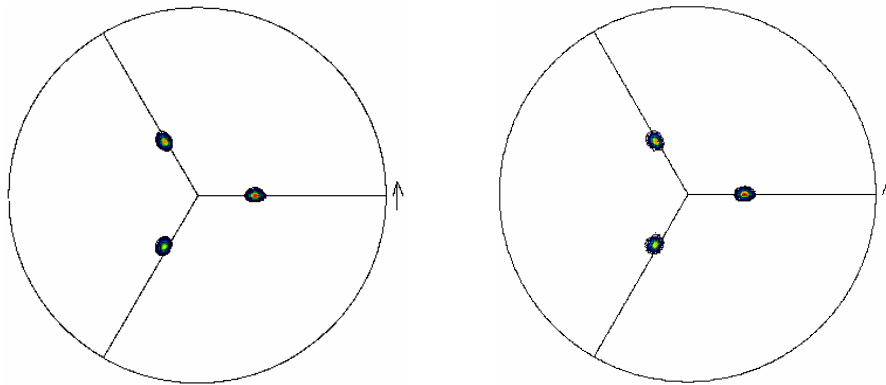Fig.2 XRD pattern of Ga_2O_3-doped ZrO_2-CeO_2 multilayer thin film

Fig.3 Pole figures of Ga_2O_3-doped ZrO_2-CeO_2 multilayer thin film

3.3 TEM

TEM pictures of 10-layer alternative Ga_2O_3-doped ZrO_2-CeO_2 multilayer thin film are shown in figure 4. The morphology of this thin film (Fig.4 (a)) reveals that Ga_2O_3-doped ZrO_2 and CeO_2 layers have the similar thickness. The thickness of each layer is close to 24nm. The selected area diffraction (SAD) indicates the orientation of the thin films is $(111)_{ZrO_2}//(111)_{CeO_2}//(0\bar{0}01)_{Al_2O_3}$ and $[11\bar{2}]_{ZrO_2}//[11\bar{2}]_{CeO_2}//[2110]_{Al_2O_3}$.

(a)   (b)
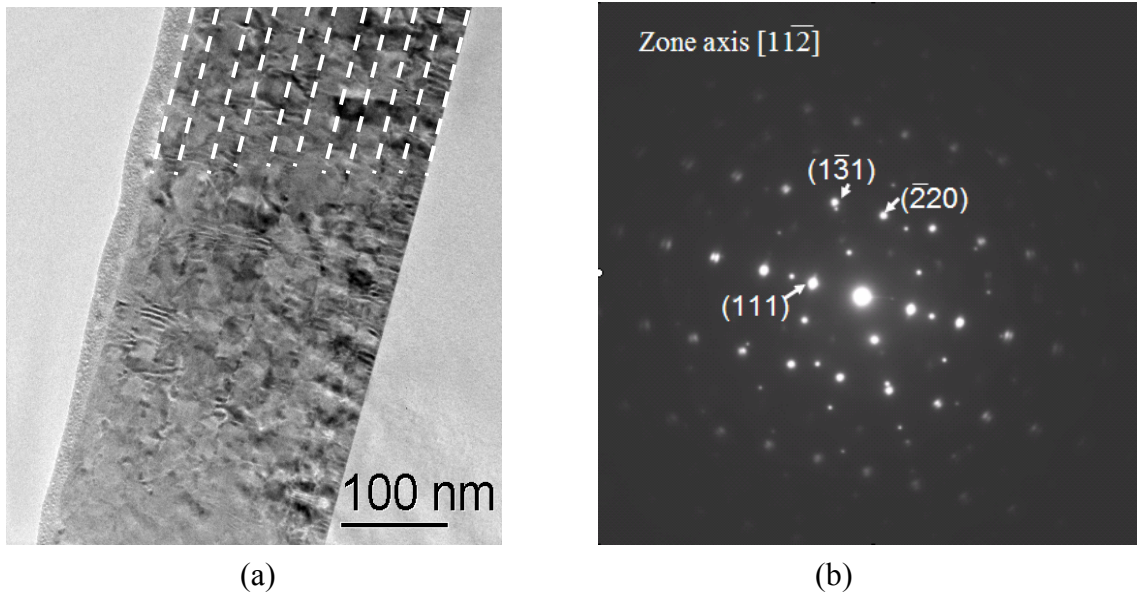
Fig. 4 The SEM of 10-layer alternative Ga_2O_3-doped ZrO_2-CeO_2 multilayer thin film. (a). cross section morphology of thin film, (b). Selected area diffraction (SAD)
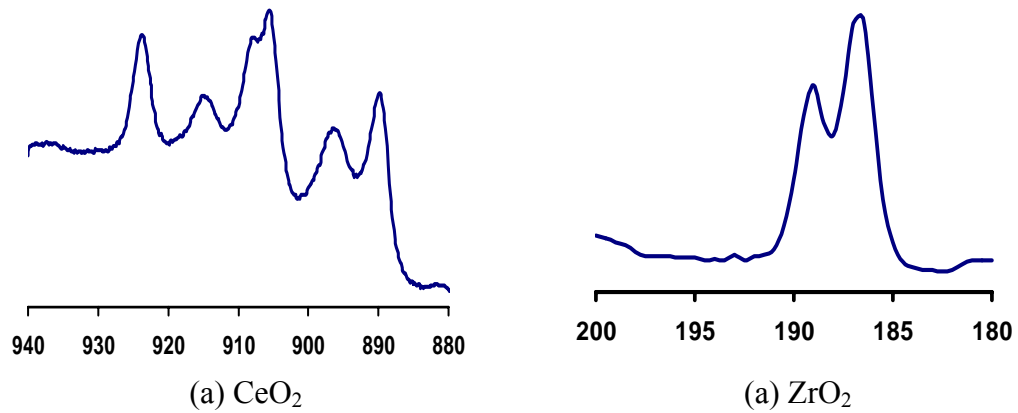
3.4 XPS

(a) CeO$_2$ (a) ZrO$_2$

Fig. 5 XPS of CeO$_2$ and ZrO$_2$ films

Fig. 5 shows the XPS of the surface of Ga$_2$O$_3$ doped CeO$_2$ film and the surface of Ga$_2$O$_3$ doped ZrO$_2$. From the spectroscopy of Ce, only Ce^{4+} peaks are observed, which indicates that the cerium is fully oxidized. Similar to the ZrO$_2$ spectroscopy, only fully oxidized ZrO$_2$ peaks can be seen.

It is well known that the ZrO$_2$ is a pure ion conductive electrolyte. However, the CeO$_2$ is considered as the mixture of ion conductivity and electron conductivity due to the transition of Ce^{4+} and Ce^{3+}. The XPS of gadolinia-doped CeO$_2$ films shows only Ce^{4+}. It can safely deduce that less electron conductive behavior in this film.
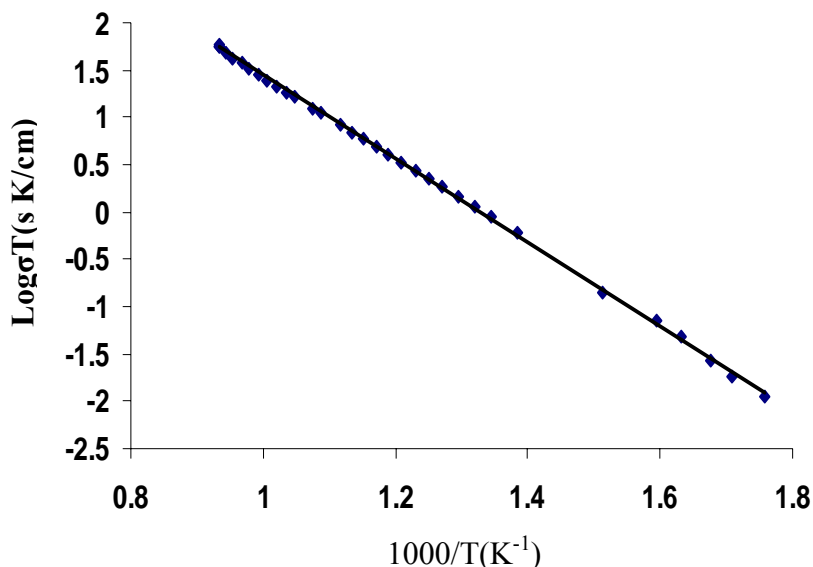

3.5 Ion conductivity

Fig. 6 Arrhenius plots of oxygen ionic conductivity of 50-layer Ga_2O_3-doped ZrO_2-CeO_2

multilayer thin film

The ionic conductivity of alternative gadolinia doped CeO_2-ZrO_2 film with 50-layer is shown in Fig.6. This material shows better electrical conductivity. As we stated above, the CeO_2 layer shows Ce^{4+} only without other valence. Furthermore, at low temperature, the electronic conductivity is significantly less compared to ionic conductivity [9]. Hence, we can consider that the conductivity measured is ionic conductivity. Compared with single crystalline ZrO_2 and polycrystalline gadolinia doped ceria[6], the alternative multilayer structure shows much better ion conductivity properties, especially at low temperature. It indicates that the materials can be used as potential ion conductor at low temperature for fuel cells, oxygen sensors.

It is believed that the high ion conductivity of the multilayer structure is due to the effect of interface between the films. Sata et. al.[5] found that an increase of the interface density in the multilayered CaF_2 and BaF_2 structure dramatically hence the fluoride ion

conductance of the materials. Igor et. al. [10] also attributed the increase of ionic conductivity of YSZ thin film to the interface contribution.

From the Arrhenius plots of the ion conductivity and the temperatures, the activation energy for ion conductivity can be calculated, 0.58ev. Compared with the data of single crystalline YSZ, 1.04ev, and the polycrystalline gadolinia doped ceria, 0.97ev, the activation energy for the multilayer structure is pretty low. As pointed out by Igor et al[10], with the increase of the contribution of interface for ion conductivity, the activation energy for conductance will decrease.

4   Conclusion

The alternative gadolinia doped CeO_2-ZrO_2 multilayer thin films are successfully prepared by sputter deposition. The films show highly (111) textured structure. The temperature is required not only for the smooth surface, but for the epitaxial growth. The characterization by XPS, TEM and XRD indicates the high quality of the films. The ion conductivity of the film is also discussed. The increase of the conductivity is believed to be the interfacial contribution.

Reference

[1] N.A. Minh, J. Am. Ceram. Soc. 76 (1993), 563.

[2] O. Yamamoto, Electrochim Acta, 45(2000), 2423.

[3] J. M. Ralph, A. C. Schoeler, and M. Krumpelt, J. Mater. Sci., 36(2001), 1161.

[4] B.C.H. Steele, Current Opinion in Solid state and Material Science, 1(1996), 684.

[5] N.Sata, K.Eberman, K Eberl, and J. Maler, Nature 408(2000), 946.

[6] S. Azad, O.A. Marina, C.M Wang, L. Saraf, V. Shuttanandan, D. E. McCready, A. EI-Azab, J. E. Jaffe, M. H. Engelhard, C.H. F. Peden, and S. Thevuthasan, Appl. Phys. Lett., 86(2005), 131906.

[7] Powder Diffraction File Database, International Center for Diffraction Dara, Newtown Square, PA, PDF 2002, 49-1642.

[8] Powder Diffraction File Database, International Center for Diffraction Dara, Newtown Square, PA, PDF 2002, 34-0394.

[9] N.Q Minh and T. Takahashi, Science and Technology of Ceramic Fuel cells (Elsevier, Amsterdam 1995), p.94

[10] I. Kosacki, C. M. Rouleau, P.F. Becher, J. Bentley, and D. H. Lowndes, Solid State Ionics, 176(2005), 1319

In situ study of Cu diffusion through barrier materials by Photoelectron Emission Microscopy (PEEM)

Wei Wei, Y.-M. Sun, and
J. M. White
University of Texas at Austin

and

Gang Xiong, Alan G. Joly, Kenneth M. Beck, and
Wayne P. Hess
Pacific Northwest National Laboratory
Richland, WA

As the trend of miniaturization continues in microelectronic fabrication, the current tantalum/tantalum nitride (Ta/TaN) diffusion barrier/liner for Cu interconnects will encounter scaling difficulties at the 45 nm node. To maintain a low effective interconnect resistivity (P_{eff} = 2.2 $\mu\Omega$ cm), an ultrathin diffusion barrier (~5 nm) is needed to scale the next-generation integrated circuit technology for the 45 nm node [1]. Recently, there has been an increasing interest to utilize transition metals, such as Ru and Ta, as Cu-plateable diffusion barrier [2-7]. Ru and Ta are air stable transition metals with high electrical conductivity (Ru bulk resistivity P = 7.1 $\mu\Omega$ cm versus P = 13 $\mu\Omega$ cm for Ta). More importantly, Ru and Ta show negligible solubility with Cu even at 900 °C [8]. Chyan [3] demonstrated that Ru is an excellent substrate for conformal Cu electroplating [4]. The inherently favorable interfacial bonding manifests in the strong adhesion between the electroplated Cu and Ru substrate even when annealed to over 600 °C [5]. Recently, Chan [4] has reported that ~20 nm Ru effectively prevents Cu diffusion up to 450 °C and Lane [9] demonstrated hat 5 nm Ru can function as a directly plateable Cu diffusion barrier up to at least 300 °C vacuum anneal.

A photoelectron emission microscope (PEEM) collects photoelectrons emitted from a specimen and projects them to an imaging screen. Generically speaking, PEEM is a new type of electron microscope, which uses photoelectrons to probe the sample surface. Many similarities can be found between PEEM and other electron microscopy techniques such as scanning electron (SEM), transmission electron (TEM), and field emission microscopy (FEM). Most commercial PEEMs are direct imaging microscopes as opposed to scanning instruments. Thus in-situ studies recorded at video rate are possible and that is a big advantage over the SEM and other scanning probe techniques.

Excitation can be accomplished by a variety of photon sources including UV lamps, lasers and synchrotron emission. The emission of low energy photoelectrons depends sensitively on the sample surface morphology and composition. Furthermore, surface contrast can be enhanced by energy selective excitation, photon polarization, or multi-photon excitation. Such versatility makes PEEM a powerful new tool for probing microscopic surface features and site selective dynamics [9,10]. An incoherent light source such as a mercury lamp (< 5 eV) is often used to obtain images quickly and easily. More sophisticated light sources have recently extended the utility of PEEM. For example, femtosecond laser pulses can be utilized in a pump-probe scheme to extract ultrafast surface dynamics while tunable synchrotron emission is used to map microscopic elemental composition.

In this project, for the first time, we applied photoemission electron microscopy (PEEM) to study the in situ surface change due to the copper diffusion through the Ru thin film. This study supplied a new potential method for both the academia and industry to in situ observe the copper diffusion process and deeply understand the functional mechanism of Ru as copper diffusion barrier material.

The substrate was Si(100) wafer coated with PVD Ta(250A). On the top of Ta layer there was 1000 A PVD Cu and 7000A electrical plated Cu. The substrate was provided by Sematech. Ruthenium films were deposited in a sputter deposition system (AJA 1500H) equipped with a main chamber, a load lock chamber, and three sputtering guns with one DC and two RF power supplies. The substrate could be heated to 773 K by a quartz lamp heater. All films were deposited at room temperature. The base pressure of the main chamber was $< 5 \times 10^{-8}$ Torr. Sputtering was done with flowing, 20 sccm, ultrahigh purity Ar (99.999%) that passed through a gas purifier prior to entering the chamber. The Ar pressures were 10 mTorr during the deposition. After deposition, films were transferred under the vacuum to an analysis chamber equipped with an X-ray photoelectron spectrometer. Film composition and thickness were determined by X-ray photoelectron spectroscopy (XPS). Using Mg Kα X-rays, spectra were taken at a pass energy of 58.7 eV. XPS binding energies (BE) were referenced to the Cu2p peak at

932.7 eV for pure Cu. Film thickness was calculated using the attenuation of the substrate Cu2p XPS peak intensity, using a mean free path of 0.68 nm in Ru.

The sample was then transferred into the UHV PEEM chamber and pumped for 1-2 hours until the base pressure drop down to $1 \sim 2 \times 10^{-9}$ torr. Sample was heated to desired temperature and kept at this temperature either through a hot filament (up to 400 °C) or by the electron bomb (400-1500°C). The temperature was read by the thermocouple welded on the sample holder. The corresponding PEEM images were captured in real-time and can be played as a movie (provided as supplement material).

The observed copper diffusion through the 1.1 nm Ruthenium thin film occurs at approximately 400 °C. The initial state of the sample at 47, as shown in Figure 1 (a), shows that the Ru film is uniform with one unknown defect bright spot. As the temperature increases, the intensity of the image drops down. This phenomenon might be due to the degassing of the adorbates on the Ru thin film surface, which, for example CO, can dramatically low down the metal surface work function. The intensity of image goes back as the temperature reaches to 318 °C since heating generally lowers the work function of metals (mainly due to volumetric expansion), as predicted by Wigner and Bardeen's double-layer theory[11, 12] and Lang-Kohn theory[13, 14]. The effective work function of polycrystalline Cu drops about 0.02 eV upon heating from 20 °C to 70 °C.[15-17] Similar results apply for Zn and Al. Such an effect can be easily verified by using PEEM to image a sheet of aluminum, for example. Once the temperature gets to 380 °C, we observe clearly the grain boundaries, associating with bunch of bright spot in the dimension of hundreds nan0meters. The PEEM image sequence shows a sudden change of features (the image quickly changes to very bright in short time) at around 400 °C, suggesting the changes result from the copper diffusion through the Ru thin film rather than from thermal expansion during heating.

In summary, we have successfully observed the in situ copper diffusion through Ru thin film along the temperature change by using the photoemission electron microscopy (PEEM). The work function change was used to indicate when the copper

reaches the top of the film. The in situ observation also supplies the information of the structure formed by the diffused copper. This is the first time use PEEM to study the copper diffusion barrier system.
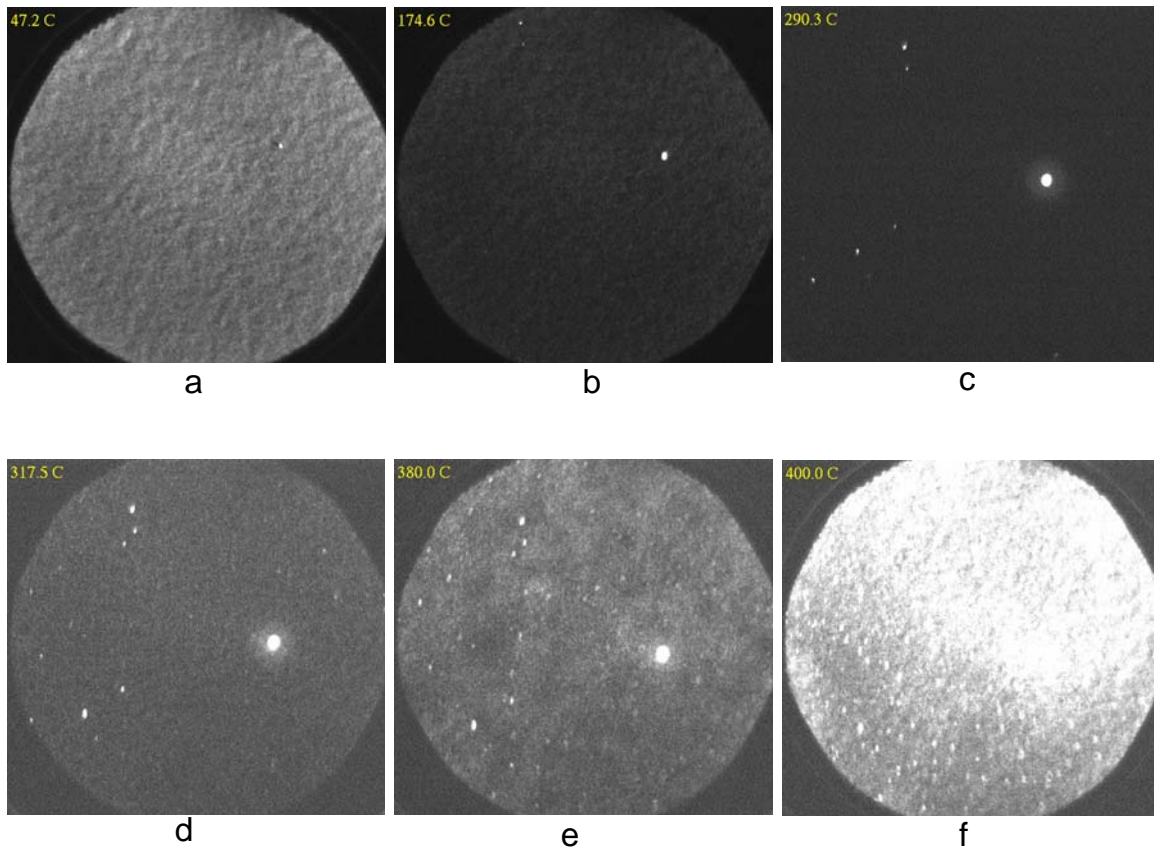
Figure 1: The corresponding PEEM images at the indicated temperature. a-e are the images before copper diffusion out Ru thin film and f is after the diffusion happened.

References

1. *International Technology Roadmap for Semiconductor-2002 Update*, (Semiconductor Industry Association, 2002), p. 74 http://public.itrs.net/.

2. M. W. Lane, C. E. Murray, F. R. McFeely, P. M. Vereechen, and R. Rosenberg, Appl. Phys. Lett. **83**, 2330 (2003).

3. Chyan, T. N. Arunagiri, and T. Ponnuswamy, J. Electrochem. Soc. **150**, C347 (2003).

4. R. Chan, T. N. Arunagiri, Y. Zhang, O. Chyan, R. M. Wallace, M. J. Kim, and T. Q. Hurd, Electrochem. Solid-State Lett. **7**, G154 (2004).

5. Y. Zhang, L. Long, T. N. Arunagiri, O. Ojeda, S. Flores, O. Chyan, and R. M. Wallace, *ibid.* **7**, C107 (2004).

6. D. Josell, D. Wheeler, C. Witt, and T. P. Moffat, Electrochem. Solid-State Lett. **6**, C143 (2003).

7. Q. Wang, J. G. Ekerdt, D. Gay, Y. M. Sun, and J. M. White, Appl. Phys. Lett. **84**, 1380 (2004).

8. T.B. Massalski, *Binary Phase Alloy Diagrams* (The Materials Information Society, 1990), p. 1467.

9. Kordesch, M.E., *Photonelectron emission microscopy and related techniques for in situ real-time surface studies*, in *In situ real-time characterization of thin films*, O. Auciello and A.R. Krauss, Editors. 2001, John Wiley & Sons, Inc. p. 217-259.

10. Kordesch, M.E., *Photoelectron emission microscopy of surfaces*, in *Encyclopedia of Surface and Colloid Science*. 2002, Marcel Dekker, Inc. p. 4059-4071.

11. Wigner, E. and J. Bardeen, *Theory of the work function of monovalent metals.* Phys. Rev., 1935. **48**: p. 84-87.

12. Bardeen, J., *Theory of the work function: II. The surface double layer.* Phys. Rev., 1936. **49**(9): p. 653-663.

13. Lang, N.D. and W. Kohn, *Theory of metal surfaces: Charge density and surface energy.* Phys. Rev. B, 1970. **1**(12): p. 4555-4568.

14. Lang, N.D. and W. Kohn, *Theory of metal surfaces: Work function.* Phys. Rev. B, 1971. **3**(4): p. 1215-1223.

15. Blevis, E.H. and C.R. Crowell, *Temperature dependence of the work function of single crystal faces of copper.* Phys. Rev. A, 1964. **2**: p. 580-584.

16. Kiejna, A., *On the temperature dependence of the work function.* Surface Science, 1986. **178**: p. 349-358.

17. Kiejna, A., K.F. Wojciechowski, and J. Zebrowski, *The temperature dependence of metal work functions.* J. Phys. F: Metal Phys., 1979. **9**(7): p. 1361-1366.

Structure of Pyrolytically formed Carbon
by Raman and EPR Spectroscopy

Weixing Xu and Linan An   Sarah D. Burton
University of Central Florida   and   Pacific Northwest National Laboratory
Orlando, FL   Richland, WA

1. Raman spectroscopy

The purpose of Raman spectroscopy measurement is to investigate the formation and nature of free carbon in structure rearrangement after pyrolysis. There is a definite difference in the electronic structures between diamond (sp^3 carbon) and graphite (sp^2 carbon), although both of them are allotropes of carbon element; that is, the former is a typical insulator with a large energy gap, while the latter is semimetallic as described by two-dimensional (2D) itinerant electron system. In the most cases of disordered carbons that are defined as sp^2/sp^3 mixed carbon, the increase in the sp^2 carbon ratio tends to establish the graphitic structure (clustering of sp^2 sites), which favors the itinerant electron character as confirmed by high conductivity and large diamagnetism.

In recent years, Raman spectroscopy has become one of most sensitive methods for the characterization of the different modifications of free carbon [i, ii,iii]. Raman spectra of the polysilazane reacting with different weight ratio of thermal initiator, and pyrolyzed at 1000 ºC was shown in Figure 1. For the sample with 4wt% thermal initiator, two bands,
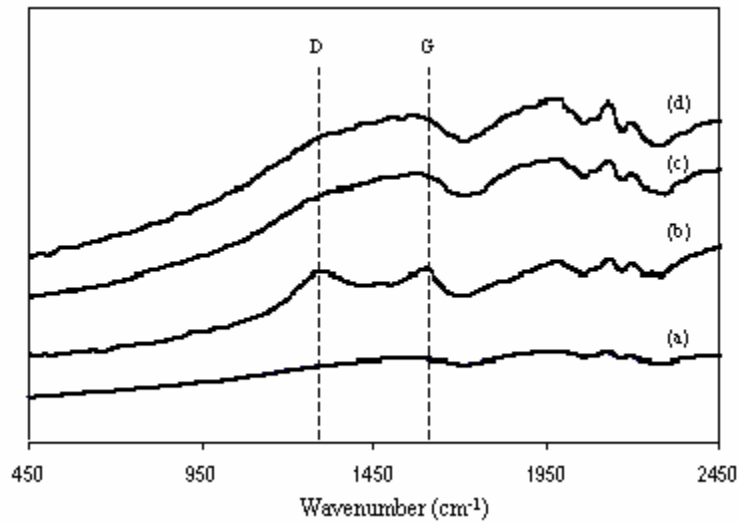
Figure 1 Raman spectra of the polysilazane reacting with different weight ratio of thermal initiator, and pyrolyzed at 1000 ºC. (a) without (b) 4 wt% (c) 6 wt% (d) 10 wt% of thermal initiator
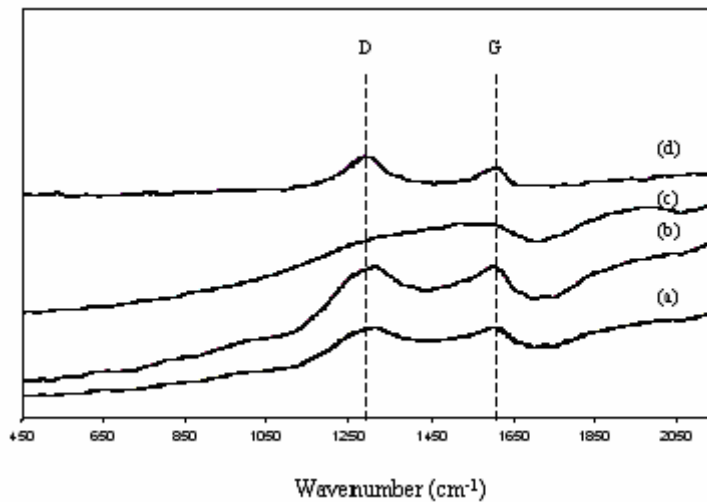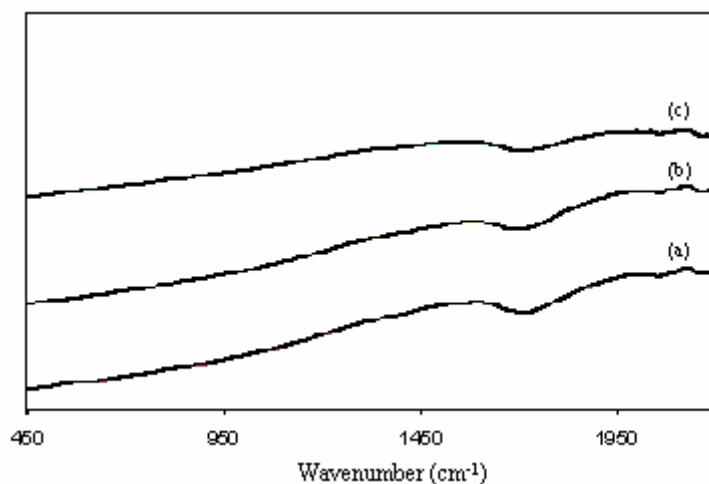

Figure 2 Raman spectra of the polysilazane reacting with different weight ratio of thermal initiator, and annealed at 1400 ºC. (a) without (b) 4 wt% (c) 6 wt% (d) 10 wt% of thermal initiator

at 1600 and 1280 cm^{-1}, can be observed in the spectrum, which are caused by amorphous Sp^2-hybridized carbon [iv]. These two bands were not observed in the spectrum of other samples, suggesting the absence of free carbon.

After annealing at 1400 ℃, Raman spectra were shown in Figure 30. Except the spectrum of the sample with 6wt% thermal initiator, free carbon can be observed in other samples. Those results suggest that the sample with 4 wt% and 6wt% of thermal initiator have different structures related to sp^2-hybridized carbon after pyrolysis and annealing respectively.

The Raman spectra of polyaluminasilazanes containing different amount of aluminum and thermal initiator and pyrolyzed at 1000 ℃ was showed in Figure 3. Similar results were observed for all the samples with Aluminum doping, no sp^2 carbon can be found in the samples pyrolyzed at 1000 ℃.

Figure 3Raman spectra of the polysilazane reacting with different weight ratio of Aluminum Isopropoxid and thermal initiator, and pyrolyzed at 1000 ℃. (a) 5 wt% Aluminum Isopropoxid without thermal initiator (b) 5 wt% Aluminum Isopropoxid and 4 wt% thermal initiator (c) 10 wt% Aluminum Isopropoxid and 4 wt% thermal initiator

After annealing at 1400 ºC, Raman spectra were shown in Figure 4. The bands of 1600 and 1280 cm^{-1} related to Sp^2-hybridized carbon can be observed in the spectrum of all the three samples. Those results suggest that after aluminum doping, similar resultant structures related to Sp^2-hybridized carbon are obtained.

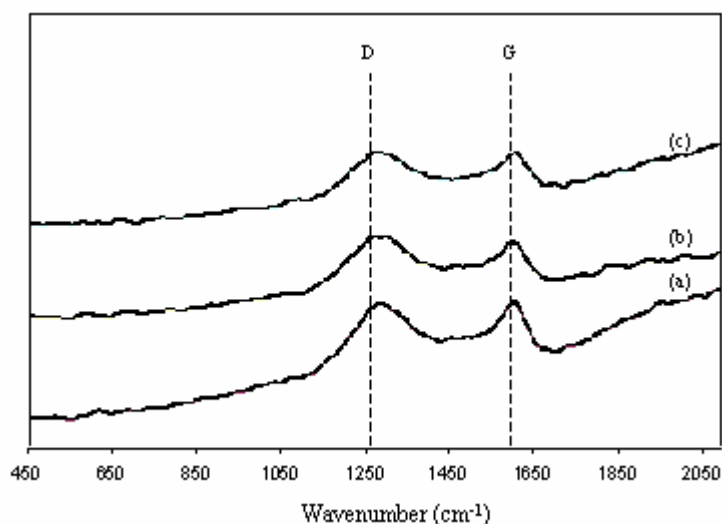*Figure 4 Raman spectra of the polysilazane reacting with different weight ratio of Aluminum Isopropoxid and thermal initiator, and annealed at 1400 ºC. (a) 5 wt% Aluminum Isopropoxid without thermal initiator (b) 5 wt% Aluminum Isopropoxid and 4 wt% thermal initiator (c) 10 wt% Aluminum Isopropoxid and 4 wt% thermal initiator*

2. Electron Paramagnetic Resonance

In 1921 Stern and Gerlach showed that an atom with a net electron magnetic can take up only discrete orientation in a magnetic filed [v]. In 1925, Uhlenbeck and Goudsmit proposed a new intrinsic property for the electron in addition to mass and charge [v]. In order to explain the behavior of alkali atom spectra in a magnetic field, they suggested that the electron must have a magnetic moment and they linked this with electron spin.

Electron papramagnetic resonance (EPR), also know as electron spin resonance (ESR) can be defined as resonant absorption of microwave energy in paramagnetic species by transition of the spin of an unpaired electron from one energy level to next in the present of a strong magnetic field. The first EPR experiment was conducted in 1944 when Zavoisky [vi] detected a peak in the paramagnetic absorption from $CuCl_2 \cdot 2H_2O$.

Electron paramagnetic resonance specifically occurs in paramagnetic molecules. i.e., molecules with unpaired electrons (e.g., free radicals, transition metals, and synthetic stable free radicals). Consider the electron as a small negatively charged object possessing a quantum mechanical property that is an analogous to spinning on its axis. This "spin" S is limited to 2S + 1 discrete states. For an unpaired electron, S = 1, so there are only two possible spin states, considered as spins in opposite directions. The value of S taken along a specified direction (Ms) is then $+\frac{1}{2}$ or $-\frac{1}{2}$. The spin states of an electron are usually labeled by their values of Ms. In the presence of an applied magnetic field, the quantum nature of the unpaired electron restricts it to two possible orientations (and hence two different energy states), parallel (Ms = $+\frac{1}{2}$) or anti-parallel (Ms = $-\frac{1}{2}$) to the field with an energy difference, ΔE, as described in Eq. (21). This is known as Zeeman splitting. Electromagnetic radiation, with a frequency corresponding to the difference in energy between these two energy states, can induce transitions of the electron between these energy states. EPR spectroscopy uses the existence of these two different energy states in a magnetic field to give an absorption spectrum based on these transitions.

The basic equation for an energy level transition (resonance absorption) for an unpaired electron is:

$$\Delta E = h \cdot \nu = g \cdot B \cdot H \qquad\qquad (1)$$

Were,

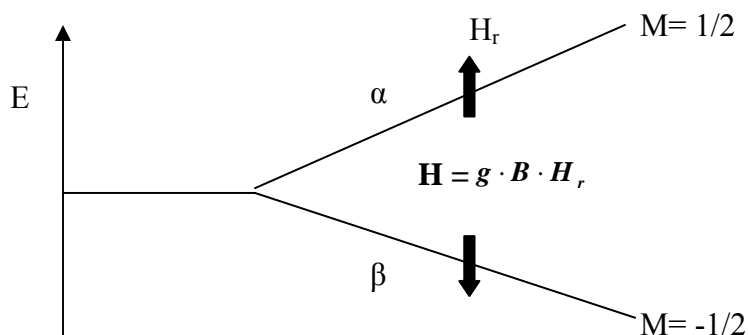ΔE = the energy difference between the two energy states

h = Plank's constant

ν = frequency of electromagnetic radiation

g = g factor

B = Bohr magneton. In EPR spectroscopy, the Bohr magneton is usually expressed as 9.274 x10^{-28} J/G. (10,000 G = 1 Tesla)

H = Resonance magnetic field

We can express this in terms of an energy level diagram as Figure 5:

Figure 5 An energy level diagram for EPR resonance absorption

For experimental convenience in ESR spectroscopy, microwave irradiation of a constant frequency is used and the magnetic field is varied. When a single unpaired electron in a magnetic field interacts with a nuclear spin, the spectrum splits into two or more lines, which produce hyperfine structure in the spectrum. The splitting of the spectrum is expressed in terms of a hyperfine coupling constant (units of G or MHz), and the absolute

position of the spectrum is expressed by the *g* value. Hyperfine couplings in EPR spectroscopy occur from the interaction between an electron spin and the magnetic dipole moment of a nearby nucleus. In polymer chemistry, usually the hyperfine structure of the ESR spectrum provides more important information about the radical than does the *g* value, because most radicals detected are carbon-centered radicals which have g~2.00.

Absorption of the applied electromagnetic radiation is detected by an EPR spectrometer, and after appropriate amplification, is displayed as the first or second derivative of the absorption field. Absorption resonance spectra are characterized by their line shape, linewidth and susceptibility (or integrated intensity).

The EPR line shape due to unresolved dipole or hyperfine broadening tends toward a Gaussian shape. The spin motion or exchange will alter the EPR line shape. For a 3D motion or exchange, the line shape becomes close to Lorentzian shape [vii, viii].

ESR in the metals gives the Lorentzian lineshape and its linewidth is proportional to the square of ESR g-shift [ix]. This behavior has been understood in terms of the relaxation mechanism via spin-orbit mixing of bands, which is known as the Elliott mechanism [x,xi]. The Elliott mechanism provides the ESR linewidth, or equivalently the spin-spin relaxation rate, as written by the relation:

$$\Lambda \boldsymbol{H} \propto \boldsymbol{T_2}^{-1} = \boldsymbol{\alpha}(\frac{\lambda}{\Delta \boldsymbol{E}})^2 \boldsymbol{\tau}^{-1} = \boldsymbol{\alpha}(\Delta \boldsymbol{g})^2 \boldsymbol{\tau}^{-1} \propto \boldsymbol{\rho} \qquad (2)$$

Here, ΔH is the ESR linewidth, T_2^{-1} the spin-spin relaxation rate, λ the spin-orbit coupling constant, ΔE the energy difference etween bands, the τ^{-1} relaxation rate of the electron

momentum, α the numerical constant of the order of unity, Δg the ESR g-shift and ρ the electrical resistivity.

A brief picture of this mechanism is that the spin-orbit mixing of two bands makes the matrix element between up and down spin states finite when the electron spin is scattered by phonon, impurity or disorder. Then, Eq.(22) suggests that the ESR linewidth is expected to show the corresponding behavior to the electrical resistivity ρ qualitatively, when the ESR linewidth is dominated by the Elliott mechanism[xi] .

2.1 Temperature dependence of line shape

Figure 6 compares EPR line shapes for the samples of polyureasilazane curing without, 4 wt%, 6wt% and 10wt% of thermal initiator and pyrolyzed at 1000 ºC, respectively. The evolution of the absorption signal curves is very similar for all the samples. EPR lines could be fitted well by a Lorentzian line for all the samples. It is suggested that rapid motion of the spin or interactions between electron spins. [xii]. The apparent shift in the position of the EPR lines is a result of a change in the operating frequency of the spectrometer caused by changes in the sample and resonator temperatures.

All the EPR spectra of SiCN exhibit no hyperfine structure, which means that the electron spin cannot be localized on nitrogen. Even if it were mainly localized on silicon, hyperfine satellites might be expected. The signal in SiCN is most likely due to carbon-centered free radicals, possibly with some delocalization of the electron spin [xiii, xiv].
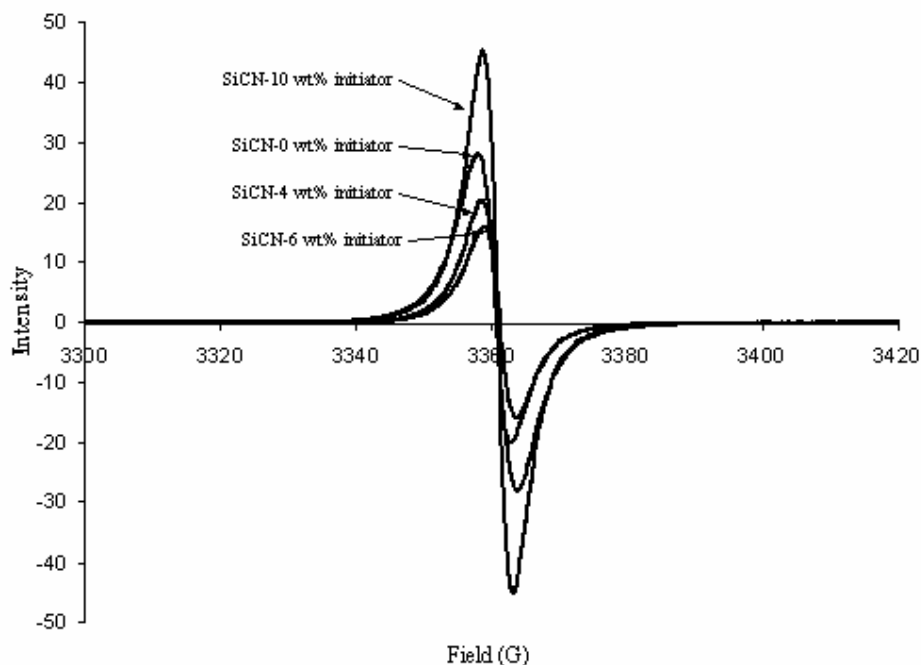
Figure 6 The EPR spectra for SiCN treated at 1000°C

2.2 Temperature dependence of linewidth

The width of the EPR signal reflects the interactions of the spins with their environment. In the case of mobile spins, the motion characteristics, such as spin mobility and dimensionality, are also parameters which play a major role in determining the EPR line linewidth. Thus, EPR has been used intensively as a technique for investigating the properties of mobile spins. The linewidth is expected to originate from the competition of broadening sources, hyperfine coupling, dipole spin-spin interactions and narrowing processes, which reflect the spin motion. According to the well-known process of motional narrowing, the observation of a narrow line could be the signature of a fast motion.
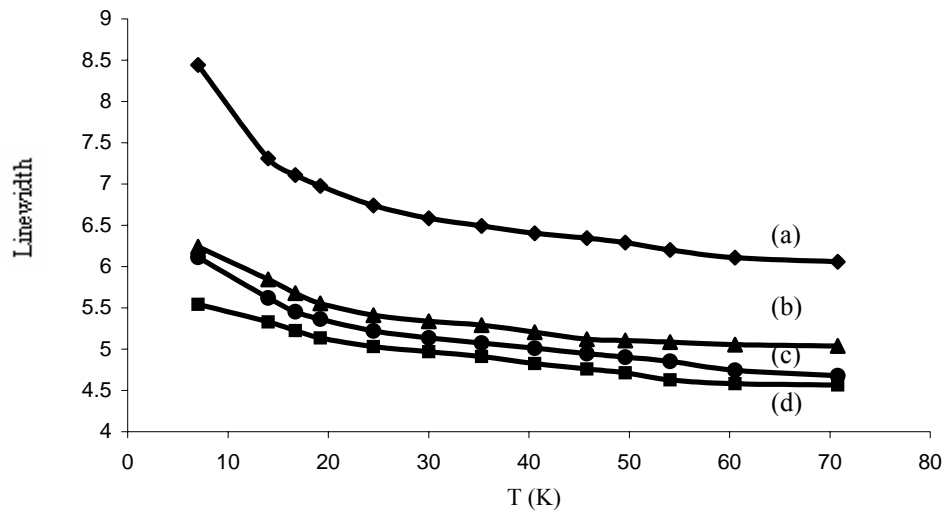
Figure 7 The temperature dependence of EPR linewidth (low temperature measurement)

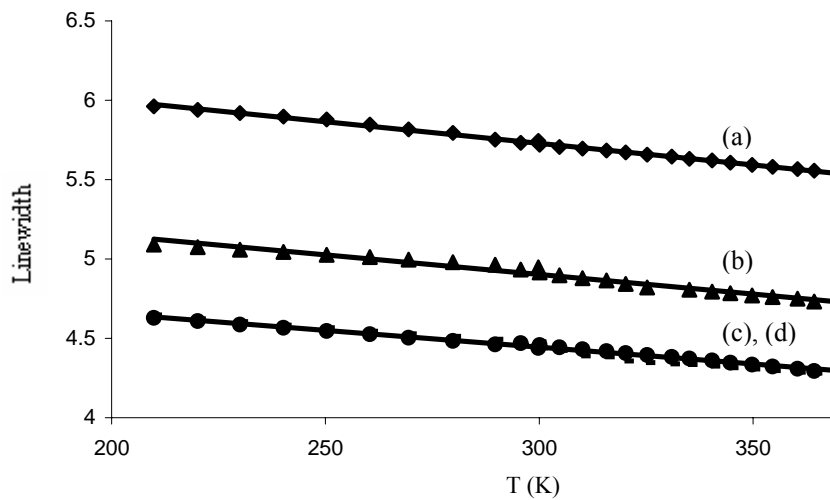*for SiCN (a) without (b) with 6wt% (c) 10wt% and (d) 4wt% of thermal initiator*

Figure 8 The temperature dependence of EPR linewidth (high temperature measurement)

for SiCN (a) without (b) with 6wt% (c) 4wt% and (d) 10wt% of thermal initiator

The temperature dependence of peak-to-peak linewidth measured in low temperature and high temperature of the samples of SiCN are shown in Figure 7 and Figure 8, respectively. A decrease in peak-to-peak linewidth of EPR spectra with increasing temperature was observed, which is contrary to the Elliott mechanism for conduction in

metal [xv] and metal-organic conductors [xvi, xvii, xviii]. The line broadening at low temperatures seems to be associated with a decrease in the hopping rate of the dangling bond electron at low temperatures [xix, xx, xxi, xxii].

In terms of motional narrowing due to hopping motion of dangling bond electron and/or motion of nuclei. The line broadening is assumed to be originally determined by hyperfine interaction of the dangling bond electron with surrounding nuclei. The line width is approximately given by

$$\Delta H_{pp} \cong g\mu_B (\Delta H_{hfs})^2 / h\nu_h \qquad (3)$$

Where, μ_B is the Bohr magneton, ΔH_{hfs} is the magnitude of the hyperfine splitting due to nuclei and h the Planck's constant, respectively [xxiii]. ν_h is approximately expressed as following [xxiv]:

$$\nu_h = \nu_{ph} \exp(-2\alpha\gamma - W/K_B T) \qquad (4)$$

ν_h is the photo frequency , α the decay rate of the wave function, γ the distance between two sites and W the energy difference between two sites. For a more exact expression, see Ref. [xxv]. In this case, activation energy (W) can be approximately obtained from a slope of log ΔHpp vs 1/T plot [xxvi].

In low temperature measurement, the peak-to-peak width vs reciprocal temperature was plotted in Figure 9. The data can be fitted with linear functions and activation energy can be calculated as 2.57 meV for SiCN sample without thermal initiator, 1.56 meV for SiCN sample with 4wt% of thermal initiator, 1.79 meV for SiCN sample with 6wt% of thermal initiator and 2.37 meV for SiCN sample with 10wt% of thermal initiator.
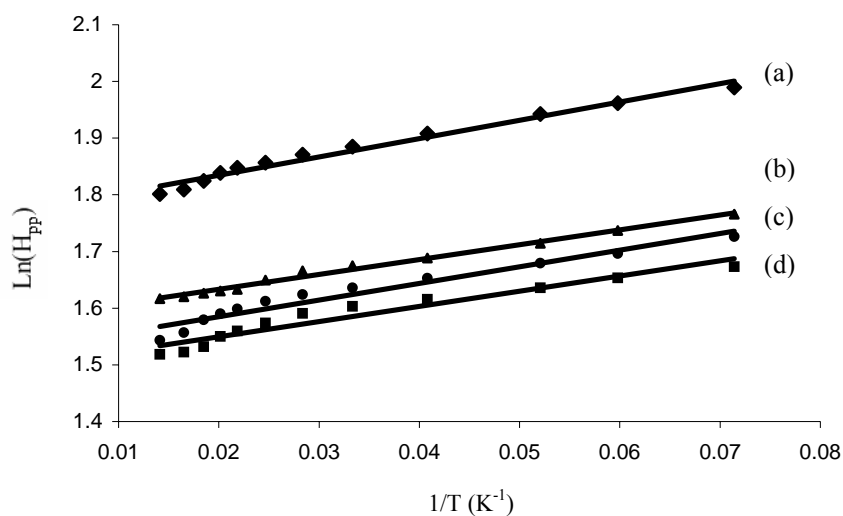
Figure 9 Plots of peak-to-peak width vs reciprocal temperature for SiCN (a) without, with (b) 6wt% (c) 10wt% and (d) 4wt% of thermal initiator (low temperature measurement). Lines represent the slopes corresponding to activation energies.
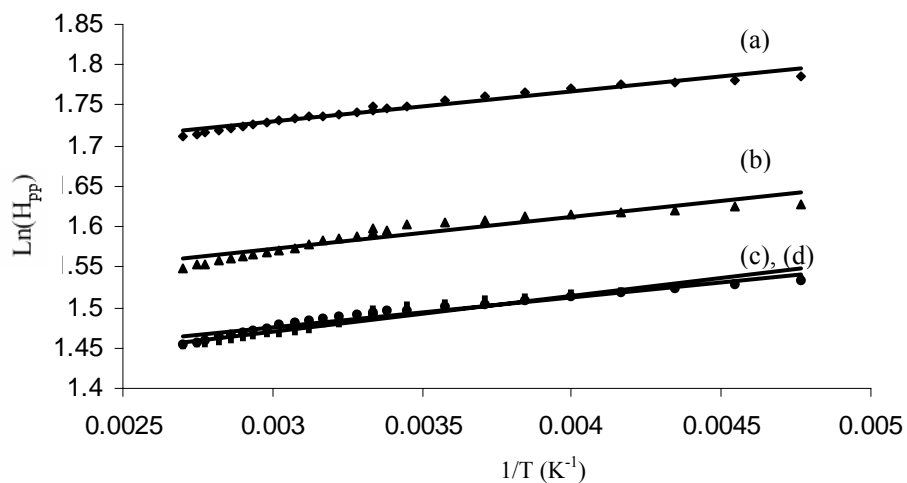

Figure 10 Plots of peak-to-peak width vs reciprocal temperature for SiCN (a) without, with (b) 6wt% (c) 4wt% and (d) 10wt% of thermal initiator (high temperature measurement). Lines represent the slopes corresponding to activation energies.

[i] Y. Wang, D.C.Alsmeyer, R. L. McCreery. Chem. Mater. 2. (1990), 557.

[ii] F. Tuinstra, J.L.Koenig, J. Chem. Phys. 53 (1970), 1126.

[iii] M. I. Nathan, J.E.Smith. Jr., K.N .Tu, J. Appl. Phys. 45. (1974), 2370.

[iv] Knight DS, White WB. J. Mater. Res. 1989; 4(2): 385.

[v] J.Wertz, J. Bolton, Electron Spin Resonance, Elemenatary Theory and Practical Application, 1986.

[vi] E. Zavoisky, J. Phys. USSR, 9 (211) (1945) 245.

[vii] A. Abragam, The Principles of Nuclear Magnetism, chapter 8 (Oxford University, Oxford, 1961).

[viii] Z.H.Wang, E.M.Scherr, A.G.MacDiarmid and A.J.Epstein, Physical Review B 45, 8, 1992, 4190.

[ix] F. Beuneu and P. Monod, Phys. Rev. B8, 2422, (1978).

[x] Rd. Elliott, Phys. Rev. 96,266, (1964).

[xi] Y. Yafet, Solid State Physics V14, Ed.H Ehrenreich, F. Seitz, D. Turnbull, Academic, N-Y., (1966).

[xii] N. Guskos, T. Bodziony, A.Biedunkiewicz, and K. AidiniS, Proceedings of the XXI International Meeting on Radio and Microwave Spectroscopy RAMIS 2005, Poznan-Bedlewo, Poland, April 24-28, 2005

[xiii] B. Frank, W. Markus, A. Fritz, and M. Klaus, Chem. Mater. 2004, 16, 919-929

[xiv] G. Jeschke, M. Kroschel, M. Jansen, J. Non-Cryst. Solids, 1999, 260, 216.

[xv] R. J. Elliott, Phys. Rev. **96**, 266 (1954).

[xvi] G. Iburillon, D. Gourier, P. Gamier and D. Vivien, J. Phm. Chem. 68,1050 (1984).

[xvii] M. Scharli, H. Kiesa, G. Ha&eke, W. Berlinger, K. W. Blazey, K. A. Mullar, Synth. Met. 99 317 (1988).

[xviii] N.S. SaricitIci, A. Grupp and M. Mehring, Chem. Phm. Lett. 192, 375 (1992).

[xix] H. Yokomichi, T. Hayashi, A. Masuda, Appl. Phys. Lett. 72 (1998) 2704.

[xx] H. Yokomichi, A. Masuda, J. Appl. Phys. 86 (1999) 2468.

[xxi] H. Yokomichi, T. Hayashi, T. Amano, A. Masuda,J. Non-Cryst. Solids 227±230 (1998) 641.

[xxii] C.B. Labelle, S.J. Limb, K.K. Gleason, J. Appl. Phys. 82 (1997) 1784.

[xxiii] P.W. Anderson, P.R. Weiss, Rev. Mod. Phys. 25 (1953) 269.

[xxiv] N.F. Mott, E.A. Davis, Electronic Processes in Non-Crystalline Materials, 2nd Ed., Clarendon, Oxford, 1979, p. 33.

[xxv] D.K. Wilson, Phys. Rev. A 134 (1964) 265.

[xxvi] H. Yokomichi, K. Morigaki, Journal of Non-Crystalline Solids 266-269 (2000) 797-802.

Atomically Resolved Adsorption of 2-butanol on TiO$_2$(110) Investigated by *in situ* Scanning Tunneling Microscopy

Zhenrong Zhang, A. Bondarchuk, J. Mike White

Chem. and Biochem. Department, University of Texas Austin, TX 78712

and

Z. Dohnálek, J. Kim, Bruce D. Kay

Pacific Northwest National Laboratory, Fundamental Sciences Directorate, Richland, WA 99352

In recent years TiO$_2$ has attracted significant attention because of its potential for the catalytic oxidation of organic contaminants [1,2]. As such, the thermal and photocatalytic oxidation of simple alcohols (e.g. methanol, ethanol, 2-propanol) has been extensively studied on model TiO$_2$(110) surfaces [3-5]. Despite that, atomic level understanding of these systems is still missing. In this study, we examined 2-butanol adsorption on TiO$_2$(110) (1×1) surface using *in situ* variable temperature scanning tunneling microscopy (VT-STM).

Experiments

Experiments were performed in an ultrahigh vacuum variable-temperature STM (Omicron) chamber. The base pressure is 7×10^{-11} Torr. This chamber is additionally equipped with a reverse view LEED (Princeton Research), a single pass cylinder mirror analyzer (Physical Electronics) for Auger studies, a mass spectrometer (UTI, 100C), and a sputter gun.

The TiO$_2$ (110) (PI KEM, UK) was cleaned by cycles of Ar ion sputtering (1keV, 1μA) and annealing at 1000-1100 K in UHV until no signal from contaminants was observed in Auger spectrum and sharp (1 × 1) LEED patterns were obtained. Then the sample cleanness was checked by STM. 2-Butanol (Aldrich, 99.5+ %) was purified by several freeze-pump-thaw cycles using liquid nitrogen. Gas was dosed through a 0.25 inch outer diameter doser tube with a 7 μm pinhole aperture. The doser tube could be positioned within 2 mm to the sample surface while the tip is kept within the tunneling distance. This setup makes the *in situ* gas adsorption investigations possible.

Results

Fig. 1 shows the atomically resolved STM constant current image and the ball model of the clean TiO$_2$(110) surface. The atoms on the bright lines parallel to the [001] direction are clearly observed with a 0.30 nm interval. It has been shown that the corrugation on STM image of TiO$_2$(110) is reversed from physical one because of electronic effects [2]. Thus these atoms are identified as the fivefold coordinated Ti atoms. In this study, the most important feature is the bright spots between the Ti rows. They are assigned to oxygen vacancies which are believed to act as the primary reactive centers for the adsorption of alcohols. Statistically the number density of oxygen vacancies is ~10% with respect to the number of Ti atom.

Fig. 2 displays four STM images taken from the same area on initially clean TiO$_2$(110) and dosing with 2-butanol. The bright upper terrace was used as a marker for the imaged area. In the clean surface image (Fig.2 (a)), one example of oxygen vacancies is highlighted with a square.
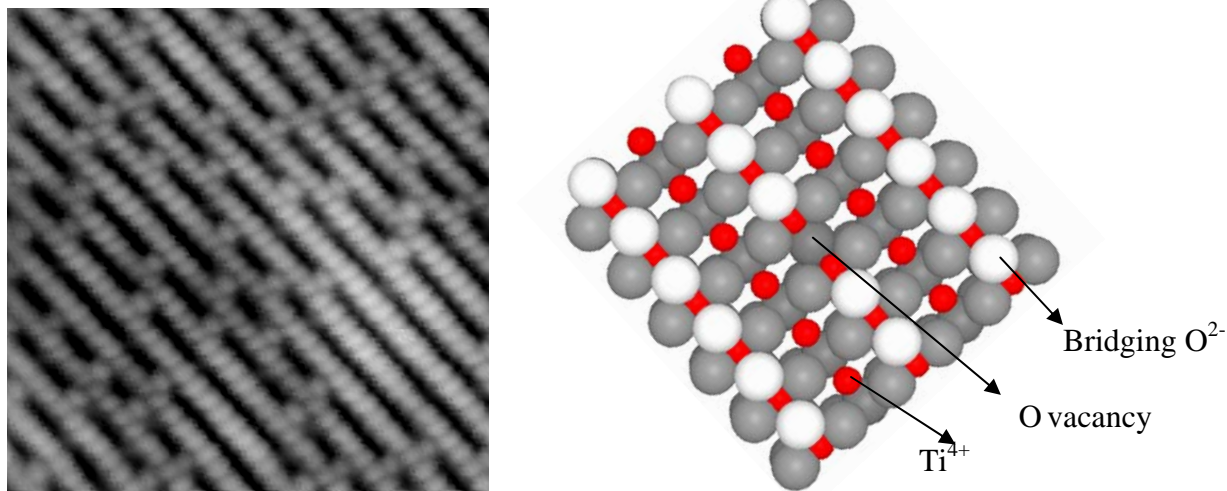
Fig.1 (a)Atomically resolved STM constant current image of the clean TiO$_2$(110) surface.
(b) the ball model of TiO$_2$(110) surface.

After the first 2-butanol dose as shown in Fig.2 (b), there are two kinds of new features. One type is the bright features as labeled with white ellipses. They are elongated in a direction perpendicular to the Ti^{4+} rows. The other type is the grey features as marked by the black circle. The size of the gray features is smaller than that of the bright ones. Compare with the clean surface, all these new features sit on the oxygen rows. For the bright features, they are exactly centered on oxygen vacancies while the grey ones do not relate to the oxygen vacancies. The vacancies which correspond to the bright features (1, 2, 3 on Fig.2(b)) are marked by the solid ellipses in Fig.2 (a). At higher coverages, as more 2-butanol was dosed onto the surface, the number of bright features increased and the newly observed features (marked with dashed ellipses in fig 2 (c)) also appear on the oxygen vacancies. When the dosage increased to 0.07 ML (Fig. 2(d)), another type of bright features appeared after most of the oxygen vacancies are titrated away by first kind of bright features. These new features are marked with black ellipses. They have the same brightness, shape and size as the previous bright feature, but they are elongated along the Ti^{4+} row instead of perpendicular to the Ti^{4+} row. In addition, they bond on the Ti^{4+} row. A grid is superimposed to identify the 2-butanol adsorption sites.

Based on the TPD results of alcohol adsorption on TiO$_2$(110) and considering the size of the bright features and grey features, the bright features are assigned to butoxy molecules and the grey features to hydroxyl groups. When 2-butanol adsorbs on the TiO$_2$ surface, oxygen vacancies are the preferential adsorption sites at low coverage as shown in Fig. 2(b) and 2 (c). Since the 2-butanol dissociates upon adsorption, the protons are transferred to the bridging oxygen atoms and form hydroxyl groups. The elongation of the butoxy/2-butanol features suggests that the hydrocarbon chains of the 2-butanol are oriented perpendicular to the Ti^{4+} rows when they adsorb at oxygen vacancies. This is easy to understand because that the bridging oxygen rows protrude higher than Ti^{4+} rows. The orientation of hydrocarbon chain is therefore unfavorable due to steric repulsion between the hydrocarbon chain and the bridging oxygen atoms.

After all the oxygen vacancies are occupied as the coverage increases, the next favorable adsorption sites are Ti^{4+} cations (black ellipses in Fig. 2(d)). This is consistent with the methanol

adsorption process on TiO$_2$(110) investigated previously by M.A. Hendersen using ensemble-
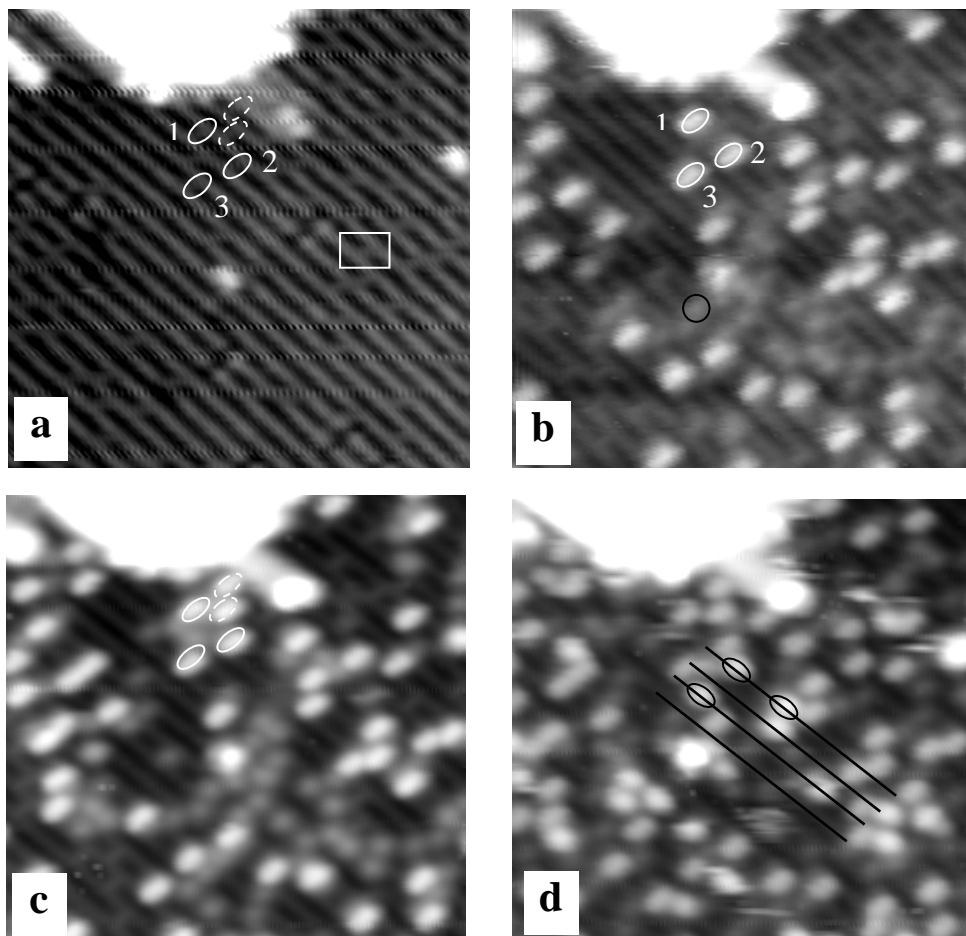

Fig.2   The STM images of same area before and after adsorption of 2-butanol on TiO$_2$(110) at 100 K: (a) bare surface. (b) surface after expose to 0.04 ML of 2-butanol, (c) after 0.05 ML of 2-butanol, (d) after 0.07 ML of 2-butanol.

averaged techniques [3]. When the 2-butanol molecules adsorb on the Ti^{4+} rows, the hydrocarbon chains are oriented along the rows. This maximizes the attractive interactions between the hydrocarbon chain and the substrate.

Conclusions

STM images of the same area on the surface before and after 2-butanol adsorption reveal that 2-butanol adsorbs preferentially on oxygen vacancy sites at 100 K. The observed features are elongated in a direction perpendicular to the Ti^{4+} rows suggesting that the hydrocarbon chains are oriented perpendicular to the Ti^{4+} rows. The hydroxyl groups are also observed in the STM images suggesting that the OH group in 2-butanol cleaved. At higher coverages, when the oxygen vacancies are filled, the additional 2-butanol binds to the Ti^{4+} sites with the hydrocarbon chain oriented along the rows. These experiments directly demonstrate that oxygen vacancies play a major role in the adsorption of alcohols on TiO$_2$ surface.

References:
1. A. Mills, R.H. Davies, D. Worsley, *Chem. Soc. Rev.* 22(1993) 417.
2. U. Diebold, *Surf. Sci.* 48 (2003) 53.
3. M.A. Henderson, S. Otero-Tapia and M. E. Castro*, Faraday Discuss.,* 114 (1999) 313.
4. L. Gamble, L.S. Jung, C. Campbell, *Surf. Sci.* 348 (1996) 1.
5. D. Brinkley and T. Engel, *J. Phys. Chem. B* 104 (2000) 9836.

Stephan E. Barlow
Director
ICPCPSRI
(509) 376-9051
se.barlow@pnl.gov